

Studying the Photodissociation of
Chlorine-Containing Molecules
with Velocity Map Imaging

Dissertation zur Erlangung des
naturwissenschaftlichen Doktorgrades der
Julius-Maximilians-Universität Würzburg

vorgelegt von

Christian Tobias Matthaer
aus Koblenz

March 27, 2023

Eingereicht bei der Fakultät für Chemie und Pharmazie am ____.____.2022

Gutachter der schriftlichen Arbeit

1. Gutachter: Prof. Dr. Ingo Fischer
2. Gutachter: Prof. Dr. Roland Mitric

Prüfer des öffentlichen Promotionskolloquiums

1. Prüfer: Prof. Dr. Ingo Fischer
2. Prüfer: Prof. Dr. Roland Mitric
3. Prüfer: Prof. Dr. _____

Datum des öffentlichen Promotionskolloquiums: ____.____.2023

Doktorurkunde ausgehändigt am _____

"I choose a lazy person to do a hard job. Because a lazy person will find an easy way to do it."

Bill Gates

List of Abbreviations

BBO	β -barium borate
(p)BASEX	(polar) basis set expansion
BDE	bond-dissociation energy
CCD	charge-coupled device
Cl	chlorine in the ground state
Cl*	spin-orbit excited chlorine
(H)CFC	(hydro-) chlorofluorocarbon
(TD-)DFT	(time-dependent) density functional theory
DPI	dissociative photoionization
IC	internal conversion
IE	ionization energy
IVR	intramolecular vibrational energy redistribution
KDP	potassium dihydrogenphosphate
MCP	microchannel plate
MPI	multiphoton ionisation
Nd:YAG	neodymium-doped yttrium aluminum garnet
NMPI	nonresonant multiphoton ionisation
REMPI	resonance-enhanced multiphoton ionization
SPI	single-photon ionisation
SHG	second harmonic generation
THG	third harmonic generation
TKER	total kinetic energy release
TOF (MS)	time-of-flight (mass spectrometry)
(V)UV	(vacuum) ultraviolet
VMI	velocity map imaging
VR	vibrational relaxation

Abstract

Kohlenwasserstoffe, die Chlor beinhalten, stellen ein erhebliches Risiko für die Umwelt da. Falls sie die Stratosphäre erreichen, können sie dort von UV-Strahlung dissoziiert werden, wodurch unter anderem atomares Chlor freigesetzt wird. Das Chloratom trägt dann zur katalytischen Zerstörung der Ozonschicht bei. Um die Chemie der Atmosphäre besser verstehen zu können, ist es somit wichtig, die Photodissoziationsdynamiken, die zu der Freisetzung von Chlor führen, zu untersuchen und zu verstehen. Deshalb wurde diese Art von Molekülen schon vielfach untersucht. Allerdings können auch Radikale, die durch die Photodissoziation entstehen, weitere Chloratome beinhalten. Um die Atmosphärenchemie besser verstehen zu können, ist es somit wichtig zu untersuchen, ob diese Radikale weiteres Chlor freisetzen können, und wenn ja, wie dieser Prozess abläuft. Schwierigkeiten bei der Produktion der Radikale bei Photodissoziationsuntersuchungen hat dazu geführt, dass dieses Themenfeld bisher vernachlässigt wurde. Nur wenige halogenhaltige Radikale wurden bisher in geringem Umfang untersucht.

Das Ziel dieser Arbeit war es, Fortschritte in der Erforschung von Radikalen, die in atmosphärischen Vorgängen eine wesentliche Rolle spielen, zu erreichen. Chlorhaltige Radikale wurden mit dem Verfahren der Flash-Pyrolyse hergestellt. Die Dissoziationsdynamiken dieser Radikale wurde dann mit der Velocity-Map Imaging Methode untersucht. Mit dieser Methode ergibt sich ein Einblick in die kinetische Energie von Fragmenten, die in einem Photolyseprozess entstehen. Außerdem kann man aus den Velocity-Map Images die Winkelverteilung ableiten. Diese Informationen erlauben Rückschlüsse auf die im Dissoziationsvorgang beteiligten Zustände.

Chlorhaltige Radikale, die für Prozesse in der Atmosphäre relevant sind, besitzen normalerweise breite Absorptionsbanden im Bereich um 235 nm. Dieser Bereich wird häufig verwendet, um diese Radikale anzuregen und deren Dissoziationsdynamiken zu beobachten. Dies ist aber auch derselbe Wellenlängenbereich, der typischerweise für die Ionisation von Chloratomen in einem $[2 + 1]$ Resonanzverstärkten Mehrphotonenionisationsprozess (REMPI) verwendet wird. Da für diese Ionisationsmethode fokussiertes Laserlicht verwendet werden muss, ist die Intensität von 235 nm Licht in der Ionisationsregion sehr hoch. Die hohe Intensität hat den Nebeneffekt, dass manche Radikale mehrere Photonen absorbieren. Diese Radikale können dann dissoziieren, wobei sie Chloratome freilassen, die deutlich höhere kinetische Energien besitzen als welche, die durch ein einzelnes Photon dissoziiert werden würden. Diese hohen Energiekomponenten führen dazu, dass die Velocity-Map Images schwer zu interpretieren sind.

In dieser Arbeit wurde ein alternativer Ionisationspfad untersucht. Chlor kann auch mit 356 nm Licht in einem $[3 + 1]$ REMPI Prozess ionisiert werden.

Allerdings ist hierfür eine hohe Intensität durch enge Fokussierung des Laserstrahls erforderlich. Selbst damit kann nur eine geringe Menge an Chlor ionisiert. Günstig ist, dass die Wellenlänge 118.9 nm (Frequenzverdreifung von dem 356 nm Licht) im Verdreifungsbereich von Xenon liegt. Durch Experimente mit einer mit Xenon gefüllten Gaszelle, die zur Frequenzverdreifung eines Nd:YAG Lasers verwendet wurde, wurden bereits Erfahrungen in der Frequenzverdreifung gesammelt. Licht eines Farbstofflaser wurde in der Gaszelle frequenzverdreifung, wodurch Licht der Wellenlänge 118.9 nm entstand, mit dem anschließend Chlor angeregt wurde. Tatsächlich ließ sich hiermit atomares Chlor sehr effizient Ionisieren. Um einen Dissoziationsprozess komplett verstehen zu können, ist Wissen über den Spin-Bahn-angeregten Zustand von Cl notwendig. Jedoch liegt keine Cl* in dem verwendeten Verdreifungsfenster von Xenon. Trotzdem erlaubt diese Methode hochqualitative Bilder ohne störendes Hintergrundsignal von Chlor im Grundzustand aufzunehmen.

Um die hier vorgestellte neue Ionisationsmethode zu etablieren, wurde eine Studie an dem stabilen Molekül Benzoylchlorid durchgeführt. Benzoylchlorid wurde mit vier verschiedenen Wellenlängen angeregt (237 nm, 253 nm, 265 nm und 279.6 nm), wodurch es in den S₁, S₂ und S₃ Zustand angeregt wurde. Es wurde eine unimodale Energieverteilung beobachtet, die unabhängig von der Dissoziationswellenlänge war. Hierbei floss ca. 20% der Überschussenergie des Dissoziationsprozesses in die Translation der Fragmente. Außerdem war das Bild isotrop. Die Ergebnisse ließen den Schluss zu, dass ein statistischer Prozess für die Dissoziation verantwortlich ist, bei dem das Molekül aus dem schwingungsangeregten Grundzustand dissoziiert.

Nachdem die Zuverlässigkeit dieser neuen [1 + 1'] REMPI Ionisationsmethode für VMI von Chlor nachgewiesen war, wurde mit der Studie von chlorhaltigen Radikalen begonnen. Zuerst wurde das CCl₃ Radikal untersucht. Es wurde bereits gezeigt, dass CCl₄, ein Halogenalkan, einen starken Einfluss auf die Zerstörung stratosphärischen Ozons ausübt. CCl₄ wurde in der Vergangenheit vielfältig verwendet, wodurch viel in die Umwelt freigesetzt wurde. Sobald CCl₄ Moleküle in die Stratosphäre aufgestiegen sind, können sie dort UV Strahlung absorbieren, woraufhin sie zu CCl₃ und Cl zerfallen. In dieser Arbeit wurde CCl₃ durch die Pyrolyse von CCl₄ hergestellt und dann zwischen 230 und 250 nm angeregt. Es wurde beobachtet, dass CCl₃ über verschiedene Kanäle dissoziieren kann. Der erste Kanal ist eine Prädissoziation, die auf einer Zeitskala ähnlich der Rotationsperiode von CCl₃ stattfindet. Dabei entsteht CCl₂ und Cl. Bei kurzen Wellenlängen wird eine Anisotropie beobachtet, die jedoch unter 240 nm anfängt zu verschwinden. Die Energieverteilung bleibt jedoch gleich. Daraus lässt sich schließen, dass der Dissoziationspfad unabhängig von der Wellenlänge ist, jedoch existiert eine Barriere im angeregten Zustand, die aber bei hohen Anregungsenergien schnell überwunden werden kann. Wenn jedoch die Anregungsenergie erniedrigt wird, muss mehr Energie im Molekül

umgelagert werden, wodurch die Dissoziation langsamer verläuft. Dadurch geht die Anisotropie verloren und das Bild wird isotrop. Der zweite Pfad ist ein statistischer Prozess, der zur Fragmentierung in CCl und Cl_2 führt. Mehrere verschiedene Beiträge überlappen im CCl Bild. Zusätzlich zu CCl Fragmenten aus der Dissoziation von CCl_3 tragen CCl Fragmente aus der Dissoziation von CCl_2 zu der Energieverteilung bei. Außerdem ist ein breites Hintergrundsignal vorhanden. Deshalb war es nicht möglich, genaue Aussagen über diesen Dissoziationspfad zu erhalten. Jedoch scheint dieser Pfad eine isotrope Energieverteilung zu besitzen, deren Form einem statistischen Dissoziationskanal ähnelt.

Um die Beiträge, die zum CCl Bild in der CCl_3 Untersuchung führen, besser zu verstehen, wurden Messungen der Photodissoziation von CCl_2 durchgeführt. Das CCl_2 wurde durch die Flash-Pyrolyse von CHCl_3 erzeugt. Es konnte gezeigt werden, dass CCl_2 ein weitere Quelle für Chlor in der Atmosphäre ist, da es durch die Absorption eines UV Photons in CCl und Cl über zwei verschiedene Kanäle zerfällt. Bei dieser Studie wurden die gleichen Wellenlängen wie bei der CCl_3 Studie verwendet. Beide Pfade überlappen und das Bild zeigt einen breiten Hintergrund. Jedoch kann gesagt werden, dass einer der Pfade einer direkten Dissoziation entspricht, bei dem ca. 48% der Überschussenergie in Translationsenergie fließt. Der Anisotropieparameter liegt etwa bei 1. Der zweite Kanal kann wegen der Überlappung mit dem direkten Prozess nicht eindeutig zugeordnet werden. Jedoch scheint dieser zweite Kanal eine Energieverteilung zu erzeugen, die isotrop ist, dessen Form ähnlich zu einer statistischen Dissoziation oder einer Prädissoziation ist.

Contents

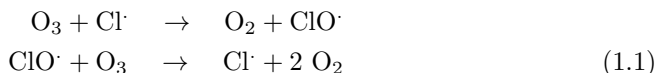
1	Introduction	1
1.1	Photodissociation	2
1.1.1	Angular Distribution	4
1.1.2	Photodissociation Studies	6
1.2	Bibliography	8
2	Methods and Experimental Setup	11
2.1	Molecular Beam Technique	11
2.1.1	Pyrolysis	13
2.2	Time-of-Flight Mass Spectrometry	13
2.2.1	Time-of-Flight Mass Spectrometry Setup	14
2.3	Photoionization	17
2.3.1	Single Photon Ionization	17
2.3.2	Resonance-Enhanced Multiphoton Ionization	18
2.3.2.1	Chlorine Ionization	19
2.4	Velocity Map Imaging	22
2.4.1	Experimental Details of the Velocity Map Imaging Setup	25
2.4.2	Image Reconstruction	26
2.4.2.1	Inverse Abel-Transform	28
2.4.2.2	Basis Set Expansion and Polar Basis Set Expansion	29
2.4.3	Data Analysis	30
2.4.4	Data Acquisition	33
2.5	Optimizing Experimental Parameters	34
2.6	Bibliography	38
3	Photodissociation of Benzoyl Chloride: A Velocity Map Imaging Study Using VUV Detection of Chlorine Atoms	41
3.1	Abstract	41
3.2	Introduction	41
3.3	Methods	43
3.4	Results	45
3.5	Discussion	54
3.6	Conclusion	58
3.7	Acknowledgements	59
3.8	Supplementary Information	60
3.9	Bibliography	69
4	Photodissociation of the trichloromethyl radical: photofragment imaging and femtosecond photoelectron spectroscopy	73
4.1	Abstract	73
4.2	Introduction	73

4.3	Experimental	75
4.4	Results	76
4.4.1	Calculations	76
4.4.2	Mass spectra	77
4.4.3	Time-resolved experiments	78
4.4.4	Nanosecond photofragment imaging	81
4.5	Discussion	89
4.6	Conclusions	94
4.7	Conflicts of interest	94
4.8	Acknowledgements	95
4.9	Supplementary Information	95
4.9.1	Further Experimental Details	95
4.10	Bibliography	103
5	Velocity Map Imaging Study of the Photodissociation of Dichloro- carbene in the VUV	107
5.1	Abstract	107
5.2	Introduction	107
5.3	Experimental	108
5.4	Results	109
5.4.1	Mass spectra	109
5.4.2	Velocity map imaging	110
5.5	Discussion	115
5.6	Conclusion	118
5.7	Supplementary Information	119
5.8	Bibliography	123
6	Summary	125

1 Introduction

Already in the mid 19. century it was discovered that various gases have the property of being able to trap heat in the atmosphere very well resulting in the now called greenhouse effect.¹ Shortly afterwards, Arrhenius determined that the combustion of fossil fuels may result in the global warming we observe today.^{2,3} These studies mainly focused on the influence of CO₂ and it was suggested that a doubling of the CO₂ concentration in the atmosphere would lead to a 5°C increase in temperature. However, at that time it was still thought that any increase in CO₂ through burning of fossil fuels was insignificant and water vapor was a much more influential greenhouse gas. Starting in the 1950s renewed interest in this topic arose⁴ and by the 1980s with the increase of the mean global temperature being recorded,⁵ the problem of man made climate change was recognized. Nowadays it is known, that molecules besides CO₂ can have an even greater influence as a greenhouse gas.⁶⁻⁸ This is because the concentration of CO₂ in the atmosphere is close to a saturation in the absorption, meaning that a large increase in CO₂ results only in a small increase in the warming process. On the other hand, molecules like CH₄, Chlorofluorocarbons (CFCs) and Hydrochlorofluorocarbons (HCFCs) have a relatively low concentration in the atmosphere resulting in a linear increase in concentration also increasing the warming potential of these molecules linearly. A simple molecule like tetrachloromethane (CCl₄) has a 100-year global warming potential of over 1000 times that of CO₂.⁹ CCl₄ is a CFC that was widely used in various applications, like as a solvent, as a fire suppressant or as a refrigerant and consequently large amounts of it were released into the atmosphere.

But more than as a contributor to the greenhouse effect, CCl₄ and other CFCs and HCFCs are known for their role as ozone depleting substances (ODS).¹⁰ Our ozone (O₃) layer protects life on earth from harmful UV radiation in the range of 200 to 300 nm. In 1974 it was discovered that CFCs play an important role in the catalytic destruction of the ozone layer.¹¹ The UV light that is still present in the stratosphere allows for the photodissociation of the HCFCs and CFCs releasing halogen atoms, mainly chlorine. This chlorine reacts with the ozone in the stratosphere via reaction (1.1). Per reaction two O₃ molecules get destroyed and at the end the halogen atom remains, being able to perform this reaction again.



Because of the widespread use of CFCs and their release into the atmosphere, holes in the ozone layer over the earth's poles were generated. When this effect was discovered, the member states of the United Nations ratified the Montreal

Protocol (1987).¹² With this it was decided, that the commercial use of CFCs was to be phased out until 2010 and that of HCFCs until 2030. Because of this the use of CCl_4 for commercial use has been banned, however it is still used in a scientific setting. In addition, CCl_4 has a lifetime of around 32 years,¹³ which is why even though the commercial use has been banned for over 10 years, roughly 90% of the amount that was in the atmosphere at the time of the ban still remains.^{14,15} However, these actions by the international community have caused the ozone layer to begin to recover.¹⁶⁻¹⁸

1.1 Photodissociation

The CFCs and HCFCs that play a major role in the destruction of stratospheric ozone need to be stable enough to rise up into those heights. Molecules like chloroform are comparatively unstable and have only a short lifetime inside our atmosphere before they absorb light and subsequently dissociate. Still, even these short-lived species contribute to the destruction of the ozone layer.¹⁹⁻²¹ Therefore, it is important to understand how the chlorine that acts as a catalyst in the destruction of ozone is generated. In other words, the study of the photodissociation dynamics of CFCs and HCFCs must be carried out.^{22,23}

Upon absorption of a UV photon that is still present in the stratosphere, a molecule AB goes into an excited state AB^* . Once in the excited state, the molecule wants to return to its ground state, relinquishing its excess energy. It can either send out light via fluorescence or phosphorescence or it can go back into its ground state via vibrational relaxation.²⁴ If the energy of the excited state is higher than the weakest bond inside the molecule, it is also possible to split this bond, fragmenting the molecule. Depending on the states involved, this photodissociation can take place in different ways. A distinction is made between direct and indirect dissociation pathways. These dissociation pathways compete with the other deactivation processes inside the molecule.

If the molecule gets excited into a repulsive electronic state (Figure 1.1 pink), the bond in the molecule gets directly broken, typically resulting in two separate fragments A and B, hence the name "direct dissociation". This kind of dissociation takes place on a very fast time scale, usually within a few femtoseconds.^{25,26}

If the molecule however gets excited into a bound state, it cannot immediately dissociate. A process leading to a dissociative state has to take place first, resulting in these processes to take longer than a direct dissociation. One differentiates between three different indirect dissociation pathways: Herzberg type-I predissociation, Herzberg type-II predissociation, and dissociation after relaxation into the vibrationally highly excited ground state.

For a Herzberg-type-I-predissociation, a repulsive state has to exist that is accessible from the bound state via internal conversion (IC). As seen in orange in Figure 1.1, a conical intersection allows for the IC into the repulsive state.

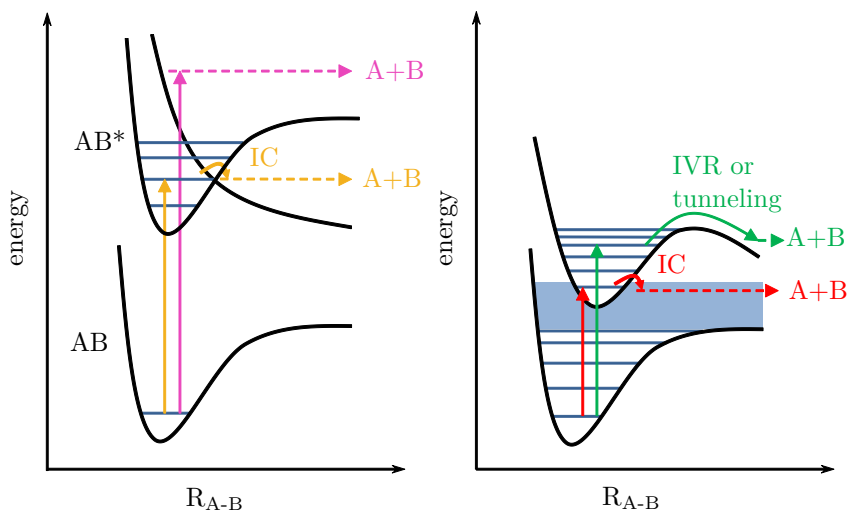


Figure 1.1: Schematic description of the various dissociation pathways. In pink a direct dissociation from an excited state is shown. The orange pathway is a Herzberg type-I predissociation where a excited states goes into a dissociative state via IC. The molecule can also dissociate from a excited state with a barrier after IVR or tunneling through the barrier (green). The last possibility shown in red is a dissociation from a highly vibrationally excited ground state.

If the molecule is in an excited state that has a barrier preventing dissociation, this barrier has to be overcome first before dissociation can occur (Figure 1.1 green). Two possible mechanisms can result in this outcome. Either vibrational energy gets redistributed inside the molecule (Intramolecular vibrational energy redistribution (IVR)) resulting in the required energy to be gained from other vibrational modes, or the barrier can be overcome by quantum tunnelling. These pathways are classified as Herzberg-type-II-predissociation.^{22,25}

The third indirect dissociation pathway, also called a statistical dissociation, occurs when the excited state AB^* shows a significant IC-rate to the ground state. This results in a rovibrationally highly excited ground state from where the rovibrational energy can be redistributed into the mode that can lead to a dissociation. If enough energy gets redistributed into this mode, dissociation occurs.^{24,27}

As mentioned previously, the energy of the photon $E_{h\nu}$ absorbed by the molecule needs to exceed the bond dissociation energy (BDE) of the bond that should be cleaved. The various energetic components that play a role in this are as follows:

$$E_{h\nu} + E_{int}(AB) + E_T(AB) = BDE + E_{int}(A) + E_{int}(B) + TKER \quad (1.2)$$

The E_{int} are the internal energies (vibrational, rotational and electronic) of the molecule AB and the fragments A and B respectively. $E_T(AB)$ is the translational energy of the molecule before dissociation and TKER is the total kinetic energy release of the fragments after dissociation which is the sum of the kinetic energies of the various fragments.²⁸

Depending on the experimental setup, it is possible to minimize $E_{int}(AB)$ and therefore it can be neglected. Also, $E_T(AB)$ can be neglected for various analysis methods. This will be described later in section 2. With this Equation 1.2 can be simplified to:

$$E_{h\nu} = BDE + E_{int}(A) + E_{int}(B) + TKER \quad (1.3)$$

For the extreme cases in which all energy goes into translational energy ($E_{int}(A) = E_{int}(B) = 0$), Equation 1.3 can be rewritten to

$$E_{h\nu} = BDE + E_T^{max}(A) + E_T^{max}(B) \quad (1.4)$$

where E_T^{max} is the maximum kinetic energy for either fragment.²⁹ Since during such a photodissociation process energy and momentum need to be conserved, one can get the maximum kinetic energy for fragments A and B as:

$$E_T^{max}(A) = (E_{h\nu} - BDE) \cdot \frac{m_B}{m_{AB}} \quad E_T^{max}(B) = (E_{h\nu} - BDE) \cdot \frac{m_A}{m_{AB}} \quad (1.5)$$

Here, $m_{A,B,AB}$ are the masses of the fragments and the parent molecule.

If summing over multiple dissociation events, fragments with the same energy and the same starting position are distributed over sphere, called the Newton sphere. Each dissociation event produces a fragment A and a fragment B, flying in opposite directions because of conservation of momentum and ending up on its respective Newton sphere. This is schematically shown in Figure 1.2.

1.1.1 Angular Distribution

Another important aspect for the dissociation process is the angle between transition dipole moment $\vec{\mu}$ and the bond \vec{k} that is getting dissociated (θ). If linearly polarized light is used, a molecule will best absorb light, if it is orientated in a way that the transition dipole moment is parallel to the polarization axis of the light. If the polarization is turned by 90° , the molecule will not

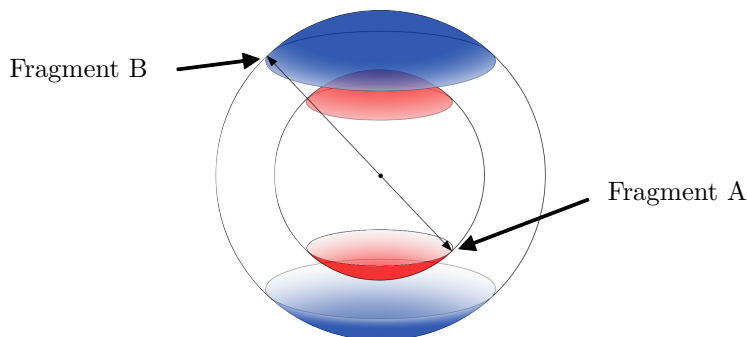


Figure 1.2: Schematic of the Newton spheres generated in a photodissociation process. The red and blue regions are the Newton spheres that get spanned by summing over many dissociation events of the respective fragment.

absorb. If θ is 0° , meaning that the transition dipole moment is parallel to the bond getting dissociated, the resulting fragments will mostly be located on the poles in z-direction on the Newton sphere (see Figure 1.3). Increasing the angle reduces the concentrated region at the poles of the Newton sphere, making the distribution more isotropic. At 54.7° the distribution is completely isotropic and increasing the angle further results in particles to start concentrating around the equator of the sphere. Once θ equals 90° , one gets a belt around the equator of the Newton sphere (see Figure 1.3).

This angular distribution of fragments $I(\theta)$ on the Newton sphere can be described by the standard recoil anisotropy function:^{22,25,29}

$$I(\theta) = N \cdot [\beta P_2(\cos(\theta))] \quad (1.6)$$

N is a normalization factor, β is called the anisotropy parameter and $P_2(\cos(\theta))$ is the second order Legendre polynomial with the cosine of the angle as its parameter:

$$P_2(\cos(\theta)) = \frac{1}{2}(3 \cos^2(\theta) - 1) \quad (1.7)$$

The β -value becomes 2 when θ is 0° and -1 for 90° . At an angle of $\theta = 54.7^\circ$, β becomes 0. This is also called the magical angle.

This kind of angular distribution can only be observed if the dissociation process takes place within the time frame of the rotational period of the molecule,

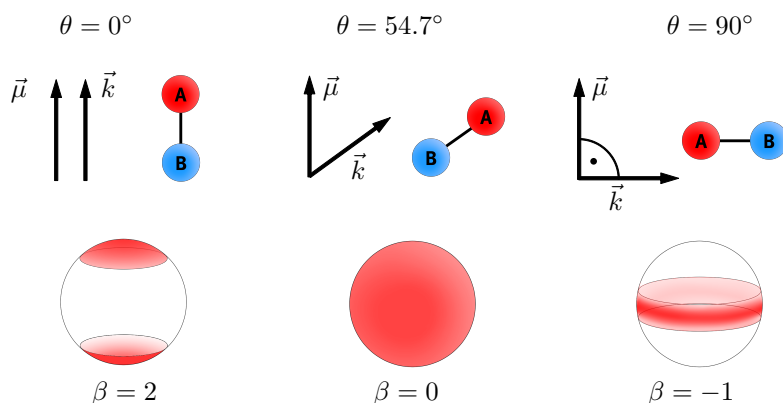


Figure 1.3: Newton sphere for different angles between transition dipole moment $\vec{\mu}$ and the bond that is broken \vec{k} . If the angle is 0° the fragments fly mainly towards the poles, resulting in a β -value of 2. At 54.7° the distribution becomes isotropic and β is 0. For an angle of 90° , a belt around the equator is formed and β becomes -1.

since otherwise the molecule starts rotating and the angular distribution is lost. That is why anisotropic distributions are mainly observed only for direct dissociations since these take place on a femtosecond time scale. Additionally, direct dissociations have a relatively high average kinetic energy of around 50% of the excess energy flowing into kinetic energy. On the other hand, indirect dissociations usually show an isotropic distribution of fragments and an average kinetic energy of around 15% to 25%.

1.1.2 Photodissociation Studies

Besides recording photoabsorption spectra, the photodissociation process of various CFCs and HCFCs have been studied in order to better understand the formation of chlorine atoms in the atmosphere.³⁰⁻³² Molecules like CCl_4 ³³ and CHCl_3 ³⁴ have already been studied in great detail. On the other hand, the radicals that get released after photolysis of these species have only been studied in much less detail, since, compared to the stable precursors, the radicals themselves have to be generated in situ, complicating the experiments tremendously. Limited studies on CCl_2 ,³⁵⁻³⁷ CCl_3 ³⁸ and CH_2Cl ^{39,40} have been done. In the past, measuring the time-of-flight mass spectrum after photodissociation was used for gaining information on the TKER of the photodissociation process.^{38,41} However, nowadays velocity map imaging (VMI) is the method of choice.^{29,42} The VMI method allows for the recording of a 2D representation of the Newton sphere (described in section 2 in greater detail). Using mathemat-

ical reconstruction methods, the original 3D kinetic energy distribution can be recovered. The technique was developed by A. Eppink and D. Parker⁴³ and has application not only for studying photodissociation dynamics but is also used for photoelectron spectroscopy,⁴⁴⁻⁴⁶ molecular scattering experiments^{47,48} and studying dissociative photoionisation.^{49,50}

In this work, the photodissociation of various chlorine containing molecules was examined with the VMI technique, gaining insight into the photodissociation dynamics of benzoyl chloride, CCl_3 , and CCl_2 . The thesis is structured as follows:

In section 2, the method of velocity map imaging and other fundamental aspects related to the experiments are explained. Also information on the experimental setup will be given.

Section 3 shows the work done on benzoyl chloride.⁵¹ Benzoyl chloride was examined in order to establish a new ionization method for atomic chlorine, since conventional ionization methods result in large background signals. This is due to an overlap in the absorption spectrum of benzoyl chloride and the wavelength used to ionize chlorine. Benzoyl chloride is the simplest aromatic acid chloride and has been studied in the past, showing that chlorine is released upon dissociation in the region of 235 nm.⁴¹ As such it was chosen as a suitable substance for establishing the new chlorine detection method.

The photodissociation of CCl_3 is then discussed in section 4. The CCl_3 is generated via pyrolysis of CCl_4 . Past studies have shown that CCl_4 is dissociated to CCl_3 , which is a major contributor to stratospheric chlorine, resulting in the destruction of ozone. The CCl_3 that is generated via photolysis still remains in the stratosphere and only limited studies on its photodissociation dynamics have been conducted in the past. Since our apparatus allows easy in situ generation of radicals, it was decided to look at this little studied radical in order to better understand what happens with the remaining CCl_3 in the stratosphere. In section 4, it is shown that CCl_3 dissociates both into $\text{CCl} + \text{Cl}_2$ as well as into CCl_2 and Cl .⁵²

In section 5, a study conducted on CCl_2 that is generated via pyrolysis of CHCl_3 is presented. The CCl_2 is dissociated and subsequently the photodissociation dynamics are examined. Since it is shown in section 4 that CCl_3 easily dissociates into CCl_2 , CCl_2 is a further relevant chlorine containing radical in the stratosphere, that can have an impact on ozone depletion. Upon UV excitation, it was discovered that CCl_2 efficiently dissociates into CCl over two separate pathways.

Lastly, in section 6, a summary of the results and an outlook on current and future research is given.

1.2 Bibliography

- (1) Tyndall, J. *Philos. Trans. Royal Soc.* **1861**, *151*, 1–36.
- (2) Arrhenius, P. S. *Lond. Edinb. Dublin philos. mag. j. sci.* **1896**, *41*, 237–276.
- (3) Arrhenius, S. *Publ. Astron. Soc. Pac.* **1897**, *9*, 14.
- (4) Benedict, W.; Plyler, E. *J. Res. Natl. Bur. Stand. (U. S.)* **1951**, *46*, 246.
- (5) Hansen, J.; Johnson, D.; Lacis, A.; Lebedeff, S.; Lee, P.; Rind, D.; Russell, G. *Science* **1981**, *213*, 957–966.
- (6) Ramanathan, V. *Science* **1975**, *190*, 50–52.
- (7) Wang, W. C.; Yung, Y. L.; Lacis, A. A.; Mo, T.; Hansen, J. E. *Science* **1976**, *194*, 685–690.
- (8) Ramanathan, V.; Cicerone, R. J.; Singh, H. B.; Kiehl, J. T. *J. Geophys. Res. Atmos.* **1985**, *90*, 5547–5566.
- (9) Hodnebrog, A.; Aamaas, B.; Fuglestad, J. S.; Marston, G.; Myhre, G.; Nielsen, C. J.; Sandstad, M.; Shine, K. P.; Wallington, T. J. *Rev. Geophys.* **2020**, *58*, e2019RG000691.
- (10) Kaufman, F. *SAE Transactions* **1977**, *86*, 58–77.
- (11) Molina, M. J.; Rowland, F. S. *Nature* **1974**, *249*, 810–812.
- (12) Secretariat, U. N. O. The Montreal Protocol on Substances that Deplete the Ozone Layer, 1987, <https://ozone.unep.org/treaties/montreal-protocol>, accessed 20.10.2022.
- (13) Butler, J. H.; Yvon-Lewis, S. A.; Lobert, J. M.; King, D. B.; Montzka, S. A.; Bullister, J. L.; Koropalov, V.; Elkins, J. W.; Hall, B. D.; Hu, L.; Liu, Y. *Atmospheric Chem. Phys.* **2016**, *16*, 10899–10910.
- (14) Prinn, R. G. et al. *Earth Syst. Sci. Data* **2018**, *10*, 985–1018.
- (15) Prinn, R. G. et al. History of chemically and radiatively important atmospheric gases from the Advanced Global Atmospheric Gases Experiment (AGAGE), 2018, <https://data.ess-dive.lbl.gov/datasets/doi:10.3334/CDIAC/ATG.DB1001>. accessed: 20.10.2022].
- (16) Solomon, S.; Ivy, D. J.; Kinnison, D.; Mills, M. J.; Neely, R. R.; Schmidt, A. *Science* **2016**, *353*, 269–274.
- (17) Kuttippurath, J.; Nair, P. J. *Sci. Rep.* **2017**, *7*, 1–8.
- (18) Kuttippurath, J.; Kumar, P.; Nair, P. J.; Pandey, P. C. *NPJ Clim. Atmos. Sci.* **2018**, *1*, 1–8.
- (19) Hossaini, R.; Chipperfield, M. P.; Montzka, S. A.; Rap, A.; Dhomse, S.; Feng, W. *Nat. Geosci.* **2015**, *8*, 186–190.

-
- (20) Hossaini, R.; Chipperfield, M. P.; Montzka, S. A.; Leeson, A. A.; Dhomse, S. S.; Pyle, J. A. *Nat. Commun.* **2017**, *8*, 1–9.
- (21) Liang, Q.; Strahan, S. E.; Fleming, E. L. *Science* **2017**, *358*, 1257–1258.
- (22) Sato, H. *Chem. Rev.* **2001**, *101*, 2687–2725.
- (23) Butler, L. J.; Neumark, D. M. *J. Phys. Chem.* **1996**, *100*, 12801–12816.
- (24) Albert, S.; Albert, K. K.; Hollenstein, H.; Tanner, C. M.; Quack, M., *Handbook of High-resolution Spectroscopy*; John Wiley & Sons, Ltd: 2011.
- (25) Schinke, R. *Photodissociation Dynamics* **1993**.
- (26) Baer, T.; Hase, W. L., *Unimolecular reaction dynamics : theory and experiments*; Oxford University Press: 1996, p 438.
- (27) Alcaraz, C.; Fischer, I.; Schröder, D., *Encyclopedia of Radicals in Chemistry, Biology and Materials*; Studer, A., Ed.; John Wiley & Sons, Ltd: 2012.
- (28) Busch, G. E.; Mahoney, R. T.; Morse, R. I.; Wilson, K. R. *J. Phys. Chem.* **2003**, *51*, 449.
- (29) *Imaging in Molecular Dynamics: Technology and Applications*; Whitaker, B. J., Ed.; Cambridge University Press: 2003.
- (30) Deshmukh, S.; Hess, W. P. *J. Phys. Chem.* **1998**, *100*, 6429.
- (31) Morton, M. L.; Butler, L. J.; Stephenson, T. A.; Qi, F. *J. Phys. Chem.* **2002**, *116*, 2763.
- (32) Lin, J. J.; Chen, Y.; Lee, Y. Y.; Lee, Y. T.; Yang, X. *J. Phys. Chem.* **2002**, *361*, 374–382.
- (33) Kawasaki, M.; Suto, K.; Sato, Y.; Matsumi, Y.; Bersohn, R. *J. Phys. Chem.* **1996**, *100*, 19853–19858.
- (34) Reid, M.; Green, V.; Koehler, S. P. *Phys. Chem. Chem. Phys.* **2014**, *16*, 6068–6074.
- (35) Shin, S. K.; Dagdigian, P. J. *J. Phys. Chem.* **2006**, *125*, 133317.
- (36) Shin, S. K.; Dagdigian, P. J. *Phys. Chem. Chem. Phys.* **2006**, *8*, 3446–3452.
- (37) Shin, S. K.; Dagdigian, P. J. *J. Phys. Chem.* **2008**, *128*, 154322.
- (38) Hintsä, E. J.; Zhao, X.; Jackson, W. M.; Miller, W. B.; Wodtke, A. M.; Lee, Y. T. *J. Phys. Chem.* **1991**, *95*, 2799–2802.
- (39) Levchenko, S. V.; Demyanenko, A. V.; Dribinski, V. L.; Potter, A. B.; Reisler, H.; Krylov, A. I. *J. Phys. Chem.* **2003**, *118*, 9233.
- (40) Dribinski, V.; Potter, A. B.; Demyanenko, A. V.; Reisler, H. *J. Phys. Chem.* **2001**, *115*, 7474.

- (41) Saha, A.; Kawade, M.; Sengupta, S.; Upadhyaya, H. P.; Kumar, A.; Naik, P. D. *J. Phys. Chem.* **2014**, *118*, 1185–1195.
- (42) Basnayake, G.; Ranathunga, Y.; Lee, S. K.; Li, W. *J. Phys. B: At. Mol. Opt. Phys.* **2022**, *55*, 023001.
- (43) Eppink, A. T.; Parker, D. H. *Rev. Sci. Instrum.* **1998**, *68*, 3477.
- (44) Lehmann, C. S.; Ram, N. B.; Powis, I.; Janssen, M. H. *J. Phys. Chem.* **2013**, *139*, 234307.
- (45) Neumark, D. M. *J. Phys. Chem.* **2008**, *112*, 13287–13301.
- (46) Bodi, A.; Johnson, M.; Gerber, T.; Gengeliczki, Z.; Sztáray, B.; Baer, T. *Rev. Sci. Instrum.* **2009**, *80*, 034101.
- (47) Lin, J. J.; Zhou, J.; Shiu, W.; Liu, K. *Rev. Sci. Instrum.* **2003**, *74*, 2495.
- (48) Sarma, G.; Marinakis, S.; Meulen, J. J. T.; Parker, D. H.; McKendrick, K. G. *Nat. Chem.* **2012**, *4*, 985–989.
- (49) Lebech, M.; Houver, J. C.; Doweck, D. *Rev. Sci. Instrum.* **2002**, *73*, 1866.
- (50) Parker, D. H.; Eppink, A. T. *J. Phys. Chem.* **1998**, *107*, 2357.
- (51) Matthaiei, C. T.; Mukhopadhyay, D. P.; Fischer, I. *J. Phys. Chem.* **2021**, *125*, 2816–2825.
- (52) Matthaiei, C. T.; Mukhopadhyay, D. P.; Röder, A.; Poisson, L.; Fischer, I. *Phys. Chem. Chem. Phys.* **2022**, *24*, 928–940.

2 Methods and Experimental Setup

Many methods for the study of molecules are available, each giving insights into different properties of them. Depending on the method, the to be examined species is either in the solid, the liquid or the gaseous phase. When studying radicals however, usually only gas-phase spectroscopic methods are applicable. This is because in general radicals have very low reaction barriers, where practically every interaction with another radical will result in a recombination of the two. In gas-phase experiments the mean distance between individual radicals is sufficiently large that the recombination is relatively unlikely.¹ Also, gas-phase experiments allow for the study of the pure characteristics of a molecule since no interactions between molecules, and molecule and solvent are present.

In this chapter, the generation of radicals is described. Afterwards, the measurement methods used in this work are presented. The methods of time-of-flight mass spectrometry and velocity map imaging were used. The utilized experimental apparatus is described in combination with the method. Subsequently, the analysis method used for interpreting the results is presented and used software is described.

2.1 Molecular Beam Technique

In order to get molecules into the gas phase, the use of the molecular beam technique was chosen for the here presented work.^{2,3} For generating a molecular beam, molecules are seeded in an inert gas, usually helium or argon, and then adiabatically expanded into a high vacuum chamber. Either a small hole can be used as the opening into the vacuum chamber, creating a continuous molecular beam, or a solenoid pulsed valve creating a periodic short burst of molecules released into vacuum. Upon expansion into vacuum, the unoriented kinetic energy of the molecules inside the valve gets oriented in the direction of the vacuum. The molecules are accelerated to supersonic speeds. This process is schematically shown in Figure 2.1. Collisions between the molecules and the carrier gas result in the speed of the molecules to converge to a mean speed.⁴ At the same time the carrier gas absorbs the internal energy of the molecules, resulting in a cooling of the rotation and vibration energy. Very low temperatures in the region of a few kelvin can be achieved. Because of this, only very few (ro-) vibrational levels are excited, allowing for sharp absorption spectra to be recorded. This cooling effect also reduces the influence of the internal energy on a photodissociation process (see Equation 1.2). Upon exiting the valve, the molecules expand in a conical shape, having a small translational energy contribution along the plane perpendicular to the exit direction from the nozzle. Because of the sudden expansion into vacuum, shock waves at the boarder of this molecular beam cone are formed (barrel shock).⁵ This increases the temperature of the molecules in the outer region of the cone. The molecular

beam then passes through a skimmer, a thin hollow cone, typically made from nickel, with a hole in its tip. This skimmer cuts off the outer portions of the molecular beam, leaving only the well cooled center part.⁶ Also, since only those molecules that had a velocity vector in the direction of the skimmer hole can pass through it, the translational energy distribution gets narrowed even further. This is called geometrical cooling.

As just mentioned, usually argon (Ar) or helium (He) are used as carrier gases. This is because of their low reactivity and good cooling efficiency. As long as the carrier gas is unreactive, also other carrier gases can be used, like nitrogen (N_2). Ar has higher mass and can absorb energy from the molecule being investigated more efficiently. However, it is prone to generating Ar-clusters with the molecule. Helium on the other hand does not cool as efficiently as argon but it does not create clusters as easily. Also the signal strength of the experiments being conducted is usually higher with He.

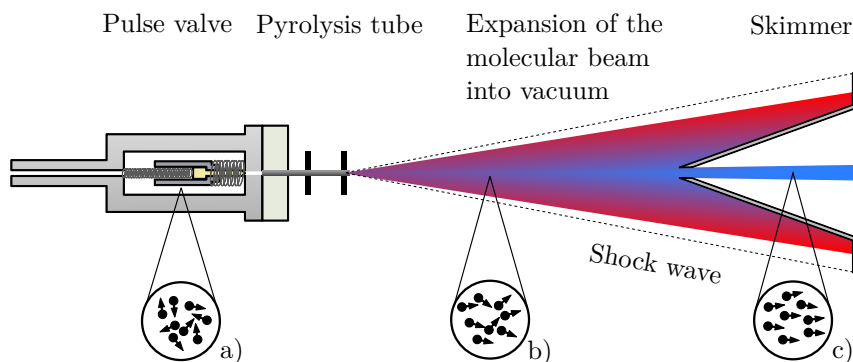


Figure 2.1: Schematic of the generation of the molecular beam. At the beginning, the motion of the molecules is unoriented inside the pulse valve (a). Then the molecules get expanded into the vacuum chamber, passing through a pyrolysis tube (SiC). The distribution of the kinetic energy gets focused into the direction of expansion, getting narrower with the amount of collisions (b)). The shock wave generated by the expansion is drawn as a dotted line. The middle part is cooled the most. The molecular beam then passes the skimmer, so that only the well cooled central region of the molecular beam remains (c)).

In this work, a solenoid pulsed valve, made by Parker is used (Series 9). It is controlled by a homebuilt device that allows for the regulation of the opening of the valve by the adjustment of the applied voltage. It is operated in a way, that the pulse valve only stays open for around $300 \mu\text{s}$. A Stanford Research DG535 delay generator is used to synchronize this pulse valve with other components described later. Typical temperatures of the molecular beam exiting this valve have been determined to be around $10 \pm 2 \text{ K}$.⁷ The molecular beam then passes through a nickel skimmer with a hole of around 2 mm in its tip.

2.1.1 Pyrolysis

For examining radicals and not only stable molecules, the radicals have to be generated in situ. One method is by heating a molecule up. Through the thermal energy imparted on the molecule a bond can be cleaved. This method of generating radicals is called pyrolysis. In the experimental setup used for the work presented in this study, a small pyrolysis tube was attached to the end of the pulse valve (see Figure 2.1). This small tube is made out of silicon carbide (SiC; Saint Gobain Keramik, Hexoloy SE SiC tube), an extremely high endurance material. The SiC tubes used in the experiments described in this thesis exhibited a resistance per unit length of about $30 \frac{\Omega}{\text{cm}}$. A voltage is applied to this tube, resistively heating it. The power applied is typically between 10 and 40 W, leading to the temperature of the tube rising up to around 2000 K. Molecules passing through this tube get heated, leading to a homolytic bond separation. This method is called flash pyrolysis. It has a very high conversion ratio of the precursor molecule and the bond that gets cleaved is fairly selective.^{8,9} Depending on the molecule, radicals that are not wanted might still be generated, making selective studies difficult in some cases. Because of this, the selection of the used precursor needs to be done carefully. Since these dissociations depend heavily on the thermal energy imparted on the molecule, molecules with one significantly weaker bond, e.g. a high atomic number halogen (bromine or iodine) attached to a carbon, are needed for a selective dissociation. This method however has the drawback that the molecules and the radicals generated from it have a very high internal energy and even the molecular beam technique cannot entirely cool these molecules. Typical temperatures for flash pyrolyzed molecules are around 150 to 300 K.¹⁰

Methods that do not entail a significant heating of the molecule encompass photolysis,^{11–13} fluorine abstraction^{14–16} and bond separation by electrical corona discharge.^{17,18} Photolysis allows for specific bonds to be cleaved selectively but its conversion ratio is very small. Abstracting hydrogen atoms from molecules using fluorine atoms is not selective and is also limited to molecules containing hydrogen. The electrical corona discharge leads to the molecules being fragmented in many different ways, making it difficult to interpret results. Pyrolysis has shown that it is a very useful tool for looking at CFC and HCFC radicals since there is a multitude of different precursors that allow for fairly selective pyrolysis.^{19,20}

2.2 Time-of-Flight Mass Spectrometry

A method used to investigate the fragments generated in a flash pyrolysis is time-of-flight (TOF) mass spectrometry (MS).^{21,22} In TOF MS, molecules and/or atoms are ionized inside a vacuum chamber. Then, an electric field is used to accelerate these charged particles in the direction of a detector. The

speed of the particle depends on its charge z , its mass m and the applied voltage U :

$$\frac{1}{2}m \cdot v^2 = z \cdot e \cdot U \quad (2.1)$$

Between the acceleration region and the detector is a field-free flight tube with the length d . Since particles with different masses get accelerated to different speeds, the spatial position of species with different masses gets separated and they reach the detector at different times. This time-of-flight t_{TOF} can be used for identifying the mass of an unknown substance and consequently identifying it:

$$t_{TOF} = \frac{d}{v} = \frac{d}{\sqrt{2eU}} \cdot \sqrt{\frac{m}{z}} \quad (2.2)$$

Knowing two masses present in a spectrum or having calibrated the apparatus with a known molecule beforehand, makes it possible to calibrate the spectrum, giving information about every signal recorded. Aceton ($m/z = 58$), that can be pyrolytically cleaved to acetyl ($m/z = 43$) is a convenient molecule for calibration since it gets ionized easily. Also, the typical isotopic distribution of molecules like Cl, that exists both as ^{35}Cl and ^{37}Cl in a ratio of 3:1, can be used to identify molecules in a mass spectrum, if limited knowledge of probable constituents is present.

In 1955, w. C. Wiley and I. H. McLaren showed that the resolution of TOF MS can be improved by using a specific arrangement of electrodes in the acceleration step.²³ It consists of three equally spaced electrodes, called ion optics. If the voltages applied to them are chosen correctly, all ions, independent on generation location, arrive on the detector at the same time. This allows for very high resolution mass spectra to be recorded.

2.2.1 Time-of-Flight Mass Spectrometry Setup

In this work, TOF MS was employed to identify the pyrolysis products generated from various precursors, in order to find a suitable precursor for generating specific radicals. Afterwards, the same setup was also utilized to identify the fragments generated by photodissociation from these radicals. Depending on the molecule and fragment being investigated, either a single laser that ionizes and dissociates can be used. Alternatively, two separate laser, one for dissociation and one for ionization, can be employed. Figure 2.2 shows a schematic representation of the used apparatus. On the bottom, a molecule gets carried from the sample container by the backing gas (Ar or He). It flows to the solenoid pulsed valve, passing through the pyrolysis tube expanding into the vacuum chamber. After the molecules pass through the skimmer, they enter

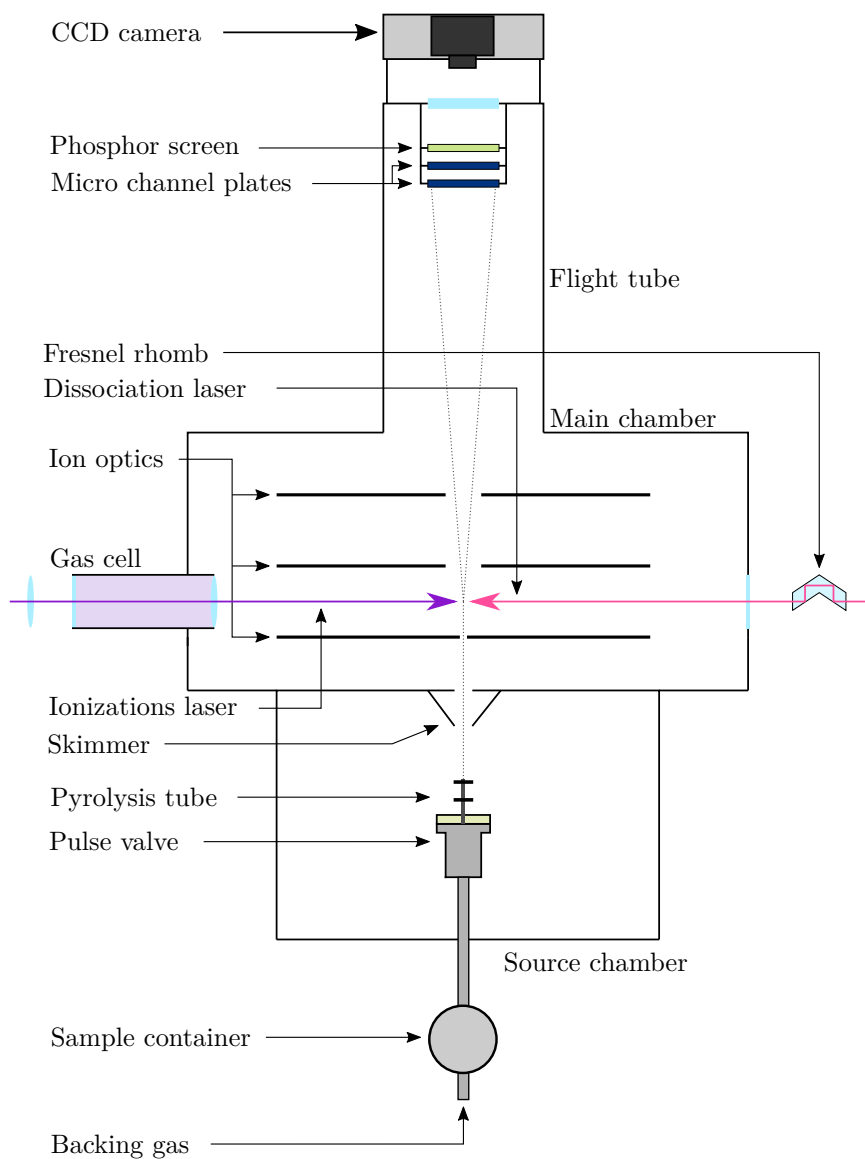


Figure 2.2: Schematic of in thesis used apparatus

the region where they are dissociated and ionized. Two separate lasers are used for these steps. Three stainless steel plates in the Wiley-McLaren arrangement

forming the ion optics are placed around this region and the electric field generated by them accelerates the ions towards the detector. The diameter of these plates is 88 mm. The bottom most plate, called repeller, has a hole of 5 mm in its center, from where the molecules entered this region. 5000 V are applied to this plate. The second and third plate have holes of 20 mm through which the ions fly towards the detector. The voltage applied to the second plate (extractor) was 4078 V. The third plate (ground) is grounded. The plates are 15 mm apart from each other.

After passing through the flight tube, the ions impact onto the detector consisting of two microchannel plates (MCP; tectra Physikalische Instrumente GmbH, MCP-50-D-L-VF-P43) with a diameter of 50 mm in a chevron configuration.²⁴ The front MCP is grounded and a voltage of 1.6 to 1.8 kV is applied to the second one. If an ion impacts on the first MCP, electrons are ejected from the material and subsequently amplified. The electrons pass through the tiny channels inside the material (about 12 μm), get accelerated towards the second MCP, impacting on it and further amplifying the electron cascade. This causes a lack of electrons inside the material which leads to a current to flow towards the MCPs. This current gets detected and amplified before being displayed on an oscilloscope. These short current peaks, which occur at different times depending on the m/z ratio for each species, are visible on the oscilloscope and represent the mass spectrum. This setup allows us to gain mass spectra with a resolution of $m/z < 1$.

The output of one of the two pulsed dye lasers was utilized for the dissociation step. The first is a Sirah Cobra-Stretch with a spectral resolution of 2.7 pm.²⁵ The second is a Sirah Precision Scan with a spectral resolution of 2.4 pm.²⁶ These dye lasers are pumped by either the second (532 nm) or third harmonic (354.67 nm) of Nd:YAG lasers. A Spectra Physics GCR-3 and a Spectra Physics Lab170 were used respectively. The output of the dye lasers is polarized horizontally. Dye lasers offer the great advantage over other types of laser systems, that they can produce light in a very broad range just by changing the used dye. Depending on the dye being used, the pump lasers wavelength has to be changed. Depending on dye and wavelength, the energy per pulse is around 20 to 40 mJ. This output was usually frequency doubled (second harmonic generation (SHG)) with a BBO crystal (β barium borate) (SHG wavelength: 215-280 nm) or a KDP (potassium dihydrogenphosphate) (SHG wavelength: 260-400 nm) resulting in output an energy per pulse between 10 and 60 mW depending on the dye. The output of dye lasers are extremely narrow in their wavelengths. All lasers operate at a repetition rate of 10 Hz and have a pulse duration of around 10 ns. The lasers were synchronized with the molecular beam with the already mentioned Stanford Research DG535 delay generator. This allows for precise excitation of molecular absorption bands or atomic lines. The process of ionization and the lasers used for this process are described in the following subsection.

2.3 Photoionization

Multiple types of photoionization are employed in order to generate the ions for the mass spectrometry, which are described below.

2.3.1 Single Photon Ionization

In order to ionize an atom or a molecule, one has to excite it above its ionization energy (IE). This creates a pair of a positively charged ion and an electron. The simplest method with which this can be achieved is using single photon ionization (SPI). Here, a particle A absorbs one photon with enough energy to excite it above the IE:



The excess energy above the IE flows into the kinetic energy of the ion-electron pair. However, since the electron is significantly lighter and momentum needs to be conserved, most of the kinetic energy goes to the electron. Only for very light ions (mainly atomic hydrogen) and considerable excess energies, the energy received by the ion can have an influence on its kinetic energy.

If the photon energy exceeds the IE of a molecule by a large margin, it can lead to the ion having enough energy to dissociate.²⁷ This is called dissociative photoionization (DPI). An ionic fragment A^+ , a neutral fragment B and a photoelectron e^- are generated in this process:



Typical IEs for CFCs, HCFCs and their radicals are around 8 eV and higher.²⁸ The radicals usually exhibit a lower IE than their respective precursors.²⁷ Light of this wavelength has to be generated inside a vacuum chamber, as air absorbs this wavelength very efficiently which would result in no photons reaching the vacuum chamber.²⁹

In the experiments described below, a pulsed neodymium-doped yttrium aluminum garnet(Nd:YAG) laser was used for SPI (Continuum Surelite II). This is a solid state laser with an emission wavelength of 1064 nm (1.165 eV) and a pulse duration of around 10 ns (10 Hz repetition rate). Its output is frequency tripled in a nonlinear crystal, resulting in a wavelength of 354.67 nm (3.50 eV) with an average power of around 160 mW. This light is then focused into a gas cell directly attached to the experimental apparatus. In this cell, the frequency is tripled again, generating 118.2 nm (10.49 eV) light. The exact process is explained in paragraph 2.3.2.1. The resulting photon energy is sufficient for ionizing most radicals generated from the pyrolysis of HCFCs and CFCs.

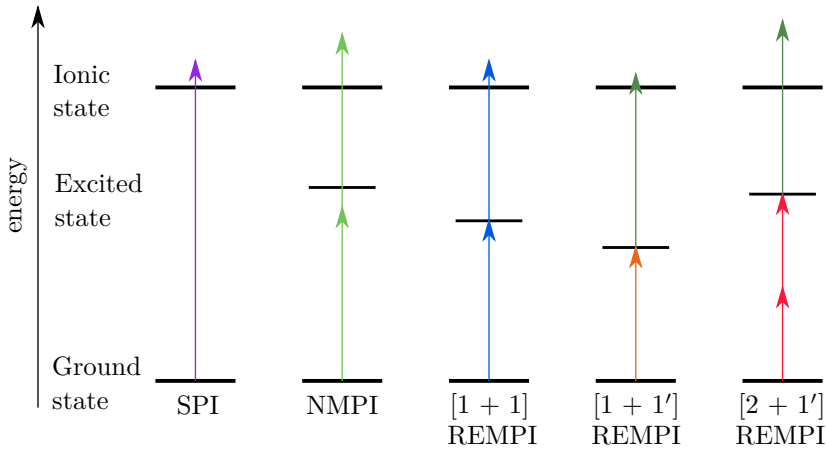


Figure 2.3: Schematic of different ionization schemes. The first is ionization with a single photon (SPI). The second is a two photon NMPI process where only a virtual state gets excited. The last three are various REMPI ionization schemes. In a first step a excited state gets excited before getting ionized in the second step.

2.3.2 Resonance-Enhanced Multiphoton Ionization

Another way to ionize a particle is by having it absorb multiple low energy photons. Two different types of this process can be differentiated, nonresonant multiphoton ionization (NMPI) and resonance-enhanced multiphoton ionization (REMPI). For NMPI, an atom or a molecule is excited into a virtual state by a photon from where it then absorbs more photons until it has absorbed enough photons to be excited above its IE (Figure 2.3 b)). As a nonlinear process involving n photons, this process is very inefficient because of the low transition dipole moment, decreasing with each additional photon required.³⁰ This process depends strongly on the light intensity. The efficiency is proportional to the intensity to the power of the amount of photons required, I^n . Considerable intensities are required for an NMPI process, meaning focused lasers are usually utilized.

On the other hand, for REMPI the particle absorbs a photon with an energy matching one of its excited states.^{31,32} From there, another photon gets absorbed, exciting the particle above its IP and creating an ion (Figure 2.3 c)). Since real states participate in this process, the cross section is considerably higher than for an NMPI process. Often easily available, low energy photons are utilized, resulting in more than two photons being needed to be absorbed. In the case that x photons are required for excitation into the excited state and y photons are required for excitation from the excited state into the ionic state, the notation of $[x + y]$ is used. This kind of process is still significantly

more efficient than a corresponding NMPI process which involves $z = x + y$ photons. Sometimes, in order to increase efficiency, two different wavelengths for the excitation and the ionization step are used. To denote that two different wavelengths are utilized, the notation of $[x + y']$ has been adopted. REMPI allows for efficient ionization of species with an IE higher than those accessible with conventional laser source with SPI.

2.3.2.1 Chlorine Ionization

In this work, a REMPI ionization scheme was used for ionizing chlorine atoms generated in photodissociation processes. Chlorine has an IE of 12.97 eV.³³ A typical limit for SPI in lab settings is around 10.5 eV (9th harmonic of a Nd:YAG laser). Because of this, SPI of chlorine is often not feasible. A well established method for ionizing chlorine is to use 235.34 nm light (5.27 eV, 44824.24 cm^{-1}) in a $[2 + 1]$ REMPI scheme.³⁴ This corresponds to the $4p \ ^2D_{3/2} \leftarrow 3p \ ^2P_{3/2}^o$ transition with subsequent ionization. Chlorine can also occur in a spin-orbit excited state (often denoted as Cl*). This state lies only 882 cm^{-1} (0.11 eV) above the ground state and can easily be produced in a dissociation process.³⁵ Therefore, it is necessary to also ionize this chlorine and examine it in order to gain a complete insight into a dissociation process. It is possible to ionize this Cl* via the $4p \ ^2S_{1/2}^o \leftarrow 3s \ ^2P_{1/2}^o$ transition, which is accessible using two photons with a wavelength of 235.21 nm (5.27 eV, 42517.79 cm^{-1}). This REMPI scheme has a nonlinear two-photon step required to reach the excited state and as such a focused laser beam is required. A graphical overview of the REMPI schemes is shown in Figure 2.4.

A output of one of the dye lasers was utilized for this. The standard method for generating light in this range is by using coumarin 102, which can be used to generate light in the range of 452 nm to 500 nm. This light is then passed through a BBO crystal which serves to double the frequency. This enables the generation of the required 235 nm light.

Another method that is sometimes utilizing is a $[3 + 1]$ REMPI process at 356.63 nm (3.48 eV, 28040.09 cm^{-1}) for ionizing Cl and 360.41 nm (3.44 eV, 27745.97 cm^{-1}) for the Cl*. This REMPI scheme first excites either state into the $4s \ ^2D_{5/2,3/2}$ state from where the chlorine then gets ionized. Pyridine 2 dye is usually used for this. It emits in a range of 667 to 751 nm and is then doubled by a KDP crystal. As a process involving three photons, this method is considerably less efficient than the $[2 + 1]$ process. When studying the photodissociation of CFCs, HCFCs, and their radicals, the $[2 + 1]$ method is often not suitable. This is due to the usually very broad and efficient absorption band in the region around 235 nm of these species. If 235 nm light is focused on these molecules, they often absorb multiple photons leading to a dissociation of the molecule with the resulting Cl fragments having various kinetic energies, depending on the amount of photons absorbed. These multiple contributions

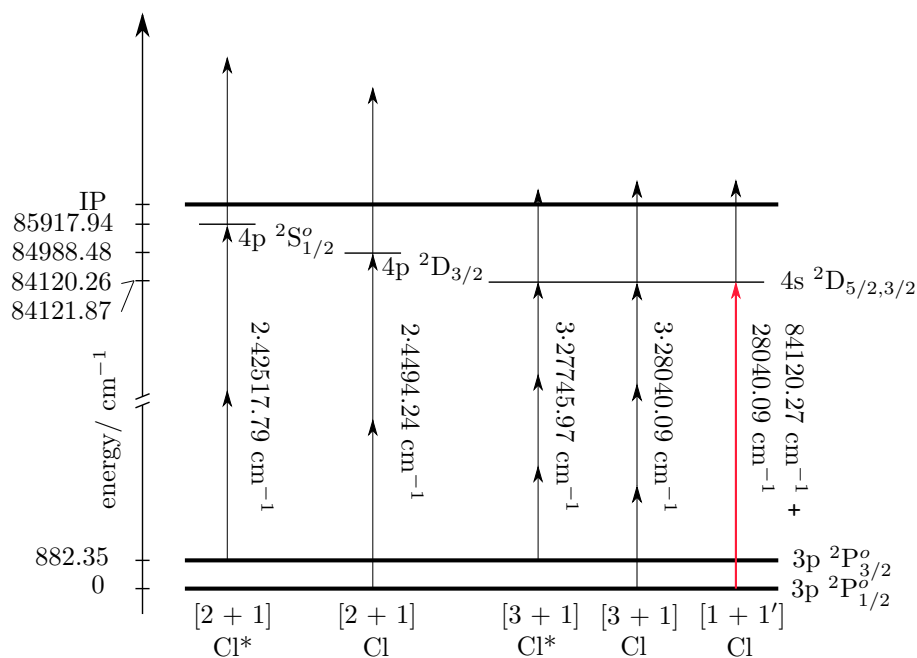


Figure 2.4: Representation of the different REMPI schemes used to ionize chlorine in this thesis. The red $[1 + 1']$ scheme is the one developed for the studies conducted in this work. The involved states are denoted besides the respective process and the required photon energies are shown.

to the kinetic energy of the Cl fragments make analysis of the photodissociation process difficult. Since these kinds of molecules usually do not absorb well or at all in the region around 356 nm, the $[3 + 1]$ REMPI scheme can be utilized without the drawbacks of the $[2 + 1]$ scheme. However, in the experiments presented in this thesis, the efficiency of this process was not high enough, resulting in no usable data being obtained.

To overcome these limitations, a new method for ionizing chlorine was developed, involving a $[1 + 1']$ REMPI scheme. It involves the transition of the chlorine atom into the same state as the $[3 + 1]$ process but with a single photon (118.88 nm, 10.43 eV, 84102.27 cm^{-1}), from where a second photon (356.63 nm) ionizes it. This scheme was realized by attaching a gas cell directly to the vacuum chamber and filling it with xenon. Xenon has a very high nonlinear refractive index and because it has a region of negative dispersion, it is possible to frequency triple light inside of it in these wavelength regions. These regions are between 113 and 117 nm, 117.2 and 119 nm, and between 126 and 129 nm.^{36,37} Other noble gases also have a comparatively high nonlinear

refractive index and allow for tripling in other regions. Krypton for example allows for tripling the 110-116 nm, and the 120-135 nm regions. The wavelength required for the excitation of Cl lies at the edge but still inside in the range of Xe making this process possible. The reported conversion efficiency is around 10^{-4} .³⁷

The second harmonic of a dye laser (356.63 nm) was focused with a 20 cm lens into the gas cell. Inside this cell the third harmonic gets generated and then focused into the ionization region of the TOF MS apparatus with a magnesium fluoride (MgF_2) lens. MgF_2 is used as a lens material because of its good transmission in this VUV region. Even though the 118.88 nm light gets focused into the ionization region, it does not produce a noticeable multiphoton absorption signal because its overall intensity is very small compared to the second harmonic of the dye laser. A schematic of this can be seen in Figure 2.5. The refractive index for 118.88 nm (third harmonic) and for 356.63 nm (fundamental) are vastly different, which is why the residual fundamental light is not focused into the vacuum chamber. This residual light does however act as the light ionizing the chlorine after the excitation to the excited state by the third harmonic.

Unfortunately, this method did not allow for the tripling of light which could excite Cl^* . Radziemski et al. report of a calculated Cl^* absorption line at 117.93 nm (10.51 eV, $84796,59 \text{ cm}^{-1}$) with an transition probability 2.5 higher than that of the transition at 118.88 nm.³⁵ It was tried to excite this line but no chlorine signal was found. It was also tried to find this atomic line with a [3 + 1] REMPI scheme but no signal was observed with this method either. Cantu et al. performed an intensive study of the absorption spectrum of atomic chlorine, reporting on more than 400 VUV absorption lines.^{38,39} However, even they did not find the calculated line at 117.93 nm. That is why it is most likely that either this transition is significantly perturbed or the intensity of this transition is significantly lower than calculated.

Even though this [1 + 1'] ionization method does not give us information about the spin-orbit excited chlorine, it allows for efficient excitation of ground state chlorine with only one photon, without the downsides of the [2 + 1] and [3 + 1] REMPI schemes. This allows for reliable data for at least the ground state of chlorine to be gathered.

The tripling efficiency inside the gas cell depends strongly on the Xe pressure and is a function of the wavelength. For the tripling process of 356.63 nm, the maximum efficiency is observed when the Xe pressure inside the chamber is around 2 mbar. The same xenon cell was used for tripling the frequency of the light used in the SPI process of the molecular fragments. For comparison, the pressure needed for maximum conversion at 354.67 nm is 13 mbar. The dependency of the conversion efficiency on the mixing ratio of Xe and Ar was also investigated. It was possible to get a Cl signal about 1.5 times higher than

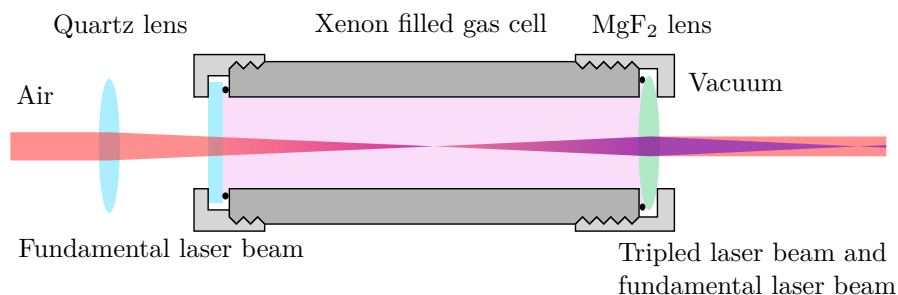


Figure 2.5: Schematic of the xenon filled gas cell used for tripling. A laser beam gets focused into the tripling cell where frequency tripled light is generated through third harmonic generation. This third harmonic and the residual fundamental light pass through a MgF_2 lens into the vacuum chamber. The third harmonic is focused into the region where molecules and atoms are to be ionized.

with pure Xe at a mixing ratio of 1:18 (106 mbar in the tripling cell). But considering the extra effort, and the extreme dependence on the mixing ratio and the pressure inside the cell, this comparatively small increase in signal was deemed to be too low for this method to be practical for everyday studies.

2.4 Velocity Map Imaging

Velocity map imaging is a method used for studying the photodissociation dynamics by identifying the total kinetic energy release of a dissociation process and the angular dependence of it.^{40,41} It can be utilized in connection with a TOF MS setup (Figure 2.6). Upon photodissociation of a molecule inside the ionization region, the fragments receive a fraction of the excess energy of the dissociation process as kinetic energy. These fragments are ionized by the ionization laser and get accelerated by the electric field, generated by the ion optics, towards the detector. On the way towards the detector, the Newton sphere expands. The impact location on the detector depends on the velocity vector \vec{v} from the momentum received during dissociation, and the flight time t_{TOF} (Equation 2.2). Only the velocity components in the plane of the detector (x-y plane) influence the position of the impact. All fragments with different velocities perpendicular (z-axis) to the detector but the same velocity in the detector plane get summed up. The impact location R_{xy} corresponds to a velocity of the fragment in the detector plane v_{xy} :

$$R_{xy} = v_{xy} \cdot t_{TOF} = v_{xy} \cdot \frac{d}{\sqrt{2eU}} \cdot \sqrt{\frac{m}{z}} \quad (2.5)$$

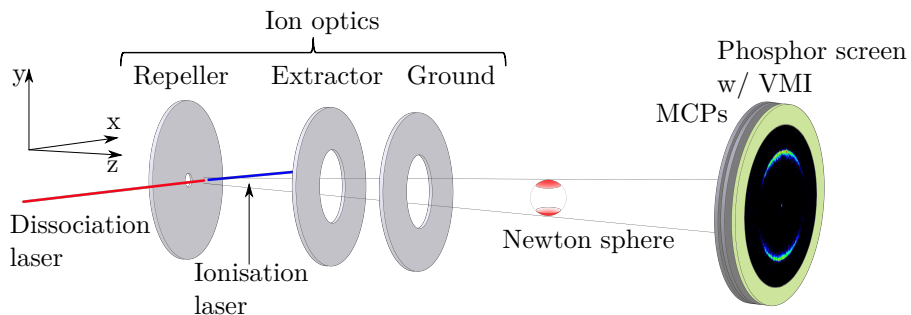


Figure 2.6: Schematic of the main components of a VMI setup. Molecules get dissociated and then ionized between the repeller and the extractor. Afterwards the fragments get accelerated towards a detector consisting of two MCPs and a phosphor screen. On the way towards the detector the Newton sphere expands. A typical projection of the Newton sphere on the phosphor screen is shown.

A phosphor screen is placed behind the MCPs, which are used for TOF MS and a positive voltage is applied to it. Upon impact of a molecule or an atom on the MCPs and the generation of the electron cascade, these electrons are attracted to the phosphor screen, exciting the regions around the impact location. Subsequently, the phosphor screen emits light from these regions and the glowing phosphor screen is photographed with a camera. A velocity map image is the recorded 2D projection of the Newton sphere with the help of the detector. Generally, only a few molecules per laser shot are dissociated and subsequently ionized, resulting in only a handful of spots to be visible on the phosphor screen at a time. Therefore, averaging over considerable time frames is required to achieve an image with sufficiently strong signal to noise ratio.

The 2D projection can be reconstructed allowing for the recovery of the 3D Newton sphere. However, since the image is only a 2D representation of the actual 3D Newton sphere, a reconstruction would not be unique, since many 3D distributions could lead to the same 2D image. If however the data leading to the images has a symmetry axis, this additional information can be utilized in order to receive an unique reconstruction. In practice, this is achieved by creating a cylinder symmetry in the image by having the dissociation laser be polarized parallel to the detector plane resulting in this axis being the symmetry axis. This velocity distribution can then be converted into an energy distribution using Equation 2.5. Since now the 3D Newton sphere has been reconstructed, the information limitation on the x-y plane has been removed:

$$E_T = \frac{zeU}{d^2} \cdot R^2 \quad (2.6)$$

Note that the kinetic energy is independent of the mass of charged particle hitting the detector. The real kinetic energy is usually slightly different from the calculated value because of inhomogeneous regions in the electric field. Information on the kinetic energy imparted to the fragments during a photodissociation event can be gained.

Since the image was recorded with a camera, the resulting kinetic energy distribution has to be converted from pixel position to energy. Using a known substance with a narrow energy distribution upon photodissociation (e.g. diatomic molecules) a calibration factor A can be obtained that allows for the conversion of the pixel position into an energy value:

$$E_T = A \cdot R^2 \quad (2.7)$$

This method for recording the kinetic energy distribution of a photofragment was first demonstrated by A. Eppink and D. Parker.⁴¹ Initially, they used the ion optic layout of W. Wiley and I. McLaren.²³ By adjusting the voltages applied to the stainless steel plates, they reduced the resolution of possible mass spectrum measurements, but in turn found that high resolution images are obtainable. If the voltages are adjusted correctly, no matter where the ions are generated inside the ionization region, all fragments with the same velocity vector \vec{v} impact at the same position on the detector. Several factors contribute to a reduced resolution in VMI experiments. The previously mentioned inhomogeneous electric fields are one contribution to the reduction of resolution. Another factor is the generation of too many ions the same time. These ions will repel each other leading to a blurring of the image. This is called the space charge effect. Since the velocity of light atoms accelerated in this manner is higher than that of heavier atoms, they are especially susceptible to be influenced by space charge effects.⁴²

When ionizing atomic fragments like chlorine via a REMPI process the Doppler effect has to be taken into account.⁵ Atoms generated in a photodissociation reaction receive kinetic energy in random directions. Some atoms will fly towards the ionization laser beam, others will fly away from it. Because of the Doppler effect the fragments perceive a different wavelength depending on the flight direction. This broadens the REMPI line. If the ionization wavelength is set to the middle of the REMPI line, only atoms with little kinetic energy along or against the laser propagation direction will be ionized. This would result in only the central stripe (y - z plane) being recorded. Because of this effect, before recording VMIs of atomic fragments, the width of the REMPI line has to be determined. While recording the VMI, the laser wavelength has to be scanned over the entire REMPI line in order to record the full Newton sphere.

2.4.1 Experimental Details of the Velocity Map Imaging Setup

For this work, the VMI setup was calibrated by using molecular chlorine Cl_2 as a calibrant. Since a photodissociation of Cl_2 results in the generation of two Cl atoms, the fragments cannot have rotational or vibrational energy. The only internal energy possible is the spin-orbit excitation of a chlorine atom. Since chlorine gets ionized via a REMPI process, the ground state chlorine and the spin-orbit excited chlorine can be studied individually. Because the fragments cannot possess any internal energy, the images are not broadened due to a distribution of internal energy. This means that the entire excess energy flows into the translation of the two chlorine atoms with only a potentially small amount used up for the spin-orbit excitation, which can be imaged separately. Because of momentum conservation, the two chlorine atoms have to have exactly the same amount of kinetic energy, resulting in an extremely narrow line to be visible in the reconstructed kinetic energy distribution. The expected energy of this peak can be easily calculated in dependence of the used dissociation wavelength by using the BDE.⁴³ Comparing the distance from the image center in pixel and the calculated energy leads to the calibration factor. By adjusting the voltages ratio between repeller and extractor while minimizing the line width of the chlorine signal, the resolution of the setup can be optimized. For the current setup the maximum resolution can be achieved at a ratio of 1.438 between repeller and extractor. In general, voltages of 5000 V and 3478 V for repeller and extractor were used respectively. The calibration factor A was determined to be $1.6 \cdot 10^{-5}$ at these voltages. 5000 V is the maximum allowed voltage that can be applied to the repeller. Lowering the voltages while keeping the ratio reduces the acceleration which in turn increases the flight time. This results in the Newton sphere to have more time to expand. This allows for the recording of higher resolution images but since the Newton sphere is larger, the maximum recordable energy is decreased.

A phosphor screen doped with $\text{Gd}_2\text{O}_2\text{S:Tb}$ is used, that emits light at 545 nm. This material glows for about 1 to 1.5 ms after excitation. However, typical time frames between different masses recorded in the TOF MS are on the scale of a few hundred nanoseconds to a few seconds. This presents a challenge for the imaging process, since the phosphor screen will glow because of the impacts of multiple species, overlapping the signals in the recorded image. In this experimental setup, a push-pull-transistor switch is used in order to rapidly alternate the applied voltage to the MCPs. A delay generator is used in order to apply the ~ 1.8 kV to the MCP when the fragment being investigated hits the detector, and a voltage of about $2/3$ (~ 1.2 kV) of this value for the rest of the time. The switch allows for the high voltage duration to be as low as 100 ns. This results in only the fragments hitting the detector within this time frame to create an electron cascade strong enough to result in the glowing of the phosphor screen. The voltage outside of this window is not decreased

entirely to 0 V in order to preserve the MCPs. The glow on the phosphor screen is recorded with a monochrome progressive scan CCD camera (PRO-SILICA GC1380H von Allied Vision Tec.) through a window in the apparatus. It has a resolution of 1360 px x 1024 px. A lens is attached to the camera, focusing the light on the CCD chip and resulting in a maximum resolution of 800 px x 800 px for the recorded images.

The output of both dye lasers is polarized horizontally. If the light enters the vacuum chamber it would be polarized perpendicular to the detector plane. In order to achieve the parallel polarization necessary for the cylindrical symmetry, the polarization is turned by 90° by a double-Fresnel rhomb. It consists of two optical prisms shaped in the form of parallel epipeds glued together by optical cement. When the input angle is adjusted correctly, this Fresnel-rhomb turns the polarization by exactly 90°.

2.4.2 Image Reconstruction

When recording velocity map images, multiple steps have to be taken in order to reconstruct the 3D Newton sphere and get the kinetic energy distribution of the fragments. The procedure is shown in Figure 2.7. Under the premise that two separate lasers are used for dissociation and ionization, the individual contributions of both lasers needs to be subtracted from the actual image. This is because either laser may produce an ion of the species being examined by itself and it would result in a signal contribution that is not related to the photodissociation which is being examined. This is especially important for experiments involving radicals. When using pyrolysis or other methods for generating a radical, other molecules besides the desired radical get generated. In some cases the product of the photodissociation being examined also gets generated during the production of the radical. Since it does not receive any translational energy from a photodissociation process, these fragments fly in a straight line resulting in a signal in the center of the detector even without the dissociation laser being switched on. The advantage of subtracting background signals is also, that signals caused by dead pixels will also be removed.

The reconstruction of the Newton sphere requires a symmetrical image. However, several factors contribute to the raw image not being perfectly symmetrical, requiring a symmetrization of the image before further analysis can be conducted. One reason for these asymmetries is an inhomogeneous acceleration field for the ions. Furthermore, the area where the electrical contact to the MCP takes place has a slightly different intensity distribution than the rest of the image. These kinds of effects can be removed by a simple symmetrization of the raw image.

Once these corrections of the raw image have been done, the 3D Newton sphere can be reconstructed from the image. Multiple different methods have been

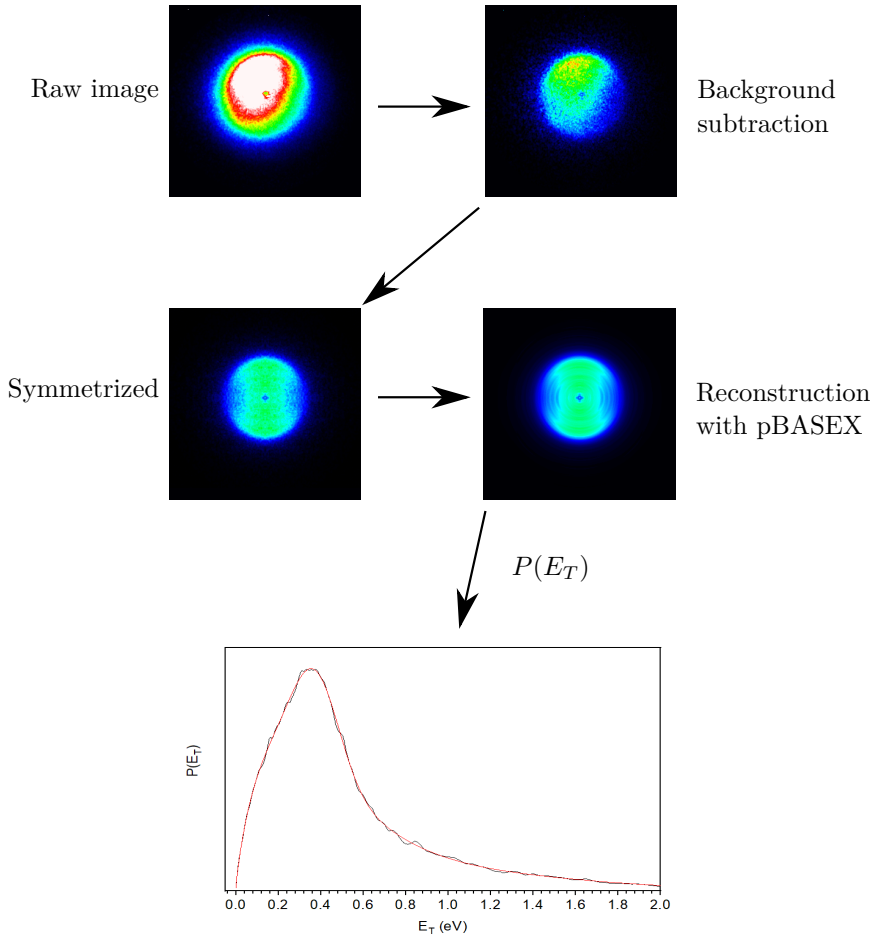


Figure 2.7: Steps required to analyze a velocity map image. First the background signal is subtracted from the raw image. Then this image is symmetrized. From the resulting image the 3D Newton sphere is reconstructed with the pBASEX algorithm. Finally the translational energy distribution can be extracted.

developed for this purpose. The methods can be divided into three different approaches:⁴⁰

- Inversion methods
- Forward convolution methods
- Maximum entropy method

The inversion methods involve a calculation of the 3D distribution on the basis of the 2D image. On the other hand, forward convolution methods try to approximate the 2D image by simulating various 3D distributions and optimizing them in order to achieve an agreement as good as possible between calculated and actual 2D image. Similarly to the forward convolution methods, the maximum entropy method also approximates and optimizes the 3D Newton sphere. The basis for this optimization is the maximization of the Bayesian probability function.

2.4.2.1 Inverse Abel-Transform

I used the pBASEX method which is an inversion type method based on the inverse Abel transform. The original Abel transform was invented in the 19. century by Norwegian mathematician N. H. Abel.⁴⁴ It is based on the fact that a 2D representation of a 3D distribution can be described by:^{40,45}

$$P(x, y) = \int_{-\infty}^{+\infty} I(x, y, z) dz \quad (2.8)$$

Here, the plane spanned by the x- and y-axis is the plane on which the 3D photofragment distribution gets projected on. This means the molecules travel along the z-axis towards the detector. Also, the cylindrical symmetry axis is assumed to be parallel to the y-axis. Since the image is recorded with a CCD chip, this integral can be rewritten for each row i on the chip with $s_i(x, y) = I(x, y_i, z)$. It is a slice of the 3D Newton sphere in the x-z plane. Because of the cylindrical symmetry the integral can be simplified to:

$$\begin{aligned} f(x, y_i) &= \int_{-\infty}^{+\infty} s_i(x, z) dz \\ &= 2 \int_0^{+\infty} s_i(x, z) dz \end{aligned} \quad (2.9)$$

Now, the Cartesian coordinate system gets converted into a cylindrical coordinate system with $\sqrt{x^2 + z^2} = r$. The angular dependency can be neglected because of the cylindrical symmetry:

$$f(x, y_i) = 2 \int_x^{+\infty} \frac{s_i(r) r}{\sqrt{r^2 - x^2}} dr \quad (2.10)$$

Applying the Fourier transform convolution theorem on this equation, it is possible to reconstruct the 3D sphere that leads to a certain distribution, one row at a time:⁴⁶

$$s_i(r) = \frac{1}{\pi} \int_r^{+\infty} \frac{\frac{d}{dx} f(x, y_i)}{\sqrt{x^2 - r^2}} dx \quad (2.11)$$

However, this method has various drawbacks, one problem being that there is a singularity at the position $x = r$. Another issue is the derivative inside the integral which results in an amplification of the noise inside the recorded image.⁴⁰

2.4.2.2 Basis Set Expansion and Polar Basis Set Expansion

The basis set expansion (BASEX) method is a further development of the standard inverse Abel transform and was developed in order to solve the shortcomings of the Abel transform.⁴⁷ It is based on the idea that the 3D distribution can be approximated with a basis $f_k(r, y)$ of the size K :

$$I(r, y) = \sum_{k=0}^{K-1} C_k \cdot f_k(r, y) \quad (2.12)$$

C_k are the coefficients of the individual basis functions. Inserting this expression into Equation 2.8, converted into cylindrical coordinates, results in following equation:

$$P(x, y) = \sum_{k=0}^{K-1} C_k \cdot 2 \int_x^{+\infty} \frac{f_k(r, y) r}{\sqrt{r^2 - x^2}} dr \quad (2.13)$$

By defining

$$g_k = 2 \int_x^{+\infty} \frac{f_k(r, y) r}{\sqrt{r^2 - x^2}} dr \quad (2.14)$$

this equation can be simplified to:

$$P(x, y) = \sum_{k=0}^{K-1} C_k \cdot g_k \quad (2.15)$$

The goal is now to solve this equation by calculating the C_k . This method is better suited of reconstructing data with a poor signal to noise ratio. But on the other hand it results in this noise added to one stripe in the center of the symmetry axis making the analysis of the reconstructed Newton sphere more ambiguous.

By switching from cylindrical to spherical coordinates, the method can be improved once more and is called polar basis set expansion (pBASEX).⁴⁸ Now

the 3D distribution is described by $I(R, \theta)$. θ is the angle between the y-axis (laser polarization axis) and the position of the point in the x-y plane. A basis $f_{kl}(R, \theta)$ is chosen, that can be split into a radial contribution and an angular contribution. Typically Gaussian distributions with the width σ and the center R_k are used for the radial contribution. Since the anisotropy of the Newton sphere can be described with Legendre polynomials ($P_l(\theta)$; see subsection 1.1.1), they are usually selected for the angular component:

$$f_{kl} = e^{-\frac{(R-R_k)^2}{\sigma}} P_l(\theta) \quad (2.16)$$

$$I(R, \theta) = \sum_{k=0}^{K-1} \sum_{l=0}^{L-1} C_{km} \cdot f_{kl}(R, \theta) \quad (2.17)$$

When using the pBASEX method with its a spherical coordinate system, the noise gets concentrated in the center point of the coordinate system, making a qualitatively good analysis of the data possible. Furthermore, since only a limited amount of Legendre polynomials (mostly only to the second order) are required to describe the angular distribution of the fragments, this method is not really compute-intensive making the reconstruction be completed quickly. Including a few more higher order polynomials can however smooth the reconstruction slightly making it easier to interpret the results. Additionally, the anisotropy parameters β_l are included in the coefficients C_{kl} , allowing quick access to them.

2.4.3 Data Analysis

Once the 3D Newton sphere has been reconstructed, the corresponding kinetic energy distribution $P(E_T)$ can be extracted from it. A typical $P(E_T)$ is shown in Figure 2.8. Several values can be extracted from the $P(E_T)$ leading to a better understanding of the dissociation dynamics. This includes the average kinetic energy $\langle E_T \rangle$, the fraction of excess energy that went to the kinetic energy of the fragments $\langle f_T \rangle$, and the anisotropy parameter β .

In order to get the average kinetic energy, the experimental data first is fitted. The fit used depends on the kind of dissociation observed. Because of the impulsive nature of such dissociations, direct dissociations usually have high average kinetic energy. They can usually be fitted best with a Gaussian distribution.

Statistical dissociation distributions can be fitted in two ways. The first involves calculating the shape of the distribution with the following equation:⁴⁹

$$P(E_T) = C \cdot E_T^n \rho_{rovib}(E_T^{max} - E_T) \quad (2.18)$$

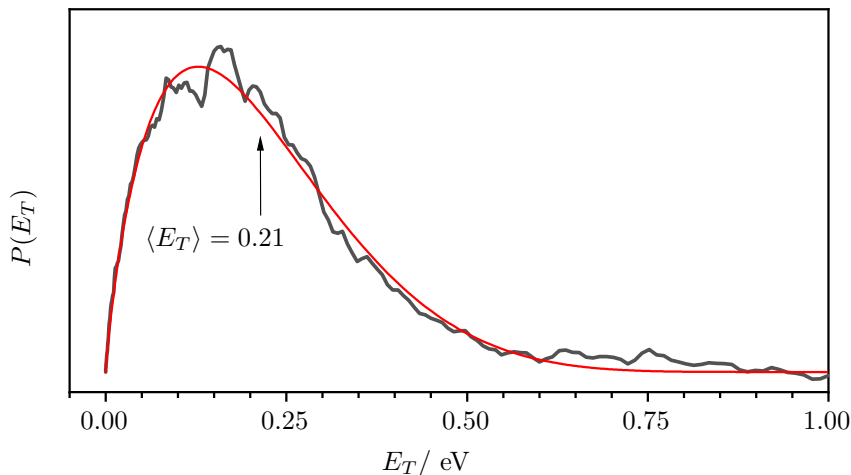


Figure 2.8: Typical kinetic energy distribution fitted with a two-parameter fit. Its average energy is 0.21 eV.

This requires the knowledge of the rovibrational density of states of the product ρ_{rovib} . C is a normalization constant and E_T^{max} is the theoretically calculated maximum energy the fragment can have (see Equation 1.5). In most cases, ρ_{rovib} can be approximated by the vibrational density of states ρ_{vib} , if high excess energies are present. In these cases the rotational energy is comparatively small because of angular momentum conservation. Here, n is the fitting parameter. If n is 0.5 it is called an ideal prior distribution, where the excess energy is distributed equally over all degrees of freedom inside the molecule.⁵⁰ But as long as it is between 0 and 3, the dissociation can be regarded as being statistical in nature.⁴⁹

If the dissociation pathway cannot be described by either a direct or a statistical pathway, if the density of states is not known, if the pathway that leads to the observed fragment cannot be identified precisely, or if multiple pathways are observed in the same distribution, only an empirical model can be used to fit the data:^{51–54}

$$P(E_T) = C \cdot E_T^a (E_T^{max} - E_T)^b \quad (2.19)$$

The structure of this empirical fit is very similar to Equation 2.18. It is called a two-parameter fit because of the two fitting parameter, a and b . The density of states is simply replaced with the term $(E_T^{max} - E_T)^b$. This term can often approximate the density of states if a statistical process is present. Equation 2.19

can fit practically any energy distribution, even direct dissociations. If the maximum kinetic energy E_T^{max} for the process is unknown, it can be replaced by an arbitrary number that is in the region where the energy distribution has already reached 0.

Using the average kinetic energies extracted from the fits and the calculated maximum kinetic energies, the fraction of energy going into the translation of the fragments can be calculated as:

$$\langle f_T \rangle = \frac{\langle E_T \rangle}{E_T^{max}} \quad (2.20)$$

Typical values for $\langle f_T \rangle$ for direct dissociations are around 50%.⁵⁵ For statistical processes on the other hand, a lot of the excess energy gets distributed inside the fragments before dissociation. This leads to a high fraction of excess energy to go into vibrational excitation of the fragments. Typically, statistical dissociation pathways have an average kinetic energy 10 to 25% of the excess energy. For the statistical dissociation of aromatic hydrocarbons $\langle f_T \rangle$ is around 10%.^{56,57} This average energy is a little higher for hydrocarbon radicals with a value of around 20%.⁵⁷⁻⁵⁹

The kinetic energy for a direct dissociation can be approximated with a simple impulsive model, described by Tuck⁶⁰ and by Galloway et al.⁶¹ The model describes a direct dissociation in the following way: Upon excitation and consequent bond cleavage, all excess energy first flows into the translational energy of the two atoms between which the bond is getting cleaved. Only then the excess energy gets redistributed inside the fragments. The average translational energy $\langle f_T \rangle$ can be computed as the quotient of the reduced mass of the atoms between which the bond is split μ_a and the reduced mass of the fragments μ_f :

$$\langle f_T \rangle = \frac{\mu_a}{\mu_f} \quad (2.21)$$

The anisotropy parameter β can be extracted from the experimental data in two ways. The first way is by integrating the angle dependent $P(E_T, \theta)$ between the energy values of interest. The result can then be fitted with Equation 1.6 which gives the β -value. The second way involves utilization of data gained from the reconstruction of the image via a program written by L. Poisson and G. Garcia (see subsection 2.4.4). Besides the total integrated intensity of the signal in dependence of the radius, it also gives the weight of the P_2 contribution, which is equal to the β -value times a scaling factor. By dividing this weight by the total intensity, the β -value can be gotten. This second method also has the advantage that some information can still be gained if multiple pathways overlap. If, for example, an isotropic and an anisotropic contribution overlap partially but can be disentangled, the quotient of the P_2 contribution divided by the anisotropic contribution can give a lower boundary value the β -value.

Similar analysis is not easily possible with the first method. As described in subsection 1.1.1, direct photodissociations usually show an anisotropy while indirect dissociations have none.

2.4.4 Data Acquisition

All TOF MS measurements were carried out using LabView programs that were developed by Michael Schneider. Since the previously used Teledyne LeCroy oscilloscope has been replaced by an oscilloscope from Rhode & Schwarz, the communication part had to be rewritten.

Individual mass spectra were recorded with the `TOFtoolNeu.vi`. The oscilloscope is set to display and save 32 averaged laser shots. Usually, five of those saved samples are averaged again to produce one mass spectrum, resulting in a final mass spectrum to consist of 160 averaged laser shots. In order to calibrate the mass spectrum two time-of-flight points need to be selected and assigned to known masses.

Wavelength dependent mass spectra were recorded with the Labview program `DyeScanHMO.vi`, which also controlled the wavelength of the dye laser for these measurements. The interval between start and stop wavelength was usually set to 0.1 cm^{-1} for REMPI line scans.

The time delay between the photodissociation and the ionization laser was adjusted with the help of the `Delay-scan_1.0.vi` program. With this program mass spectra at different delays between the lasers were recorded. This data can be used to identify the time delay when the two lasers reach the ionization region at the same time. Also, this program can be used for scanning the ionization laser timing with respect to the molecular beam timing. This is used to adjust the time when and with this the position of where the molecular beam gets hit by the laser.

Both, the wavelength and the time delay scans, can be analyzed with the `integrate spectra 4.0.vi` program.

`VMI_Einzelbild.vi` was used to record the images. A continuous mode in which n single images from one laser pulse get summed to a resulting image can be selected. Once n images are recorded, the image is deleted and it starts over from the beginning again. This mode is used when checking the signal before recording the VMI. Once the preparations are completed, the continuous mode can be switched to a recording mode where the image will be saved. The experimental parameters were documented in a separate file. The amount of individual images n used for generating a VMI was usually between 5000 and 10000. Because of shifts in laser power over time, longer measurements are not advisable. This VMI recording program also offers the feature to remove signals from the individual images that fall below a set value (thresholding).

This is important because each individual image contains the noise of the CCD chip. A value of 4 was chosen for the threshold.

The program `1-png.binär.tab add sub.vi` was used to subtract the single laser background signals from the actual velocity map image. Since this results in the signal from dead pixels to be subtracted twice, one image without any lasers on has to be added to the VMI at the end in order to completely remove the influence of these dead pixels.

Symmetrization and analysis of the VMI images were done with a program written by L. Poisson and G. Garcia. First residual bad pixels that could not completely be subtracted previously are removed. Afterwards, the images are symmetrized. Finally the Newton sphere gets reconstructed with the pBASESX algorithm. Depending on the dissociation process the Legendre polynomials P_0 , and P_2 or the polynomials P_0 , P_2 , and P_4 were used.

2.5 Optimizing Experimental Parameters

Before VMIs can be recorded, the optimal experimental parameters have to be determined. These parameters include:

- Pyrolysis power
- Backing pressure
- Molecular beam width and delay
- Time delay between dissociation laser and ionization laser
- REMPI lines

The pyrolysis power has a large influence on the products generated. If the pyrolysis power is too low, insufficient amount of radical will be generated. Also the amount of precursor will not have been depleted by a lot, which may lead to the photolysis of this precursor to generate a significant background signal. On the other hand, if the power is too high, the pyrolysis process will become arbitrary, resulting in various radicals to be generated. Depending on the precursor, these radicals might also have a photodissociation pathway leading to the product that gets generated in the pathway that is to be studied. This leads to an overlap of signals in the $P(E_T)$ and makes the analysis more challenging or outright impossible. Furthermore, when the pyrolysis power is high and lots of radicals get generated, recombination products are formed at an increased rate. This can also lead to unwanted background signals. These reasons make finding a precursor that dissociates selectively at a not too high pyrolysis power utmost important.

Figure 2.9 shows a comparison of three mass spectra at different pyrolysis power settings used for the pyrolysis of CHCl_3 (30 W, 40 W and 50 W). At low pyrolysis powers mainly CCl_2 and small amounts of CCl and CHCl are

produced. At higher pyrolysis powers, signals like CCl_3 , CHCl_2 , and recombination products like C_2Cl and C_2Cl_2 become relevant. When examining the photodissociation of CCl_2 , a power between 30 and 40 W would be ideal. At 30 W the CCl_2 signal is still weak, leading to a poor signal to noise ratio in the VMI. The signal increases significantly at 40 W but other fragments start to get observable. Because at pyrolysis power levels of around 30 W CCl_2 is the dominant product and no other relevant species can decay to CCl , CHCl_3 is a suitable precursor for studying the photodissociation of CCl_2 .

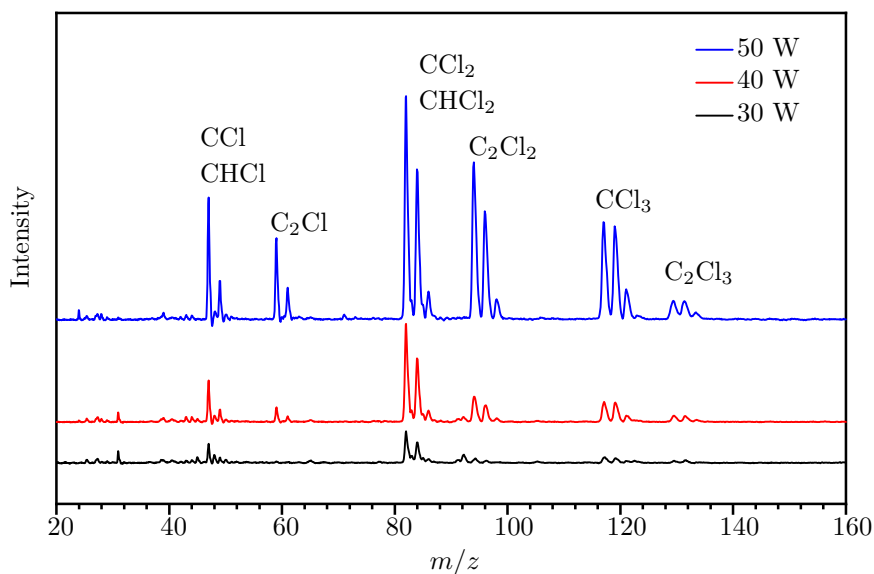


Figure 2.9: Example for the dependence of radical generation with pyrolysis. CHCl_3 is pyrolyzed with 30 W, 40 W, and 50 W. At low powers mainly CCl_2 and some CCl and CHCl are produced. By increasing the pyrolysis power fragments like CCl_3 and CHCl_2 are produced, as well as recombination products like C_2Cl and C_2Cl_2 .

Backing gas and pressure can have an influence on the cooling and the total signal. The backing gas can also form clusters with the molecule being investigated. That is why performing a few test measurements with different backing gases and varying their pressure is required. The difference in cooling potential between He and Ar is demonstrated in Figure 2.10 with a CCl image resulting from the dissociation from CCl_2 at 230 nm (precursor: CHCl_3). Helium shows a noticeable longer higher energy tail because of the reduced cooling potential compared to the signal recorded with argon.

The opening width of pulse valve generating the molecular beam also has to be optimized. The further the pulse valve gets opened, the stronger the signal

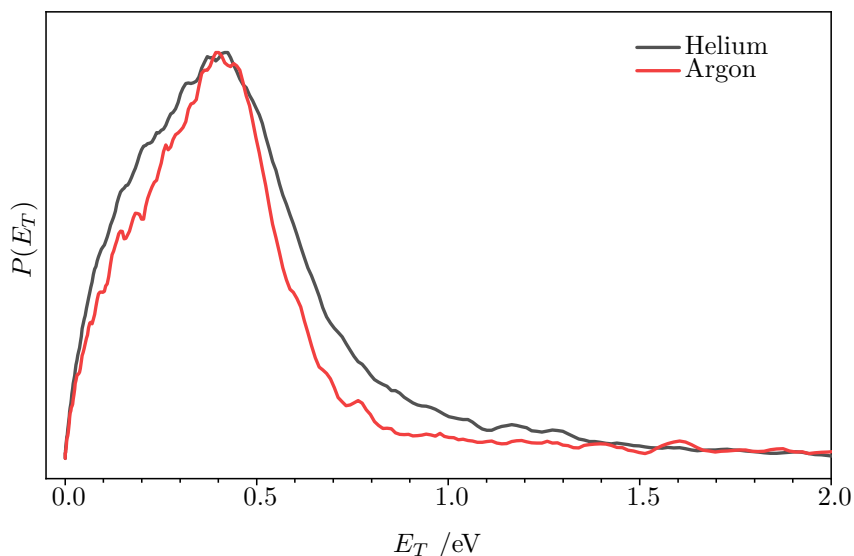


Figure 2.10: Comparison of the $P(E_T)$ of CCl generated from the photodissociation of CCl_2 (precursor CHCl_3). The helium trace is visibly broader which is a result of the increased residual internal energy of the radicals before being photodissociated.

that can be observed becomes, improving the signal to noise ratio. However, if it is opened too far, the returning force exerted by the springs in the valve can result in a oscillation of the magnetic body that is responsible for opening and closing the nozzle, which has a negative influence on the signal. The onset of this oscillation depends on how the valve was sealed, and the backing gas and pressure applied. Therefore, regular checks of the TOF in dependence of the molecular beam position have to be performed. Also, images should be recorded at the rising edge of the molecular beam since this is the coldest part of the beam, resulting in the best VMIs.

Scans of the time delay between dissociation and ionization laser have to be carried out in order to find the optimal timing for recording the image. This scan also gives information on the type of dissociation taking place. If the ionization laser comes immediately after the dissociation laser, an increase in the fragment signals should be observed. If this rise time is on the same time scale as the resolution of the lasers (~ 10 ns) only this upper limit of 10 ns can be given. If it is longer, the rate constant for the dissociation can be determined from the rise time.

The last factor that has to be repeatedly verified is the position of a REMPI line when ionizing a species via a REMPI scheme. When examining a sample for

the first time, this REMPI line needs to be found. But even if the REMPI line is already known and recorded, the REMPI line shifts slightly over the course of a week, and sometimes even over the course of a day because of thermal effects inside the lasers. This has an especially profound effect when examining atomic fragments since their REMPI lines are only a few cm^{-1} broad. If the REMPI line shifts, it would result in only a part of Doppler profile to be scanned when performing VMI experiments. This would lead to only a part of the entire Newton sphere to be recorded.

2.6 Bibliography

- (1) Nonhebel, D. C.; Walton, J. C., *Free-radical chemistry; structure and mechanism*; University Press: 1974, p 572.
- (2) Kantrowitz, A.; Grey, J. *Rev. Sci. Instrum.* **1951**, *22*, 328.
- (3) Kistiakowsky, G. B.; Slichter, W. P. *Rev. Sci. Instrum.* **1951**, *22*, 333.
- (4) Smalley, R. E.; Wharton, L.; Levy, D. H. *Acc. Chem. Res.* **1977**, *10*, 139–145.
- (5) Albert, S.; Albert, K. K.; Hollenstein, H.; Tanner, C. M.; Quack, M., *Handbook of High-resolution Spectroscopy*; John Wiley & Sons, Ltd: 2011.
- (6) Demtröder, W., *Laserspektroskopie: Grundlagen und Techniken*; Springer-Verlag Berlin Heidelberg: 2007.
- (7) Giegerich, J. Photofragment-Imaging des Ethylradikals, 2012.
- (8) Kohn, D. W.; Clauberg, H.; Chen, P. *Rev. Sci. Instrum.* **1992**, *63*, 4003.
- (9) Wentrup, C. *Angew. Chem., Int. Ed.* **2017**, *56*, 14808–14835.
- (10) Minsek, D. W.; Blush, J. A.; Chen, P. *J. Phys. Chem.* **1992**, *96*, 2025–2027.
- (11) Fischer, I.; Pratt, S. T. *Phys. Chem. Chem. Phys.* **2022**, *24*, 1944–1959.
- (12) Heaven, M.; Miller, T. A.; Bondybey, V. E. *Chem. Phys. Lett.* **1981**, *84*, 1–5.
- (13) Osborn, D. L.; Zou, P.; Johnsen, H.; Hayden, C. C.; Taatjes, C. A.; Knyazev, V. D.; North, S. W.; Peterka, D. S.; Ahmed, M.; Leone, S. R. *Rev. Sci. Instrum.* **2008**, *79*, 104103.
- (14) Garcia, G. A.; Krüger, J.; Gans, B.; Falvo, C.; Coudert, L. H.; Loison, J. C. *J. Chem. Phys.* **2017**, *147*, 013908.
- (15) Monks, P. S.; Stief, L. J.; Krauss, M.; Kuo, S. C.; Zhang, Z.; Klemm, R. B. *J. Phys. Chem.* **1994**, *98*, 10017–10022.
- (16) Dulcey, C. S.; Hudgens, J. W. *J. Phys. Chem.* **1983**, *87*, 2296–2298.
- (17) Schlachta, R.; Lask, G.; Tsay, S. H.; Bondybey, V. E. *Chem. Phys.* **1991**, *155*, 267–274.
- (18) Engelking, P. C. *Rev. Sci. Instrum.* **1998**, *57*, 2274.
- (19) Morley, G. P.; Felder, P.; Huber, J. R. *Chem. Phys. Lett.* **1994**, *219*, 195–199.
- (20) Shin, S. K.; Dagdigian, P. J. *Phys. Chem. Chem. Phys.* **2006**, *8*, 3446–3452.
- (21) Campana, J. E. *Instrum. Sci. Technol.* **2008**, *16*, 1–14.
- (22) Glish, G. L.; Vachet, R. W. *Nat. Rev. Drug Discov.* **2003**, *2*, 140–150.

-
- (23) Wiley, W. C.; McLaren, I. H. *Rev. Sci. Instrum.* **1955**, *26*, 1150.
- (24) Wiza, J. L. *Nucl. Instrum. Methods* **1979**, *162*, 587–601.
- (25) Und Plasmatechnik GmbH, S. L., *Sirah Pulsed Dye Laser Service Manual Cobra*, 2002.
- (26) Und Plasmatechnik GmbH, S. L., *Sirah Pulsed Dye Laser Service Manual PrecisionScan*, 2002.
- (27) Alcaraz, C.; Fischer, I.; Schröder, D., *Encyclopedia of Radicals in Chemistry, Biology and Materials*; Studer, A., Ed.; John Wiley & Sons, Ltd: 2012.
- (28) Matthaehi, C. T.; Mukhopadhyay, D. P.; Röder, A.; Poisson, L.; Fischer, I. *Phys. Chem. Chem. Phys.* **2022**, *24*, 928–940.
- (29) Janda, M.; Hensel, K.; Tóth, P.; Hassan, M. E.; Machala, Z. *Appl. Sci.* **2021**, *11*, 7053.
- (30) Demtröder, W., *Laserspektroskopie 2*, 6th ed; Springer Spektrum: 2013.
- (31) Hurst, G. S.; Payne, M. G.; Kramer, S. D.; Young, J. P. *Rev. Mod. Phys.* **1979**, *51*, 767.
- (32) Streibel, T.; Zimmermann, R. *Annu. Rev. Anal. Chem.* **2014**, *7*, 361–381.
- (33) Sansonetti, J. E.; Martin, W. C. *J. Phys. Chem. Ref. Data* **2005**, *34*, 1559.
- (34) Reid, M.; Green, V.; Koehler, S. P. *Phys. Chem. Chem. Phys.* **2014**, *16*, 6068–6074.
- (35) Radziemski, L. J.; Kaufman, V. *J. Opt. Soc. Am.* **1969**, *59*, 424–443.
- (36) *Applied Laser Spectroscopy*; Demtröder, W., Inguscio, M., Eds.; Springer US: 1990.
- (37) Ganeev, R. A.; Usmanov, T. *J. Opt. A-Pure Appl. Op.* **2000**, *2*, 550.
- (38) Cantu, A. M.; Parkinson, W. H.; Grisendi, T.; Tagliaferri, G. *Phys. Scr.* **1985**, *31*, 579.
- (39) Cantu, A. M.; Parkinson, W. H. *Phys. Scr.* **1988**, *37*, 336.
- (40) *Imaging in Molecular Dynamics: Technology and Applications*; Whitaker, B. J., Ed.; Cambridge University Press: 2003.
- (41) Eppink, A. T.; Parker, D. H. *Rev. Sci. Instrum.* **1998**, *68*, 3477.
- (42) Ashfold, M. N.; Nahler, N. H.; Orr-Ewing, A. J.; Vieuxmaire, O. P.; Toomes, R. L.; Kitsopoulos, T. N.; Garcia, I. A.; Chestakov, D. A.; Wu, S. M.; Parker, D. H. *Phys. Chem. Chem. Phys.* **2006**, *8*, 26–53.
- (43) Barrow, R. F.; Long, D. A.; Millen, D. J.; Roy, R. J. L., *Energy levels of a diatomic near dissociation*; The Chemical Society: 1973, pp 113–176.

- (44) Abel, N. *J. für die Reine und Angew. Math.* **1826**, *1*, 153–157.
- (45) Heck, A. J.; Chandler, D. W. *Annu. Rev. Phys. Chem.* **1995**, *46*, 335–372.
- (46) Vicharelli, P. A.; Lapatovich, W. P. *Appl. Phys. Lett.* **1998**, *50*, 557.
- (47) Dribinski, V.; Ossadtchi, A.; Mandelshtam, V. A.; Reisler, H. *Rev. Sci. Instrum.* **2002**, *73*, 2634.
- (48) Garcia, G. A.; Nahon, L.; Powis, I. *Rev. Sci. Instrum.* **2004**, *75*, 4989.
- (49) Quack, M. *Chem. Phys.* **1980**, *51*, 353–367.
- (50) Knsrsey, J. L. *J. Chem. Phys.* **2003**, *54*, 1206.
- (51) Muckerman, J. T. *J. Phys. Chem.* **1989**, *93*, 179–184.
- (52) North, S. W.; Marr, A. J.; Furlan, A.; Hall, G. E. *J. Phys. Chem.* **1997**, *101*, 9224–9232.
- (53) Deyerl, H. J.; Fischer, I.; Chen, P. *J. Chem. Phys.* **1999**, *111*, 3441.
- (54) Grubb, M. P.; Warter, M. L.; Johnson, K. M.; North, S. W. *J. Phys. Chem.* **2011**, *115*, 3218–3226.
- (55) Sato, H. *Chem. Rev.* **2001**, *101*, 2687–2725.
- (56) Giegerich, J.; Fischer, I. *Phys. Chem. Chem. Phys.* **2013**, *15*, 13162–13168.
- (57) Tsukiyama, K.; Bersohn, R. *J. Chem. Phys.* **1998**, *86*, 745.
- (58) Ichimura, T.; Mori, Y.; Shinohara, H.; Nishi, N. *J. Chem. Phys.* **1998**, *107*, 835.
- (59) Giegerich, J.; Fischer, I. *J. Chem. Phys.* **2015**, *142*, 044304.
- (60) Tuck, A. F. *J. Chem. Soc., Faraday trans. II* **1977**, *73*, 689–708.
- (61) Galloway, D. B.; Glenewinkel-Meyer, T.; Bartz, J. A.; Huey, L. G.; Crim, F. F. *J. Chem. Phys.* **1998**, *100*, 1946.

3 Photodissociation of Benzoyl Chloride: A Velocity Map Imaging Study Using VUV Detection of Chlorine Atoms

Christian T. Matthaedi, Deb Pratim Mukhopadhyay, and Ingo Fischer

Published: J. Phys. Chem. A, 2021, 125, 14, 2816-2825

DOI: 10.1021/acs.jpca.0c11236

3.1 Abstract

UV photodissociation of benzoyl chloride, Ph-CO-Cl, is associated with the loss of a chlorine atom. Here we excite benzoyl chloride to the S_1 , S_2 , and S_3 excited states at 237, 253, 265, and 279.6 nm and detect the Cl photofragment by $[1 + 1']$ photoionization using 118.9 nm VUV radiation. The translational energy distribution of the Cl atom is measured by velocity map ion imaging. An isotropic image and a unimodal translational energy distribution are observed at all dissociation wavelengths, and a fraction of 18-20% of the excess energy is released into translation. The results indicate a dissociation that predominately proceeds from the vibrationally hot S_0 ground state, although the observed translational energy release deviates significantly from a prior distribution. However, the impulsive model does also not represent the translational energy release. As a Cl/Cl* branching ratio of 9:1 or more is observed in one-color experiments at 235 nm, we conclude that direct dissociation from excited electronic states contributes only to a minor extent.

3.2 Introduction

Volatile organic compounds (VOC) and free radicals containing Cl have been gaining attention since the discovery of their active catalytic role for destroying stratospheric ozone.¹⁻⁴ Upon photodissociation in the atmosphere, one of the major fragmentation channels is C-Cl bond cleavage, followed by the formation of Cl, a highly reactive and oxidative species. Thus, chlorinated compounds can seriously affect both the atmospheric chemical processes and composition.^{1,3-6} For a deeper understanding of their complex chemistry, the mechanistic details and outcome of the initial photodissociation processes need to be investigated.

The C-Cl bond cleavage of alkyl chlorides generally occurs via a direct mechanism from an initially excited repulsive surface with a large release of translational energy.⁷⁻⁹ In particular, CH₃Cl has been studied in great detail using VUV excitation.¹⁰⁻¹⁵ On the other hand, in aryl chlorides, an indirect mechanism from a lower electronic state following internal conversion (IC) often

competes with the direct dissociation.^{8,9,16–18} Moreover, spin-orbit coupling also plays a significant role in the mixing of different electronic states. In α , β -unsaturated alkyl chlorides, multiple C-Cl bond dissociation pathways along with HCl formation are experimentally observed.^{19–24} For acyl chlorides like CH_3COCl , the C-Cl bond cleaves preferentially over the C-C bond with fast dissociation via an exit barrier that results from surface crossing between electronic states, in contrast to the usual intersystem crossing mechanism seen in Norrish type-I reaction of aliphatic aldehydes and ketones.^{25–27} Enones like acryloyl chloride ($\text{CH}_2=\text{CHCOCl}$) show two different Cl fragmentation channels along with HCl formation and CO elimination.^{28–31} In these two channels, the fast Cl with high translational energy results from an electronic predissociation, and the low-energy channel mainly appears from excited vibrational states of S_0 following IC. Fumaryl chloride (Cl-CO-CH=CH-CO-Cl) supposedly also shows a similar behavior.³²

In the current study, we have investigated the photodissociation of benzoyl chloride (Ph-CO-Cl), the simplest aromatic acid chloride, over an energy region that covers three different electronic states by detection of Cl photofragments with VUV radiation in a velocity map imaging (VMI) spectrometer. Benzoyl chloride is mainly used in the dye and pharmaceutical industries. A major application is in the production of benzoyl peroxide, used as initiator in the polymer industry. Benzoyl chloride can be harmful to the environment, because it releases Cl upon photodissociation and its gas phase absorption spectrum extends to UV-B region. Photodissociation of Ph-CO-Cl has been studied by Saha et al., who analyzed the time-of-flight (TOF) profile of Cl ionized by $[2 + 1]$ REMPI after exciting the S_3 state at 235 nm. The translational energy distribution was obtained by forward convolution of the experimental profile. In their one-color experiments, they found two Cl dissociation channels along with HCl formation.³³ The fast channel was assigned to dissociation in the S_1 state, populated via $S_3 \rightarrow S_1$ internal conversion, while the slower one was found to originate from statistical dissociation in the S_0 ground state following IC. As their experimental arrangement was one-color in nature, they were limited to study the dissociation dynamics in the S_3 state. With the current two-color setup, using UV excitation and VUV ionization, we can study this process from all optically accessible states, thus allowing us to get more insight into the photofragmentation process.

Velocity map imaging (VMI) of photofragments is an efficient and versatile technique to study photodissociation as both translational energy and angular distribution of photofragments can be measured simultaneously with mass selectivity.³⁴ Thus, the technique has been widely applied to study photofragmentation as well as reactive scattering, bimolecular reactions and time-resolved chemical dynamics.^{35–39} In general, resonance-enhanced multiphoton ionization (REMPI) is applied for fragment detection, but in recent years, single photon

ionization using VUV has also been used as a universal ionization source in multi mass ion imaging.^{40–45}

In VMI, probing atomic species is more advantageous compared to their molecular cofragment due to the absence of vibrational and rotational degrees of freedom. With only three translational modes, the 2D image of an atomic fragment is easier to interpret though it contains all energy information regarding the parent molecule as well as the counter-fragment. Therefore, Cl becomes the obvious choice to probe by VMI while investigating the dissociation of Cl-containing molecules. The IE of Cl is 12.968 eV and the usual way for ionization is either [2 + 1] or [3 + 1] REMPI using ~ 235 or ~ 355 nm.^{46,47} As initial excitations in both schemes require multiphoton steps, tight focusing of the laser beam is necessary, which leads to unwanted side reactions including secondary dissociation and dissociative photoionization (DPI) and often blurs the actual process. Furthermore, the absorption cross-section of many organic molecules is large at 235 nm, making them more susceptible to multiphoton side reactions. Therefore, an alternative detection scheme is warranted to investigate the photodissociation dynamics of chlorides.

In the present study, we ionize atomic Cl in a [1 + 1'] process via the ${}^2D_{5/2} \leftarrow {}^2P_{3/2}^o$ transition. Since this process involves sequential absorption of single photons, tight focusing is no longer necessary, hence multiphoton side reactions are eliminated. Note that there are two energetically close atomic states present in Cl at around 118.9 nm (${}^2D_{5/2}$, ${}^2D_{3/2}$) which can be excited in a one- or three-photon transition from the ${}^2P_{3/2}^o$ ground state with an intensity ratio of 4:1.⁴⁶

3.3 Methods

The details of the present experimental arrangement have been described elsewhere.^{48,49} Briefly, a Wiley & McLaren type linear time-of-flight mass spectrometer (TOF-MS) was used, operated in either space-focusing or VMI configuration with three velocity-focusing plates (repeller, extractor, ground), separated by 15 mm. The Ph-CO-Cl (99%) was purchased from Sigma-Aldrich and used without further purification. The sample compartment was directly attached to the carrier gas flow just behind the pulsed valve. The sample vapor was mixed in 1.0 atm of He and expanded into vacuum through a pulsed solenoid valve operating at 10 Hz repetition rate. To keep the sample concentration low to avoid cluster formation, the sample temperature was kept at ~ 30 °C though the boiling point is 198 °C. The seeded free jet was further skimmed and entered into the ion optics through a 5 mm hole in the repeller plate. Ions were extracted by an electric field of 1014 V/cm, while 2319 V/cm was used to accelerate the ions toward the detector. When recording mass spectra, slightly different fields were used to achieve the best mass resolution. For all two-color experiments, the unfocused frequency-doubled output (0.5–1.0 mJ/pulse) of a

dye laser (Sirah, Cobra using coumarine 102, 307, or 153) pumped at 355 nm by a Nd:YAG laser was used for dissociation, and the excitation light crossed the molecular beam at 90° between the repeller and extractor plates. The early part of the jet was excited for minimizing the chance of cluster excitation if present. The ionizing light was introduced in a counter-propagating manner with a delay of typically 170-200 ns. A delay generator (SRS, DG535) was used for synchronization between the molecular beam (MB) and the two lasers. In the laboratory frame, the MB, ion flight path, and the detector were along +z direction, while the dissociation and ionizing lasers came from +x and -x direction. By using a Fresnel double rhomb, the polarization of the dissociation laser was set to be vertical (y-direction), parallel to the detector plane (xy), ensuring the cylindrical symmetry of the recorded image.

For [1 + 1'] ionization of Cl, 118.9 nm VUV light is required for the $^2D_{5/2} \leftarrow ^2P_{3/2}^o$ transition. Another dye laser (Sirah, Precision-Scan), using Pyridine 2 dye and pumped with 532 nm, generates UV light between 350 and 360 (8-9 mJ/pulse) nm via second harmonic generation (SHG). This output was used for frequency tripling, and the residual UV light ionized the excited Cl. VUV light can be generated in the 113.5-117.0 and 117.6-119.2 nm ranges in pure Xe via third-harmonic generation (THG).^{50,51} The SHG output was focused by a lens ($f = 200$ mm) into a Xe gas cell through a fitted quartz window, while the frequency tripled VUV output was focused into the ionization region by a rear-mounted MgF_2 ($f = 100$ mm) lens. As the VUV conversion efficiency is generally less than 10^{-4} , absorption of two VUV photons is unlikely.⁵¹ The Xe cell was directly mounted at the vacuum chamber, and the optimum pressure (P_{Xe}) was 2-3 mbar. Note that the VUV output depends on the gas pressure as the phase-matching depends on the number density of the tripling medium.⁴⁰ The shortcoming of this scheme is that the $^2D_{5/2} \leftarrow ^2P_{1/2}^o$ transition of Cl* is outside of the negative dispersive range of Xe; therefore, the spin-orbit excited Cl* state could not be probed by the present arrangement. It is important to mention that Radziemski and Kaufman have listed a Cl* absorption line at about 117.9 nm (84796.59 cm⁻¹) with a calculated intensities more than 2.5 times larger than the intensities of Cl at 118.9 nm.⁴⁶ Although, with this atomic line, Cl* should be probed by the present setup, we were unable to detect it. Observation with a conventional [3 + 1] scheme also failed. We also tried to find this line by using different compounds e.g., pyrolysis of CCl_4 , where a large amount of Cl* is formed (more than 50% of the Cl) and detected it by [2 + 1] and [3 + 1] REMPI, but surprisingly the listed Cl* line was not observed. Therefore, we conclude that the transition is either significantly perturbed or the calculated intensity is overestimated. Interestingly, Cantu et al. reported more than 400 VUV absorption lines of Cl and Cl* in two extensive papers, but they have not listed the 117.9 nm Cl* line as an observed transition.^{52,53} [3 + 1] REMPI detection at 356.7 nm was carried out by removing the tripling cell.

For characterizing the molecular beam, standard 118.2 nm (10.49 eV) photoionization (SPI) was employed, tripling the 354.7 nm output (15 mJ/pulse) of an Nd:YAG laser with $P_{Xe} = 10\text{-}12$ mbar. In one-color experiments, the dissociation laser was employed for ionization also with slightly higher energy (1.5-2.0 mJ/pulse) and focused by a quartz lens ($f = 200$ mm). The photon energy was calibrated using the Cl atomic lines. The ionization laser was scanned through the whole Doppler width of the atomic transitions for both one- and two-color experiments. Ions were detected by a dual-stage microchannel plate (MCP) detector equipped with a phosphorescent screen (P43). The front MCP was always kept at ground potential to ensure the field-free drift condition. For mass gating, the voltage at the back MCP was controlled by a high voltage switch operated at 10 Hz with 100 ns gate width. The recorded 2D image of the crushed newton sphere was digitized by a progressive-scan CCD camera (Prosilica GC1380H) after focusing by an achromatic object lens. Each image was accumulated over 5000 laser shots and separately recorded background images from both dissociation and ionization laser were subtracted to get the true two-color image. The resulting image was then symmetrized, and the 3D newton sphere was reconstructed via inverse Abel transformation with the pBASEX algorithm employing Legendre polynomials up to fourth order.^{48,54} Translational energy release distributions $P(E_T)$ were calibrated using the photodissociation of Cl_2 at 356.63 nm via $1_u \leftarrow 0_g^+$ ($X^1\Sigma_g$) excitation. The observed ion image and corresponding $P(E_T)$ (Figure 3.S1 in the Supporting Information) are consistent with the earlier report with perpendicular anisotropy and narrow translational energy distribution.⁵⁵ For one-color experiments, the background was measured at an off-resonance wavelength. To record the mass spectrum, the current generated by the MCP stack was amplified, and the corresponding voltage drop was detected by an oscilloscope. To measure the time dependence of Cl formation, the mass signal was monitored as a function of delay between the ionization and dissociation lasers. Ion images were recorded at different delay times ranging from ~ 5 to ~ 200 ns, and they all showed similar distributions.

The geometry optimizations and harmonic frequency calculations were carried out on the DFT/B3LYP/6-311++G** level of theory, using the Gaussian 09 program package.⁵⁶ The bond dissociation energy was estimated from the differences of computed energies at 0 K. All energies were corrected for zero point energies.

3.4 Results

[1 + 1'] REMPI of Cl.

The top panel in Figure 3.1 shows the REMPI spectrum of mass channel m/z 35 after dissociation of Ph-CO-Cl in a [1 + 1'] scheme. The ion intensity of

$^{35}\text{Cl}^+$ is plotted against the VUV wavenumbers. The $^2\text{D}_{5/2} \leftarrow ^2\text{P}_{3/2}^o$ transition appears as the most intense peak, while the shoulder represents the $^2\text{D}_{3/2} \leftarrow ^2\text{P}_{3/2}^o$ transition. To exclude the possible contribution from a $[3 + 1]$ REMPI process, we recorded mass spectra using 28040.1 cm^{-1} ($84120.3 \text{ cm}^{-1}/3$) with and without Xe in the gas cell (bottom panel). Trace b indicates that without Xe there is no signature of $^{35}\text{Cl}/^{37}\text{Cl}$, which confirms that the Cl^+ signal in the top panel results exclusively from a $[1 + 1']$ process, and no contribution from a $[3 + 1]$ process was present under the employed focusing conditions.

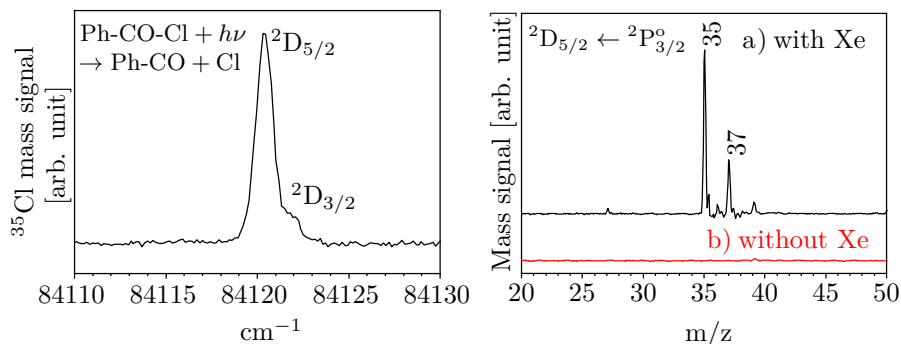


Figure 3.1: Left panel: REMPI scan of the atomic Cl from benzoyl chloride photodissociated at 237 nm and ionized in a $[1 + 1']$ process. Bottom panel: Mass spectra recorded with and without Xe in the tripling cell at 28040.1 cm^{-1} . The absence of Cl mass peaks in trace b excludes the possibility of a $[3 + 1]$ REMPI process and indicates that the generated Cl is ionized only in a $[1 + 1']$ process.

Absorption and Mass Spectra.

To identify the electronic states of Ph-CO-Cl correctly, we have measured the gas phase absorption spectrum of Ph-CO-Cl as depicted in Figure 3.2. There are three distinct humps at $\sim 280 \text{ nm}$ (S1), $\sim 255 \text{ nm}$ (S2), and $\sim 235 \text{ nm}$ (S3) that are consistent with previous work.^{33,57} The excitation wavelengths in our experiment are indicated by arrows. The nature of these states are reported to be $\pi^*(\text{ring}, \text{C}=\text{O}) \leftarrow n(\text{Cl}, \text{O})$ (S₁), $\pi^*(\text{ring}, \text{C}=\text{O}) \leftarrow \pi(\text{ring})$ (S₂) and $\pi^*(\text{ring}, \text{C}=\text{O}) \leftarrow \pi(\text{ring})$ (S₃) type.³³ All bands are structureless, which would be in agreement with a fast nonradiative relaxation.

Figure 3.3 compares normalized mass spectra recorded under different experimental conditions. The photoionization mass spectrum recorded at 118.2 nm is shown in the bottom trace, trace (d). This experiment is very useful to characterize the experimental conditions because it can efficiently ionize all species with an IE lower than 10.49 eV . The spectrum is dominated by the molecular ions, m/z 140 ($\text{PhCO}^{35}\text{Cl}$) and 142 ($\text{PhCO}^{37}\text{Cl}$) as well as 105 (PhCO), with

m/z 58 (CH_3COCH_3) used as calibrant. PhCO^+ was generated via dissociative photoionization (DPI) of the parent molecule (3.1), the reported appearance energy for (3.1) is 9.69 eV.⁵⁸



Other minor peaks are mainly due to the background signals from the reaction chamber. There is no indication of clusters present in the experimental conditions, as evident by the same mass spectrum depicted up to m/z 400 (Figure 3.S2 in the Supporting Information). Trace (c) shows a similar mass spectrum as the one given in the bottom trace of Figure 3.1, recorded with SPI of 118.9 nm (10.43 eV), resonant for $[1 + 1']$ ionization of atomic Cl. No Cl^+ signal is present, which indicates the absence of a one-color background signal. Only minute signatures of m/z 142, 140, and 105 are visible. This different signal-to-noise (S/N) ratio between 118.9 and 118.2 nm ionization can be explained by the higher laser power at 118.2 nm and the better conversion efficiency in Xe at 354.7 nm.

Traces (a) and (b) depict the same 118.9 nm m/z spectrum recorded after excitation with 237 and 279.6 nm light. The huge signals at m/z 35 (^{35}Cl) and 37 (^{37}Cl) in both spectra immediately reflect the efficiency of VUV for probing photofragmented Cl even with low power of dissociation light. The Cl signal was still substantial, even when we reduced the dissociation laser power to 1 mW without focusing. As trace (c) does not show any signs of Cl, it is evident that the Cl^+ peaks at trace (a) and trace (b) appear exclusively due to homolytic bond cleavage and not from DPI of Ph-CO-Cl.

It is difficult to quantify the relative dissociation probability at different wavelength without a suitable calibrant. The absorption cross section σ_{abs} at 237 nm is a factor of 3.5 larger compared to 279.6 nm (see Figure 3.2), but the Cl signal at 237 nm excitation is roughly an order of magnitude larger, indicating a more efficient photodissociation upon S_3 excitation.

Translational Energy Release Distribution of Cl.

We investigated the photodissociation of benzoyl chloride in two-color experiments at four different wavelengths, 279.6, 265, 253, and 237 nm. Furthermore, we conducted one-color experiments at 235.34 nm. We will start discussing the results obtained at 237 nm excitation, because they are most relevant for a comparison with previous work.

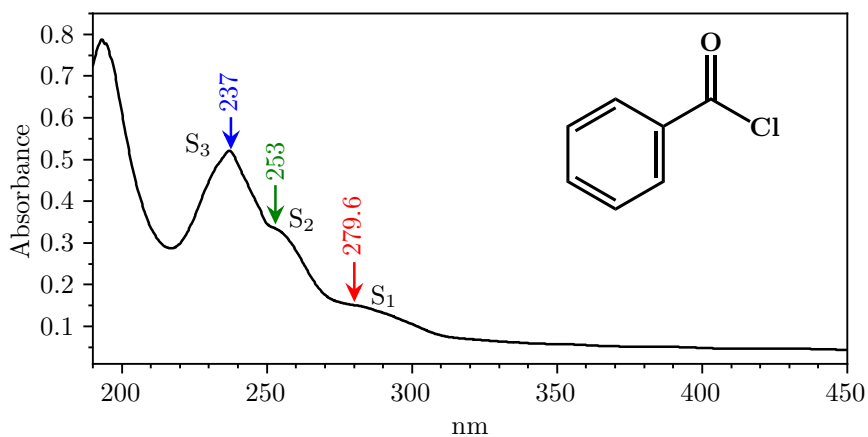


Figure 3.2: Gas phase absorption spectrum of the Ph-CO-Cl. Three electronic states appear as broad humps without any vibronic structures, indicating short excited-state lifetimes. The excitation wavelengths in the current study are indicated by the arrows.

237 nm Dissociation.

Trace a of Figure 3.4 shows the translational energy release distribution $P(E_T)$ of the ^{35}Cl photofragment generated from the initially excited S_3 state at 237 nm. The recorded 2D velocity map image is also shown in the side panel. The $P(E_T)$ was calculated from the reconstructed 2D slice of Cl^+ generated by $[1 + 1']$ REMPI, following photodissociation. In contrast to the previous report, we observed an isotropic, unimodal energy distribution rather than a bimodal one.³³ The calculated $P(E_T)$ was fitted with the empirical function (2).^{48,59,60}

$$P(E_T) = C \cdot (E_T)^a (E_T^{\max} - E_T)^b \quad (3.2)$$

Here a and b are adjustable parameters, C is a normalization constant, and E_T^{\max} is the maximum translational energy available for Cl after photodissociation. As evident from the right-hand side ion image of trace a, the photofragment angular distribution (PAD) is isotropic with the value of the β parameter nearly equal to zero, which immediately indicates a dissociation that proceeds on a time scale longer than a rotational period. Earlier calculations predicted the angle between transition dipole moment and the dissociating C-Cl bond to be $\sim 150^\circ$ for the excitation to the S_3 state. In case of a fast dissociation, a β -value of ~ 1.2 would be expected.³³

According to the momentum conservation law after photodissociation, relation 3.3 holds,

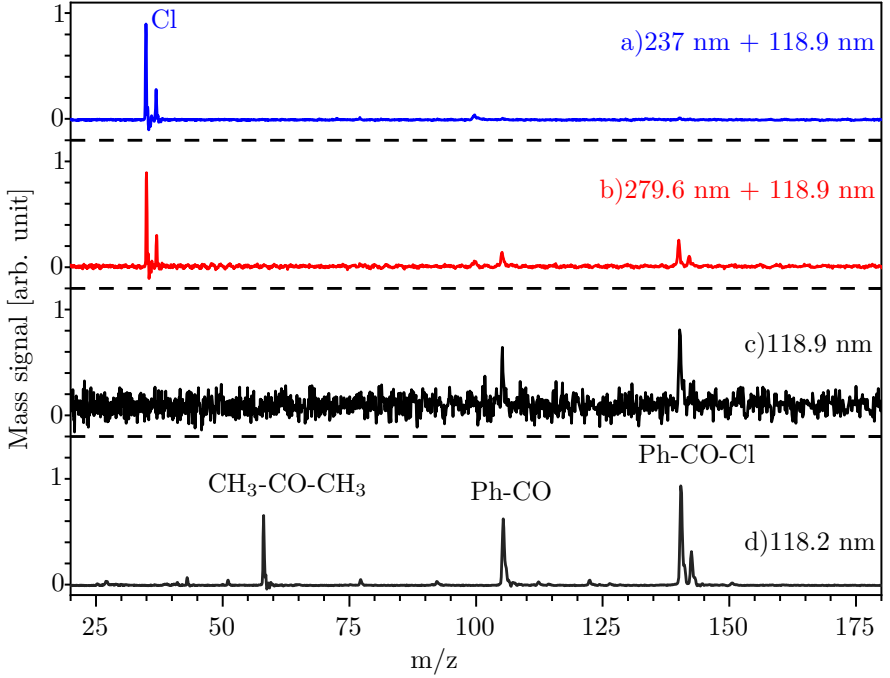


Figure 3.3: Mass spectra recorded by using different dissociation and ionization wavelengths. Trace d characterizes the molecular beam with SPI at 10.49 eV. Ph-CO at 105 is produced by dissociative photoionization of benzoyl chloride (m/z 140). Acetone (m/z 58) was used as a calibrant. Traces a and b indicate the Cl photofragment signal at two different excitation wavelengths probed by 118.9 nm [$1 + 1'$] REMPI. No Cl signal is observed with 118.9 nm only (trace c), which implies that no contribution from DPI is present in the current probing condition.

$$m_{\text{Cl}} \times v_{\text{Cl}} = m_{\text{Ph-CO}} \times v_{\text{Ph-CO}} \quad (3.3)$$

with m and v being the mass and velocity of the respective fragments. The excess energy (E_{excess}) for the departing fragments is given as

$$E_{\text{excess}} = (h\nu - \text{BDE}) \quad (3.4)$$

Thus, the maximum available translational energy for Cl is

$$E_T^{\text{max}}(\text{Cl}) = E_{\text{excess}} \times \frac{m_{\text{Ph-CO}}}{m_{\text{Ph-CO-Cl}}} \quad (3.5)$$

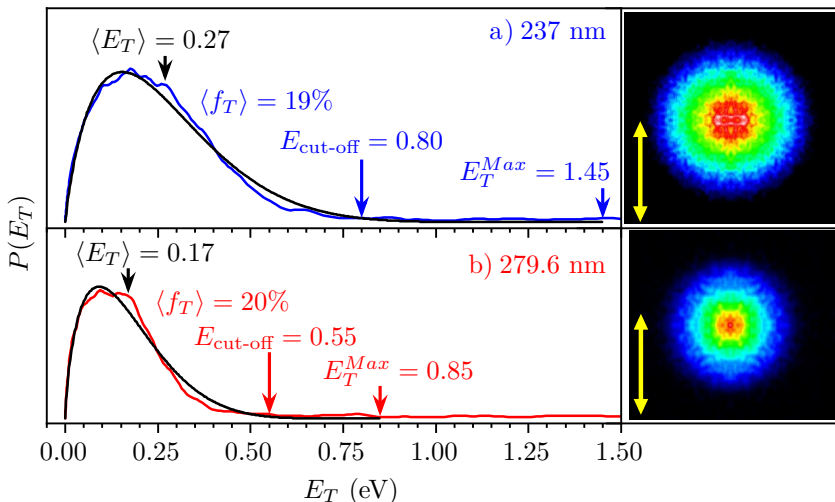


Figure 3.4: Translational energy distribution $P(E_T)$ of ^{35}Cl upon excitation to S_3 (upper trace) and S_1 state (lower trace). The blue and red curves indicate the experimental results, while the black curves represent a fit based on expression 3.2. Corresponding ion images after symmetrization are shown in side panels and the dissociation laser polarization is indicated by yellow double headed arrows. Smaller $\langle f_T \rangle$ values indicate that only a small fraction of the energy is released as translation. Both distributions appear similar, implying a single dissociation channel for C-Cl bond cleavage with a common mechanism from both states.

The C-Cl bond dissociation energy of Ph-CO-Cl computed on the DFT/B3LYP/6-311++ G** level is 3.30 eV, similar to the previous report.³³ Hence, at 237 nm excitation (5.32 eV) the maximum translational energy (E_T^{max} available for the departing Cl fragment would be 1.45 eV (Table 3.1). The average translational energy of ^{35}Cl , $\langle E_T \rangle$, is 0.27 eV; consequently, the expectation value for the total translational energy release is thus $\langle E_T \rangle$ released as translation is a more useful parameter than E_T when comparing photodissociation from different electronic states, as the amount of excess energy varies with excitation wavelength. The computed $\langle f_T \rangle$ is $\sim 19\%$. The most probable energy and the experimental cutoff E_{cutoff} were determined to be 0.18 (12%) and 0.80 eV (55%) respectively. The former indicates the maximum of the distribution, while the latter, estimated by eye, points out at which energy the distribution reaches baseline and indicates the maximum translational energy of the Cl atom actually has acquired after photodissociation. The time dependence for the Cl-atom loss is depicted in the Figure 3.S7, and the rise time of the Cl signal is about 20-30 ns, within the time resolution of current setup.

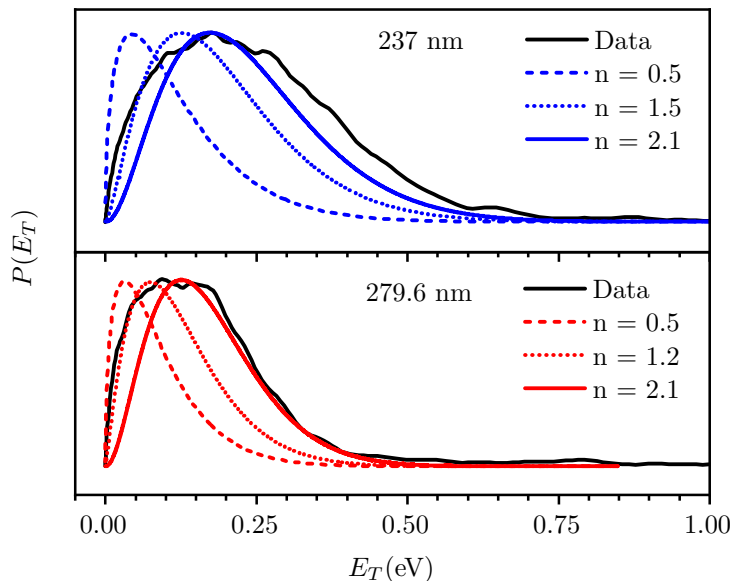


Figure 3.5: One-parameter fits of the experimental data (black line) following expression 6 with different values of n . A value of $n = 0.5$ corresponds to a prior distribution.

Although the two-parameter fit (3.2) is an excellent way to extract expectation values from the fit, it is an empirical approach without a sound physical basis. An alternative is a one-parameter fit, based on theoretical models. Quack suggested using a distribution function of the form (3.6) to mimic the more accurate, but also more complicated, behavior of phase space theory.⁶¹

$$P(E_T) = C \rho_P(E_T^{\max} - E_T) E_T^n \quad (3.6)$$

Here, n is an adjustable parameter, $0 < n < 3$, that reflects the character of the transition state (i.e., loose vs tight), ρ_P the (ro-)vibrational density of states of the product and C a normalization constant. The expectation value for the translational energy release, $\langle E_T \rangle$, can be found from a simplified procedure, employing the expression

$$\langle E_T \rangle = \int_0^E E_T P(E_T) dE = \frac{\int_0^{E_T^{\max}} \rho_P(E_T^{\max} - E_T) E_T^{n+1} dE_T}{\int_0^{E_T^{\max}} \rho_P(E_T^{\max} - E_T) E_T^n dE_T} \quad (3.7)$$

Table 3.1: Maximum Translational Energy Available for Fragmented $^{35}\text{Cl}(E_T^{\text{max}})$ at Different Photodissociation Wavelengths along with some Energy Parameters^a

$\lambda_{\text{diss}} \backslash \text{nm}$	$E_{\text{excess}} \backslash \text{eV}$	$\langle E_T^{\text{tot}} \rangle \backslash \text{eV}$	$\langle f_T \rangle$	$E_T^{\text{max}}(^{35}\text{Cl}) \backslash \text{eV}$	$E_{c-o}(^{35}\text{Cl}) \backslash \text{eV}$
237	1.93	0.36	0.19	1.45	0.80
253	1.60	0.29	0.18	1.20	0.70
265	1.38	0.25	0.18	1.04	0.55
279.6	1.13	0.23	0.20	0.85	0.55

^a E_T^{max} is calculated using eq 3.5. For $\langle f_T \rangle$, error bars of +5%/ - 10% are assumed.

and finding the value of n that reproduces the experimentally derived distribution. The denominator in (3.7) represents the normalization constant. In our computations, we approximated the integral by a sum over states. A value of $n = 0.5$ corresponds to the so-called prior distribution, which describes a perfectly statistical dissociation. The upper trace of Figure 3.5 shows that $P(E_T)$ cannot be described by such a prior distribution (dashed line), which indicates deviations from an ideal statistical process. A reasonable overall fit is achieved with $n = 2.1$ (solid lines), but it is evident that the rising part of the distribution is not represented well. From this fit, we derive $\langle f_T \rangle = 0.17$ at 237 nm for $n = 2.1$. Larger values of n would shift the distribution to unreasonable values of $\langle E_T \rangle$. The rising (low-energy) part of the distribution is fitted best with values around $n = 1.5$, which would correspond to $\langle f_T \rangle = 0.13$.

To check for a possible direct dissociation in an excited state, we computed the translational energy release expected in an impulsive model, using the expressions described by Tuck⁶² and by Galloway et al.⁶³ We found an expectation value $\langle f_T \rangle = 0.34$, i.e., considerably higher than the experimentally observed one. The values for the different models are compared in Tables S1 and S2 in the Supporting Information.

Further information on the dynamics should be accessible from the molecular counterfragment, Ph-CO. However, there is a large background contribution from dissociative photoionization of the precursor, see (3.1), which renders it impossible to extract the “true” two-color signal.

The previous study also investigated the HCl loss from benzoyl chloride and computed possible pathways.³³ We also detected HCl fragments in a one-color experiment at 236.00-235.07 nm. We observed a narrow spot in the center of the image that is interpreted as a contribution from the decomposition of benzoyl chloride in the sample line to the signal. Therefore, we believe that conclusions beyond the previous work are not warranted.

279.6 nm Dissociation.

To investigate the dependence of the photodissociation dynamics on the excess energy, we measured the $P(E_T)$ of ^{35}Cl after exciting Ph-CO-Cl at the blue edge of the S_1 state with 279.6 nm (4.43 eV). The calculated $P(E_T)$, as well as the corresponding velocity map image, are depicted in the lower trace of Figure 3.4. Like the distribution obtained upon excitation at 237 nm, it is also isotropic and unimodal with $\langle E_T \rangle = 0.17$ eV and $\langle E_T^{tot} \rangle = 0.23$ eV. Thus, nearly the same $\langle f_T \rangle$ value of 20% is computed. The most probable translational energy (0.13 eV, 15%), as well as experimental cutoff energy (0.55 eV, 65%), are also similar to the $P(E_T)$ from the S_3 state. Distributions based on expressions 3.6 and 3.7 are given in the lower trace of Figure 3.5. Again, the data cannot be fitted by a prior distribution (dashed line). Using $n = 2.1$ (solid line), eq 3.6 provides a reasonable fit to the high energy part of the distribution, whereas the rising edge is best approximated by $n = 1.2$. Overall, the one-parameter fit is more satisfactory at 279.6 nm than it is at 237 nm.

253 and 265 nm Dissociation.

Finally, we recorded two-color velocity map images of photodissociated ^{35}Cl upon excitation of Ph-CO-Cl at two additional wavelengths, 253 nm (in the region of the S_2 state) and 265 nm (in between S_1 and S_2). The corresponding distributions along with experimental images are depicted in Figure S₄ and S₅. Again, both distributions are unimodal in nature and resemble the ones recorded at other excitation wavelengths. The determined energy parameters are listed in Table 3.1. One-parameter fits using expressions 3.6 and 3.7 are presented in Figure 3.S6. Like values at 237 and 279.6 nm, $P(E_T)$ cannot be fitted by a prior distribution. A good overall fit is obtained with $n = 2.1$, while the rising part of the distribution is best represented by $n = 1.3$.

235.34 nm Dissociation.

For a direct comparison with the previous work, we have also measured a one-color image of ^{35}Cl exciting Ph-CO-Cl at 235.34 nm and detecting Cl in a $[2 + 1]$ REMPI transition. The calculated $P(E_T)$ is depicted in Figure 3.6. An additional contribution appears at higher translational energies, although it is not as intense as reported by Saha et al. The component can be fitted by an additional Gaussian, which is centered at $\langle E_T \rangle = 1.11$ eV. It is associated with a slightly negative β -value. For comparison, Saha et al. reported $\langle E_T \rangle = 0.72$ eV. As one-color experiments required focusing of a laser beam, dissociation after multiphoton excitation, leading to dissociation from higher electronic states of benzoyl chloride or dissociative photoionization is an explanation for this higher kinetic energy trail of the Cl distribution. The negative β -value indicates a

direct dissociation. The process can be suppressed, when the excitation laser is not used for detection.

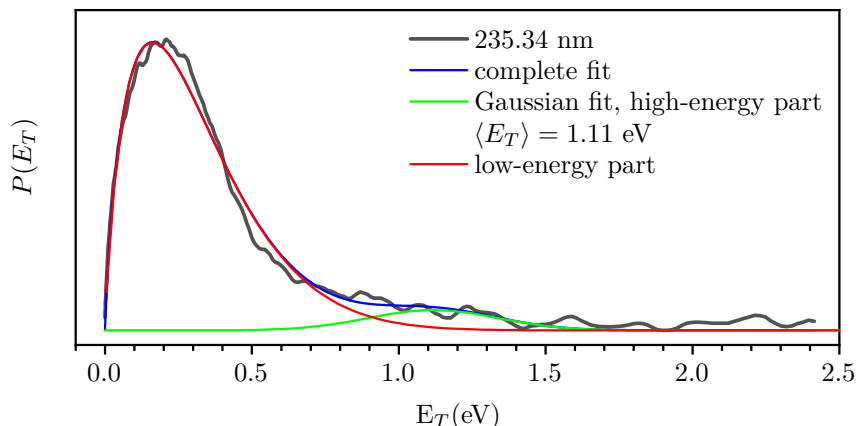


Figure 3.6: Cl photofragment $P(E_T)$ recorded in a one-color experiment (black) shows a contribution at higher translational energies that can be fitted by a Gaussian centered at 1.11 eV. The contribution is possibly due to unwanted multiphoton higher-order processes results from focusing.

We also probed the Cl* photofragment in a one-color experiment at 235.21 nm. Compared to the Cl contribution given in Figure 3.6, the high-energy trail was more pronounced. However, as multiphoton processes might contribute to the high energy part of the distribution, it is difficult to extract additional insight into the dynamics. Branching ratios Cl/Cl* were extracted from the integrated absorption profiles (Figure 3.S8), assuming a relative ionization probability of 0.85.^{64,65} Parameters like laser power, background pressure, and time delay were systematically varied. The branching ratio was always larger than 9:1; thus, a propensity for formation of Cl in its lower spin-orbit state is evident. Although in the one-color experiments a multiphoton contribution cannot be excluded, this propensity is in agreement with the absence of a Cl* signal in two-color experiments using a [3 + 1] detection scheme in conjunction with 235 nm excitation.

3.5 Discussion

C-Cl Cleavage.

In their earlier one-color experiment, Saha et al. reported two dissociation channels for C-Cl bond cleavage from the S₃ state by fitting their experimental

TOF profile with a bimodal translational energy distribution.³³ The experimental PAD was isotropic in nature with calculated $\langle E_T \rangle$ values of 0.72 and 0.15 eV. The authors concluded two different dissociation pathways from the initially excited S_3 state. In the high-energy channel dissociation was supposed to proceed via an exit barrier in the S_1 state, which is populated by $S_3 \rightarrow S_1$ IC. The low-energy contribution was explained by a statistical dissociation following $S_3 \rightarrow S_0$ internal conversion (IC). In contrast, our two-color experiments show a unimodal $P(E_T)$ of the Cl photofragment, indicating that one C-Cl dissociation channel dominates at all excited states. The distribution agrees qualitatively with the lower energy distribution of the previous work, although we find a larger value of $\langle f_T \rangle = 17\%$ instead of 7%. In one-color experiments, a weak contribution at high translational energies is present, centered at $\langle E_T \rangle = 1.11$ eV rather than 0.72 eV. Note that in the experiments of Saha et al, the translational energy distribution has been derived by forward convolution from the TOF-profile, which is equivalent to a one-dimensional projection of the velocity distribution. Since different distributions can result in the same TOF profile, it is difficult to avoid ambiguities. In contrast, an image constitutes a two-dimensional projection and at least for cylindrical symmetry the full 3D distribution can be derived. Therefore, imaging experiments reflect $P(E_T)$ more accurately.

Interestingly though, the experimental $P(E_T)$ cannot be fitted by a prior distribution ($n = 0.5$), but an impulsive model suggests almost twice the translational energy release and is also not adequate. A one-parameter fit (3.6) using $n = 2.1$ on the other hand describes $P(E_T)$ reasonably well, although the low-energy part of the distribution is better describes by smaller values of n between 1.2 and 1.5. According to Quack,⁶¹ this value is within the range consistent with a statistical dissociation. An impulsive model, which is more adequate for a direct dissociation yields $\langle f_T \rangle = 34\%$, much higher than the experimentally observed values. Furthermore, the isotropic PAD excludes direct dissociation (assuming that an accidental emission of photofragments at the magic angle relative to the transition dipole moment at all excitation energies is unlikely). A slow dissociation in the excited-state (slower than a rotational period and thus in agreement with $\beta = 0$) is in contradiction with the diffuse absorption spectrum that suggests short excited state lifetimes. Nevertheless, the inadequacy of a prior distribution indicates deviations from an ideal statistical model and suggests that the reaction proceeds along a complicated reaction coordinate. Bond breaking might be preceded by ring opening or isomerization. Such rearrangement reactions have been computed by Saha et al. for possible HCl loss.³³ It has also been shown by Neumark and co-workers that upon dissociation over an exit barrier a substantial fraction of the barrier height is converted to translational energy of the fragments.⁶⁶ The unusually high $\langle f_T \rangle$ could thus indicate a significant reverse barrier in the fragmentation. Other reasons for

a deviation from an ideal statistical model have been summarized in a recent review.⁶⁷

Similar $\langle f_T \rangle$ values, a similar shape of the distributions and an isotropic PAD at all excitation energies imply that photodissociation from all states shares the same mechanism. As indicated in Figure 3.7, we conclude from our data that excitation is followed by IC to the electronic ground state and dissociation occurs from there. As the available excess energy is insufficient for electronic excitation of either fragment (Ph-CO and Cl), based on current observations it can be concluded that the actual dissociation is predominately a ground state phenomenon from vibrationally hot molecules generated by rapid internal conversion (Figure 3.7). Dissociation from a triplet state, populated by ISC (intersystem crossing), can be excluded based on the energetics. At 279.6 nm excitation, the available excess energy is 1.13 eV. As the maximum translational energy $E_{\text{cut-off}}$ measured for Cl is ≈ 0.55 eV, the energy of such a triplet state would have to be unreasonably low. As all ion images are isotropic in nature, it can be assumed that the dissociation time scale is slow compared to molecular rotation. We note that in the photodissociation of cyclic hydrocarbons^{68,69} and aryl chlorides at 193 nm¹⁶ that fragment in a statistical fashion, values for $\langle f_T \rangle$ between 10 and 12% have been observed. Larger $\langle f_T \rangle$ of 15 to 20% have been found in the H atom loss from alkyl radicals^{16,68,70} and from benzyl.^{71,72}

In our experiment, we also observed a rise time of the Cl^+ mass signal of ~ 10 -30 ns (Figure 3.S7 in the Supporting Information), thus the dissociation dynamics is not resolvable temporally by our current ns laser system. As we could not identify a transition state in S_0 employing standard quantum chemical calculations, RRKM computations contribute only limited information.

It is interesting to note that due to fast energy dissipation from the initially excited state, aryl chlorides like chlorobenzene and chlorotoluene show the indirect “hot molecule” dissociation predominantly over the direct mechanism that mainly operates in alkyl chlorides.^{9,17} In Ph-CO-Cl, this fast relaxation causes the short-excited state lifetime, which ultimately results in the structureless broad absorption spectrum. Nevertheless, radiative deactivation and ISC might compete with IC. The Cl yield observed upon 237 nm excitation as compared to 279.6 nm, which is larger by more than the difference in σ_{abs} indicates a higher photodissociation quantum yield at higher excitation energies. Presumably, processes that can compete with IC upon S_1 excitation become less relevant in the S_3 state. However, a quantitative analysis is not warranted.

Several aliphatic α , β -unsaturated carbonyl chloride like allyl chloride, acryloyl chloride, and propargyl chloride show two Cl dissociation channels when excited with 193 nm light with the higher kinetic energy channel as predominant one,^{22,23,28,29} but for aromatic carbonyl chlorides, there is no report other than the one from Saha et al. The group also reported that the 2-furoyl chloride dissociation proceeds in a similar manner.⁷³

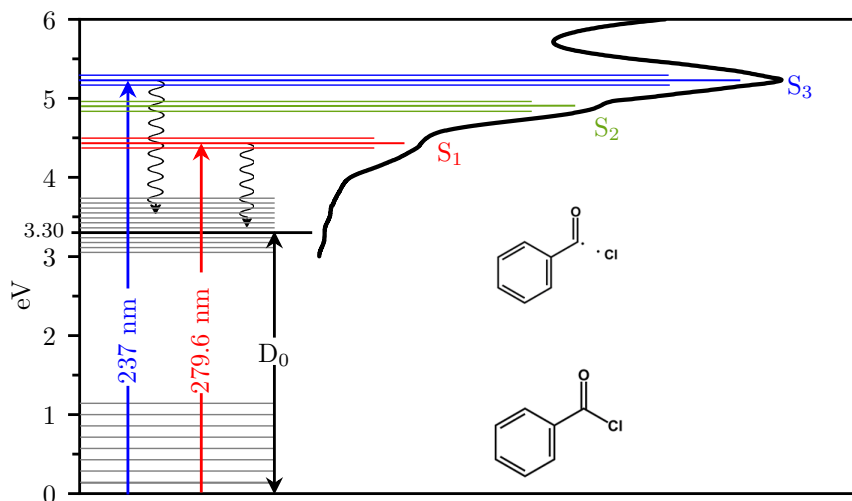


Figure 3.7: Proposed scheme for photodissociation of Ph-CO-Cl from both S₃ and S₁ states. The UV-vis spectrum is also depicted for comparison. The electronic states excited in the current study are indicated by red, green and blue. Excitation is followed by fast IC to S₀ resulting in a dissociation from vibrationally hot molecule. This rapid relaxation is most likely responsible for the structureless absorption spectrum.

For photodissociation of chlorinated molecules, the spin-orbit branching ratio often gives additional information about the mechanism. As noted above, we could not detect Cl* via [1 + 1'] REMPI using VUV and detection in two-color experiments using a [3 + 1] scheme at 355 nm led to no observable Cl* signal. To determine the spin-orbit branching ratio, we therefore had to rely on the one-color scheme at 235 nm. In agreement with Saha et al. we found a propensity of Cl formation, but determined a larger Cl/Cl* ratio of about 9:1 (Figure 3.S8). The dominance of Cl over Cl* confirms the efficient deactivation to S₀ and subsequent dissociation from the ground state, although the small Cl* contribution indicates the existence of minor channels to the photodissociation dynamics. The deviation of the experimental P(ET) from the one-parameter fit (3.6) that increases with excitation energy indicates that at 237 nm these minor channels might increase in importance. Note that the direct photodissociation of alkyl chlorides like CH₃Cl, CD₃Cl and C₂H₅Cl at 193 nm leads to a preponderance of Cl*.¹⁴

C-C Cleavage.

Apart from the C-Cl bond cleavage, there may be an additional C-C dissociation channel present in Ph-CO-Cl which leads to the production of COCl when excited at the S_3 level.



Saha et al. predicted that reaction 3.8 was endothermic by 111 kJ/mol (1.15 eV) compared to C-Cl bond dissociation; nevertheless, the reaction is energetically possible at 235 nm. In the photoionization mass spectrum after 237 nm excitation (Figure 3.S2), no COCl signal is visible. As an experimental ionization energy of COCl is not available in the literature, we computed it as 8.69 eV at the B3LYP/6-311++G** level. It should thus be detected under our experimental conditions. This suggests that C-C cleavage is only a minor channel at 237 nm excitation, if present at all.

3.6 Conclusion

The photodissociation of benzoyl chloride has been investigated by detecting the chlorine atom photofragment via $[1 + 1']$ photoionization. This scheme can be applied easily in combination with VMI to explore the photodissociation of chlorinated compounds. Previously, Cl was probed by either $[2 + 1]$ or $[3 + 1]$ one-color REMPI, schemes that are prone to have contributions from multiphoton processes due to focusing of the laser beam, in particular when applied to molecules with an aromatic chromophore. However, one disadvantage is that Cl^* cannot be easily probed by this two-color scheme. We have used the $[1 + 1']$ scheme for studying the photodissociation of benzoyl chloride after excitation to the S_1 , S_2 , and S_3 states. In all velocity map images of the Cl fragment, a unimodal translational energy distribution was observed. The distribution is isotropic, implying $\beta = 0$ and around 18-20% of the excess energy are released as translation. The observed expectation value for the translational energy is neither described by the (ideal statistically) prior distribution nor by the impulsive model, which suggest a significantly higher translational energy release of 34%. Despite the comparably high translational energy release, it is concluded that the photodissociation is in better agreement with a statistical dissociation mechanism, supported by the isotropic photofragment angular distribution, the large Cl/Cl* ratio of 9:1 and the fit of $P(E_T)$ using a more flexible one-parameter function that has been shown to describe statistical dissociation processes. The unusually large translational energy release might be due to significant reverse barrier along the reaction coordinate. The C-Cl bond is cleaved

from the vibrationally excited S_0 state, which is populated by rapid internal conversion from the photoexcited electronic states. Diffuse absorption bands indicate a short excited-state lifetime, but the isotropic photofragment angular distribution rules out a direct excited state distribution. One-color experiments at 235 nm found a Cl/Cl* branching ratio of about 9:1. Nevertheless, additional minor photodissociation pathways might increase in relevance at higher excitation energies. In contrast, a bimodal translational energy distribution was reported in previous one-color TOF profiling experiment that obtained a translational energy distribution by forward convolution of the TOF profile. The current study also finds no evidence for cleavage of the C-C bond, which would produce COCl fragments.

3.7 Acknowledgements

This work has been financially supported by the Deutsche Forschungsgemeinschaft, Grants GRK 2112 and FI 575/13-1.

3.8 Supplementary Information

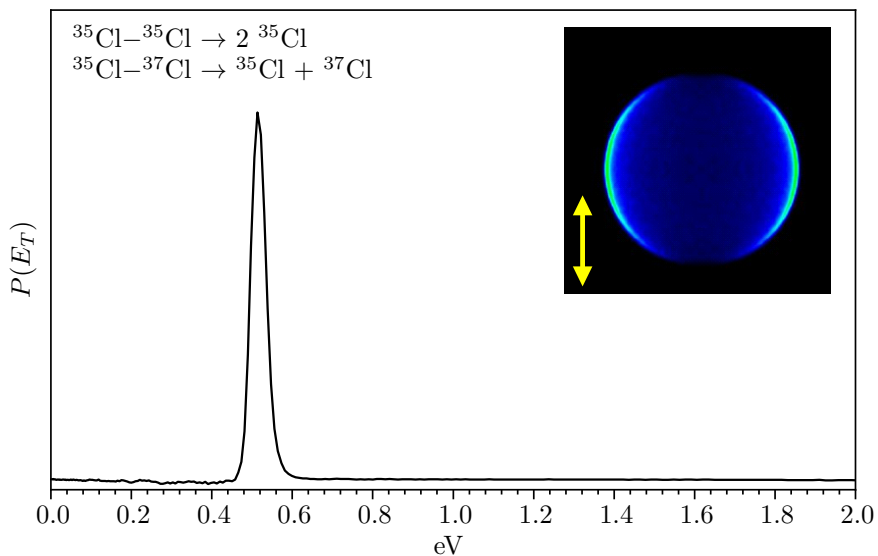


Figure 3.S1: VMI and corresponding $P(E_T)$ of ^{35}Cl from photodissociation of Cl_2 at 356.6 nm. As expected, it appears as a sharp narrow distribution with perpendicular anisotropy ($\beta = -1$).

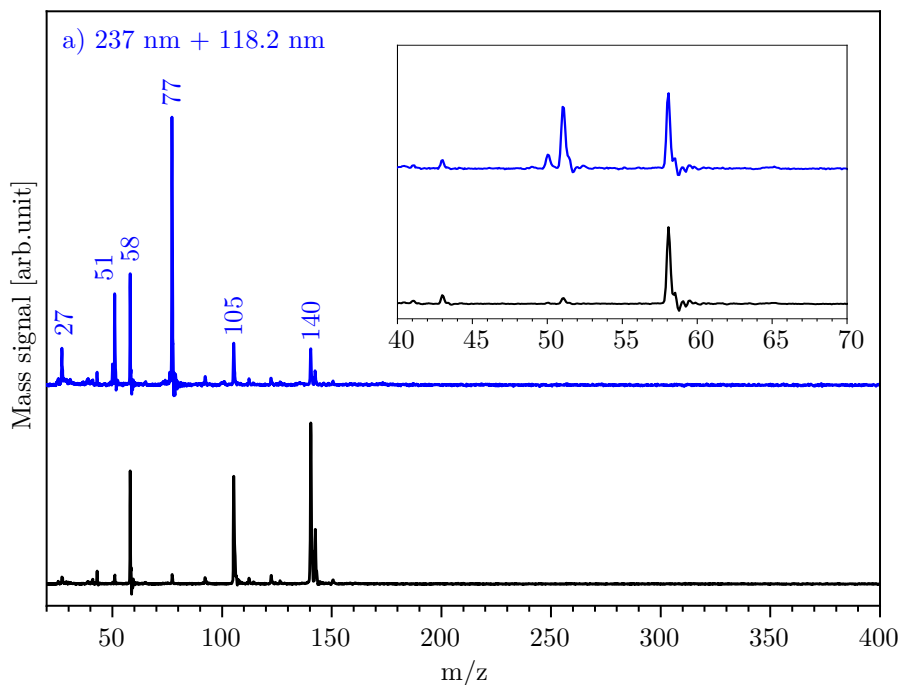


Figure 3.S2: Single photon 118.2 nm photoionization mass spectra of Ph-CO-Cl. A magnified section of the low mass range is shown as inset. Trace b) confirms the absence of cluster formation under our experimental conditions. Trace a) indicates the species generated after 237 nm dissociation and the relative intensity of the $m/z=105$ (Ph-CO) increases compared to $m/z=140$ (Ph-CO-Cl). However, most of the Ph-CO fragment ionizes dissociatively as evidenced by the large increase of daughter fragments ($m/z=77, 51, 27$). The inset spectra show no mass peak at 63 (COCl), indicating that C-C bond fragmentation is a minor channel in the photodissociation.

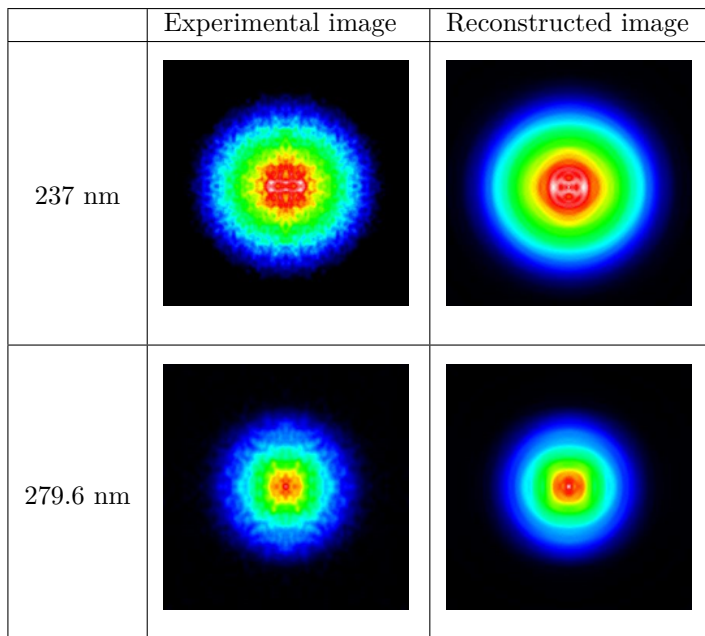


Figure 3.S3: Comparison of the experimentally measured symmetrized velocity map images of fragmented Cl with the reconstructed images. It was reconstructed by inverse Abel transformation employing the pBASEX algorithm. Legendre polynomials up-to 4 th order have been used for this purpose. The $P(E_T)$ was calculated from the reconstructed image.

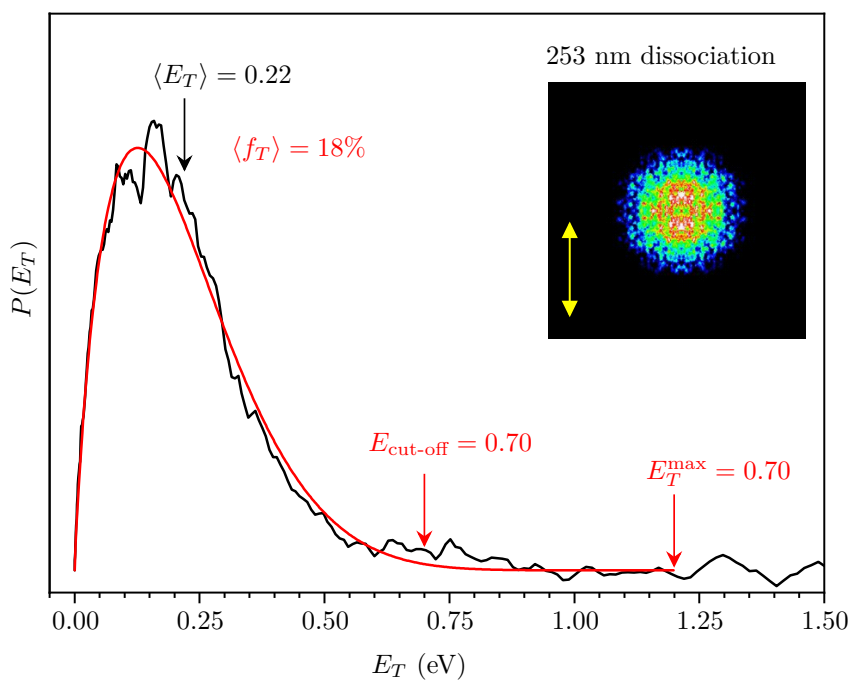


Figure 3.S4: Translational energy distribution $P(E_T)$ of photodissociated ^{35}Cl upon excitation to S_3 state at 253 nm. The black curve indicates the experimental result while the red curve represents a simulation based on expression (3.2).

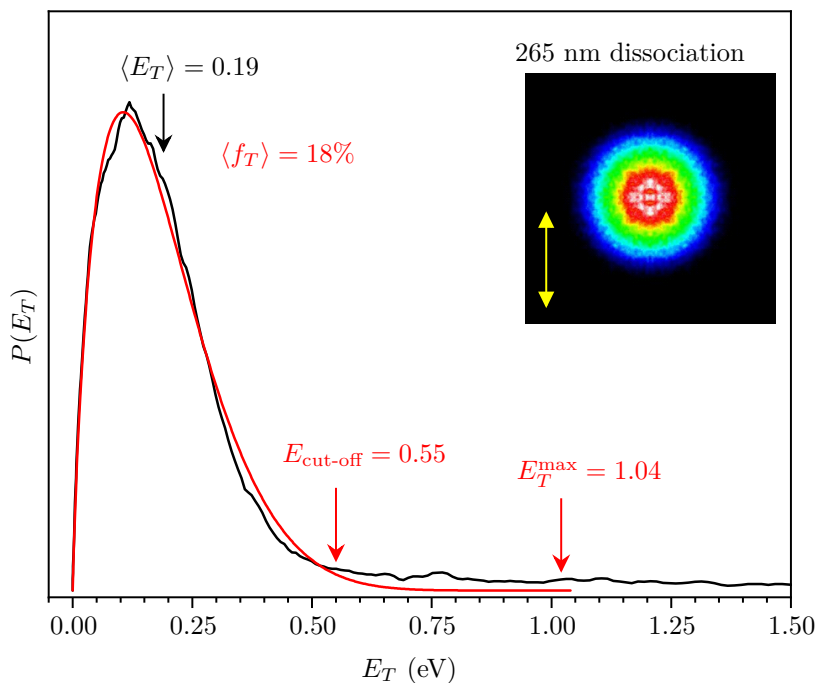


Figure 3.S5: Translational energy distribution $P(E_T)$ of photodissociated ^{35}Cl upon excitation to 265 nm. The black curve indicates the experimental result while the red curve represents a simulation based on expression (3.2).

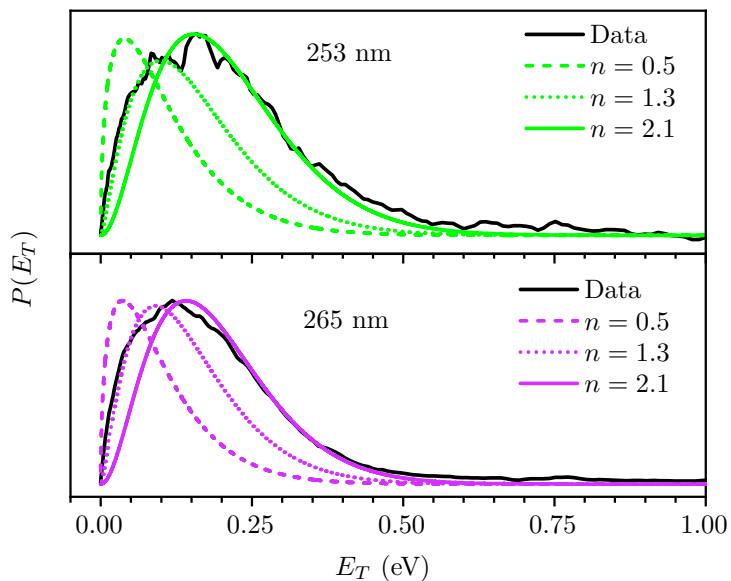


Figure 3.S6: Fit of the experimental translational energy distributions $P(E_T)$ of photodissociated ^{35}Cl (black) at 253 nm (top) and 265 nm (bottom) using function (6), see main paper. As visible, the data cannot be described by a prior distribution, which corresponds to $n = 0.5$ (dashed lines). The low energy part is best fitted using $n = 1.3$, whereas the high energy part is better fitted with $n = 2.1$.

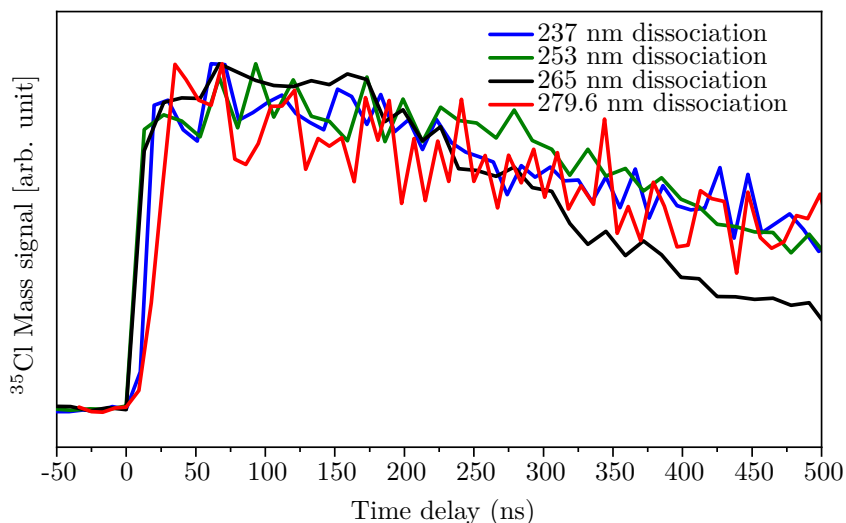


Figure 3.S7: Time dependence of the Cl signal at four dissociating wavelengths. The ^{35}Cl mass signal is measured as a function of delay between dissociation and ionization lasers. The step growth of mass signal implies the time for dissociation, while the slow decay indicates the fly-out of the Cl atom from the ionization volume. The rise time at all wavelengths is 20-30 ns.

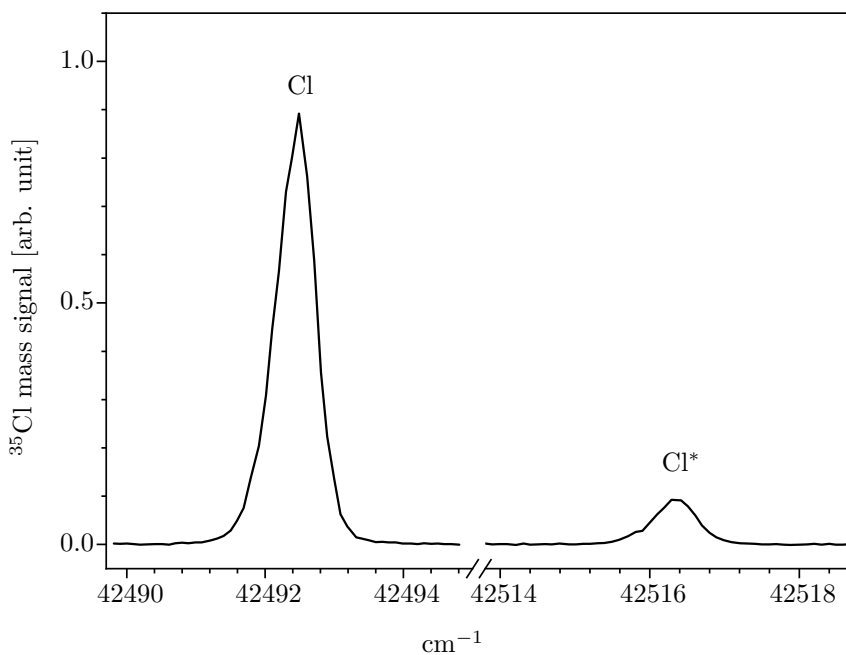


Figure 3.S8: [2 + 1] REMPI spectra of fragmented Cl and Cl* after photodissociation of Ph-CO-Cl recorded in one-color experiment. The areas under curves are used to determine the branching ratio.

Table 3.S1: Comparison of the fraction of excess energy released as translation computed in different models along with experimental values.

$\lambda_{\text{diss}}/\text{nm}$	$E_{\text{excess}}/\text{nm}$	$\langle f_T \rangle$			
		Two-parameter fit	One parameter fit ($n = 2.1$)	Prior distribution ($n = 0.5$)	Impulsive model
237	1.93	19%	17%	8%	34%
253	1.60	18%	18%	9%	34%
265	1.38	18%	18%	10%	34%
279.6	1.13	20%	20%	10%	34%

Table 3.S2: Translational energy release computed by the impulsive model as described in References.^{62,63}

$\lambda_{\text{diss}}/\text{nm}$	$E_{\text{excess}}/\text{nm}$	$E_T^{\text{tot}}/\text{eV}$	$E_T^{\text{max}}(^{35}\text{Cl})/\text{eV}$	$E_T(^{35}\text{Cl})/\text{eV}$	f_T
237	1.93	0.65	1.45	0.49	33.8%
253	1.60	0.55	1.20	0.41	34.2%
265	1.38	0.47	1.04	0.35	33.7%
279.6	1.13	0.39	0.85	0.29	34.1%

3.9 Bibliography

- (1) Ravishankara, A. R. *Proc. Natl. Acad. Sci. U.S.A.* **2009**, *106*, 13639–13640.
- (2) Faxon, C. B.; Allen, D. T. *Environ. Chem.* **2013**, *10*, 221–233.
- (3) Young, C. J. et al. *Atmospheric Chem. Phys.* **2014**, *14*, 3427–3440.
- (4) Hossaini, R.; Chipperfield, M. P.; Saiz-Lopez, A.; Fernandez, R.; Monks, S.; Feng, W.; Brauer, P.; Glasow, R. V. *J. Geophys. Res. Atmos.* **2016**, *121*, 14, 271–14, 297.
- (5) Pechtl, S.; von Glasow, R. *Geophys. Res. Lett.* **2007**, *34*, L11813-L11817.
- (6) Tsai, W. T. *Toxics* **2017**, *5*, 23.
- (7) Wayne, R. P. *Nature* **1979**, *280*, 521.
- (8) Freedman, A.; Yang, S. C.; Kawasaki, M.; Bersohn, R. *J. Chem. Phys.* **1980**, *72*, 1028–1033.
- (9) Wang, G. J.; Zhu, R. S.; Zhang, H.; Han, K. L.; He, G. Z.; Lou, N. Q. *Chem. Phys. Lett.* **1998**, *288*, 429–432.
- (10) Ahmed, M.; Peterka, D. S.; Regan, P.; Liu, X.; Suits, A. G. *Chem. Phys. Lett.* **2001**, *339*, 203–208.
- (11) Lambert, H. M.; Dagdigian, P. J. *Chem. Phys. Lett.* **1997**, *275*, 499–505.
- (12) Lin, J. J.; Chen, Y.; Lee, Y. Y.; Lee, Y. T.; Yang, X. *Chem. Phys. Lett.* **2002**, *361*, 374–382.
- (13) Matsumi, Y.; Das, P. K.; Kawasaki, M. *J. Chem. Phys.* **1990**, *92*, 1696–1701.
- (14) Matsumi, Y.; Das, P. K.; Kawasaki, M. *J. Chem. Phys.* **1992**, *97*, 5261.
- (15) Won, D. S.; Kim, M. S.; Choe, J. C.; Ha, T. K. *J. Chem. Phys.* **2001**, *115*, 5454–5460.
- (16) Ichimura, T.; Mori, Y.; Shinohara, H.; Nishi, N. *J. Chem. Phys.* **1997**, *107*, 835–842.
- (17) Lin, M. F.; Huang, C. L.; Kislov, V. V.; Mebel, A. M.; Lee, Y. T.; Ni, C. K. *J. Chem. Phys.* **2003**, *119*, 7701–7704.
- (18) Liu, Y. J.; Persson, P.; Lunell, S. *J. Chem. Phys.* **2004**, *121*, 11000–11006.
- (19) Umemoto, M.; Seki, K.; Shinohara, H.; Nagashima, U.; Nishi, N.; Kinoshita, M.; Shimada, R. *J. Chem. Phys.* **1985**, *83*, 1657–1666.
- (20) Browning, P. W.; Kitchen, D. C.; Arendt, M. F.; Butler, L. J. *J. Phys. Chem.* **1996**, *100*, 7765–7771.
- (21) Myers, T. L.; Kitchen, D. C.; Hu, B.; Butler, L. J. *J. Chem. Phys.* **1996**, *104*, 5446.

- (22) Morton, M. L.; Butler, L. J.; Stephenson, T. A.; Qi, F. *J. Chem. Phys.* **2002**, *116*, 2763–2775.
- (23) McCunn, L. R.; Bennett, D. I.; Butler, L. J.; Fan, H.; Aguirre, F.; Pratt, S. T. *J. Phys. Chem.* **2006**, *110*, 843–850.
- (24) Foley, C. D.; Joalland, B.; Alavi, S. T.; Suits, A. G. *Phys. Chem. Chem. Phys.* **2018**, *20*, 27474–27481.
- (25) Person, M. D.; Kash, P. W.; Butler, L. J. *J. Phys. Chem.* **1992**, *96*, 2021–2023.
- (26) Deshmukh, S.; Hess, W. P. *J. Chem. Phys.* **1994**, *100*, 6429–6433.
- (27) Martin, X.; Moreno, M.; Lluch, J. M. *J. Chem. Soc., Faraday trans.* **1996**, *92*, 373–375.
- (28) Szpunar, D. E.; Miller, J. L.; Butler, L. J.; Qi, F. *J. Chem. Phys.* **2004**, *120*, 4223–4230.
- (29) Yang, C.; Wu, W.; Liu, K.; Wang, H.; Su, H. *Sci. China Chem.* **2012**, *55*, 359–367.
- (30) Lee, P. W.; Scrape, P. G.; Butler, L. J.; Lee, Y. P. *J. Phys. Chem.* **2015**, *119*, 7293–7304.
- (31) Pérez-Soto, R.; Vázquez, S. A.; Martínez-Núñez, E. *Phys. Chem. Chem. Phys.* **2016**, *18*, 5019–5026.
- (32) Kawade, M.; Saha, A.; Upadhyaya, H. P.; Kumar, A.; Naik, P. D.; Bajaj, P. N. *J. Phys. Chem.* **2011**, *115*, 1538–1546.
- (33) Saha, A.; Kawade, M.; Sengupta, S.; Upadhyaya, H. P.; Kumar, A.; Naik, P. D. *J. Phys. Chem.* **2014**, *118*, 1185–1195.
- (34) Whitaker, B. J., *Imaging in Molecular Dynamics: Technology and Applications*; Cambridge University Press: 2003.
- (35) Butler, L. J.; Neumark, D. M. *J. Phys. Chem.* **1996**, *100*, 12801–12816.
- (36) Ashfold, M. N.; Nahler, N. H.; Orr-Ewing, A. J.; Vieuxmaire, O. P.; Toomes, R. L.; Kitsopoulos, T. N.; Garcia, I. A.; Chestakov, D. A.; Wu, S. M.; Parker, D. H. *Phys. Chem. Chem. Phys.* **2006**, *8*, 26–53.
- (37) Greaves, S. J.; Rose, R. A.; Orr-Ewing, A. J. *Phys. Chem. Chem. Phys.* **2010**, *12*, 9129–9143.
- (38) Chandler, D. W.; Houston, P. L.; Parker, D. H. *J. Chem. Phys.* **2017**, *147*, 013601–013608.
- (39) Röder, A.; Petersen, J.; Issler, K.; Fischer, I.; Mitrić, R.; Poisson, L. *J. Phys. Chem.* **2019**, *123*, 10643–10662.
- (40) Lockyer, N. P.; Vickerman, J. C. *Laser Chemistry* **1997**, *17*, 139–159.
- (41) Tsai, S. T.; Lin, C. K.; Lee, Y. T.; Ni, C. K. *Rev. Sci. Instrum.* **2001**, *72*, 1963–1969.

-
- (42) Lau, K. C.; Liu, Y.; Butler, L. J. *J. Chem. Phys.* **2005**, *123*, 054322–054330.
- (43) Townsend, D.; Li, W.; Lee, S. K.; Gross, R. L.; Suits, A. G. *J. Phys. Chem.* **2005**, *109*, 8661–8674.
- (44) Albert, D. R.; Davis, H. F. *Phys. Chem. Chem. Phys.* **2013**, *15*, 14566–14580.
- (45) Bain, M.; Hansen, C. S.; Ashfold, M. N. *J. Chem. Phys.* **2018**, *149*, 081103–081107.
- (46) Radziemski, L. J.; Kaufman, V. *J. Opt. Soc. Am.* **1969**, *59*, 424.
- (47) Arepalli, S.; Presser, N.; Robie, D.; Gordon, R. J. *Chem. Phys. Lett.* **1985**, *118*, 88–92.
- (48) Pachner, K.; Steglich, M.; Hemberger, P.; Fischer, I. *J. Chem. Phys.* **2017**, *147*, 084303–084311.
- (49) Steinbauer, M.; Giegerich, J.; Fischer, K. H.; Fischer, I. *J. Chem. Phys.* **2012**, *137*, 014303.
- (50) Demtroder, W.; Inguscio, M., *Applied Laser Spectroscopy*; Plenum Press: 1990.
- (51) Ganeev, R. A.; Usmanov, T. *J. Opt. A-Pure Appl. Op.* **2000**, *2*, 550–556.
- (52) Cantu, A. M.; Parkinson, W. H.; Grisendi, T.; Tagliaferri, G. *Phys. Scr.* **1985**, *31*, 579–586.
- (53) Cantu, A. M.; Parkinson, W. H. *Phys. Scr.* **1988**, *37*, 336–341.
- (54) Garcia, G. A.; Nahon, L.; Powis, I. *Rev. Sci. Instrum.* **2004**, *75*, 4989–4996.
- (55) Samartzis, P. C.; Sakellariou, I.; Gougousi, T.; Kitsopoulos, T. N. *J. Chem. Phys.* **1997**, *107*, 43–48.
- (56) Frisch, M. J. et al., *Gaussian 09, Rev. B.01*; Gaussian, Inc.: 2016.
- (57) Caralp, F.; Foucher, V.; Lesclaux, R.; Wallington, T. J.; Hurley, M. D. *Phys. Chem. Chem. Phys.* **1999**, *1*, 3509–3517.
- (58) McLoughlin, R. G.; Traeger, J. C. *Organic Mass Spectrometry* **1979**, *14*, 434–438.
- (59) North, S. W.; Marr, A. J.; Furlan, A.; Hall, G. E. *J. Phys. Chem.* **1997**, *101*, 9224–9232.
- (60) Deyerl, H. J.; Fischer, I.; Chen, P. *J. Chem. Phys.* **1999**, *111*, 3441–3448.
- (61) Quack, M. *Chem. Phys.* **1980**, *51*, 353–367.
- (62) Tuck, A. F. *J. Chem. Soc., Faraday trans.* **1977**, *73*, 689–708.
- (63) Galloway, D. B.; Glenewinkel-Meyer, T.; Bartz, J. A.; Huey, L. G.; Crim, F. F. *J. Chem. Phys.* **1994**, *100*, 1946–1952.

- (64) Liyanage, R.; Yang, Y. A.; Hashimoto, S.; Gordon, R. J.; Field, R. W. *J. Chem. Phys.* **1995**, *103*, 6811–6814.
- (65) Regan, P. M.; Langford, S. R.; Ascenzi, D.; Cook, P. A.; Orr-Ewing, A. J.; Ashfold, M. N. *Phys. Chem. Chem. Phys.* **1999**, *1*, 3247–3251.
- (66) Osborn, D. L.; Choi, H.; Mordaunt, D. H.; Bise, R. T.; Neumark, D. M.; Rohlffing, C. M. M. *J. Chem. Phys.* **1997**, *106*, 3049–3066.
- (67) Jayee, B.; Hase, W. L. *Annu. Rev. Phys. Chem.* **2020**, *71*, 289–313.
- (68) Tsukiyama, K.; Bersohn, R. *J. Chem. Phys.* **1986**, *86*, 745–749.
- (69) Giegerich, J.; Fischer, I. *Phys. Chem. Chem. Phys.* **2013**, *15*, 13162–13168.
- (70) Giegerich, J.; Fischer, I. *J. Chem. Phys.* **2015**, *142*, 044304.
- (71) Song, Y.; Zheng, X.; Lucas, M.; Zhang, J. *Phys. Chem. Chem. Phys.* **2011**, *13*, 8296–8305.
- (72) Shapero, M.; Cole-Filipiak, N. C.; Haibach-Morris, C.; Neumark, D. M. *J. Phys. Chem.* **2015**, *119*, 12349–12356.
- (73) Saha, A.; Upadhyaya, H. P.; Kumar, A.; Naik, P. D.; Bajaj, P. N. *Chem. Phys.* **2012**, *402*, 74–82.

4 Photodissociation of the trichloromethyl radical: photofragment imaging and femtosecond photoelectron spectroscopy

Christian T. Matthaehi, Deb Pratim Mukhopadhyay, Anja Röder, Lionel Poisson, and Ingo Fischer

Published: Phys. Chem. Chem. Phys., 2022, 24, 928-940

DOI: 10.1039/D1CP04084G

4.1 Abstract

Halogen-containing radicals play a key role in catalytic reactions leading to stratospheric ozone destruction, thus their photochemistry is of considerable interest. Here we investigate the photodissociation dynamics of the trichloromethyl radical, CCl_3 after excitation in the ultraviolet. While the primary processes directly after light absorption are followed by femtosecond-time resolved photoionisation and photoelectron spectroscopy, the reaction products are monitored by photofragment imaging using nanosecond-lasers. The dominant reaction is loss of a Cl atom, associated with a CCl_2 fragment. However, the detection of Cl atoms is of limited value, because in the pyrolysis CCl_2 is formed as a side product, which in turn dissociates to $\text{CCl} + \text{Cl}$. We therefore additionally monitored the molecular fragments CCl_2 and CCl by photoionisation at 118.2 nm and disentangled the contributions from various processes. A comparison of the CCl images with control experiments on CCl_2 suggest that the dissociation to $\text{CCl} + \text{Cl}_2$ contributes to the photochemistry of CCl_3 .

4.2 Introduction

The photochemistry of halogen-containing species has gained considerable interest since the discovery of their role in the destruction of stratospheric ozone.¹ Numerous alkyl and alkenyl halides, in particular chlorine-substituted have thus been investigated in the gas phase over the years to obtain UV photoabsorption and photodissociation cross sections, but also photodissociation products and branching ratios.²⁻⁹ In contrast, much less is known about open-shell species, i.e. chloroalkyl radicals. Diatomics CX (X = F, Cl, Br, I) have been investigated by high-resolution spectroscopy and their excited states were characterized in detail.^{10,11} The electronic spectroscopy of CCl_2 has been studied in a matrix¹² as well as in the gas phase.^{13,14} The photodissociation of CCl_2 to $\text{CCl} + \text{Cl}$ has been explored by the Dagdigian group using laser-induced fluorescence, who reported both the spin-orbit branching ratio of Cl as well as a bimodal rotational state distribution of CCl ,¹⁵⁻¹⁷ and by Huber and cowork-

ers, who applied photofragment translational spectroscopy.¹⁸ Also the excited states of mixed carbenes CXY were characterized by high resolution electronic spectroscopy.^{19–22} Furthermore, Reisler, Krylov and coworkers investigated the photodissociation of the CH₂Cl radical.^{23,24}

Here we focus on the trichloromethyl radical, CCl₃, which appears as an intermediate in the photodissociation of chloroalkanes and -alkenes in the upper atmosphere,^{25,26} compounds that are involved in stratospheric ozone depletion. The kinetics of the CCl₃ + O₂ reaction has also been monitored because of its relevance in plasma etching.^{27–29} UV absorption and multiphoton ionisation (MPI) yielded information on two-photon excited Rydberg states.³⁰ Danis et al. identified a structureless band with maximum absorption at 210 nm and an absorption cross section $\sigma_{abs} = 14.5$ Mb.³¹ This band was later assigned to the transition from the X²A₁ ground state into the C₂A₁'(3s) Rydberg state.³² Partial resolution of the out-of-plane bending mode and absorption cross sections σ_{abs} at the band heads ranging from 10.2 Mb at 224.8 nm to 1.7 Mb at 250.5 nm were reported, in qualitative agreement with the previous work. An accurate ionisation energy (IE) of 8.06 eV as well as information on the ionic ground state was obtained from a vibrationally resolved photoelectron spectrum.³³ While the neutral ground state is pyramidal (C_{3v}) the ionic ground state is planar (D_{3h}). However, the excited state dynamics has been scarcely explored. The only experimental study of Hintsä et al. used translational energy spectroscopy to explore the photodissociation at 308 nm.³⁴ In this work, only loss of chlorine was found, thus the dominant photodissociation pathway is CCl₃ → CCl₂ + Cl. Hintsä et al. reported an average translational energy release of 13 kcal mol⁻¹ (54 kJ mol⁻¹) and an anisotropy parameter $\beta \approx 1 \pm 0.2$. Computationally, the neutral and ionic ground state have been investigated,^{33,35} but information available on the excited electronic states is limited to low-level methods like Hartree-Fock.³⁰ In order to obtain a full picture of the excited state dynamics of CCl₃, we initiated a study that combines femtosecond-time resolved photoionisation and photoelectron spectroscopy (TR-PES)^{36–38} to explore the initial processes following photoexcitation with nanosecond photofragment imaging^{39,40} to monitor the photodissociation products. The latter approach has evolved into a method that provides detailed insight into the photodissociation mechanism of stable molecules^{40–42} and radicals⁴³ by monitoring the translational energy release of photofragments. In the past, we applied the method to investigate H-atom loss from radicals,⁴⁴ biradicals⁴⁵ and carbenes,⁴⁶ but recently extended our work to chlorine-containing molecules.⁴⁷ Experiments are accompanied by computations using time-dependent density functional theory (TD-DFT).

4.3 Experimental

CCl_3 was generated by flash pyrolysis either from CCl_3Br or from CCl_4 . In addition, CHCl_3 (chloroform) was employed for control experiments on CCl_2 . All precursors were commercially obtained from Sigma-Aldrich, seeded in around 1.5-2 bar of Ar and thermally cleaved in an electrically heated SiC tube, mounted on a solenoid pulsed valve. In the subsequent adiabatic expansion, the radicals are typically cooled to vibrational temperatures of 150 K, as concluded from previous work.⁴⁵

In both, the femtosecond (fs-) time resolved experiments and the nanosecond (ns-) photofragment detection, the velocity map imaging (VMI) technique was applied.^{39,40} Fs-time resolved experiments were conducted at the LUCA/S-LIC laser facility. Photoelectron images (PEI) were recorded and yielded the TR-PES. Experimental conditions were similar to previous experiments.^{48,49} Briefly, the tripled fundamental of the Ti:Sa laser around 266 nm (10-50 mJ) was used as the pump pulse, for the probe pulse the fundamental of the Ti:Sa laser (798 nm, 0.1-0.7 mJ) was employed. For the time-resolved mass spectra six scans were averaged, for the photoelectron images seven scans. Within one scan the ion signal as well as the PE images were integrated over 150 laser shots. As no dependence on the relative polarization of the pump and probe pulses was observed, the rotational mean is discussed in the experimental spectra. The one-colour background signal was subtracted from the delay traces. The ns-experiments were conducted at the University of Würzburg, using a photofragment imaging setup.^{44,47} A skimmed free molecular jet enters the time of flight mass spectrometer (TOF-MS), which can be operated in either space-focusing or VMI configuration. Two separate counterpropagating ns-laser systems were used to dissociate and ionize the fragments. For photodissociation, the unfocused frequency-doubled output of a Nd:YAG laser pumped dye laser (230-250 nm/5.39-4.96 eV) with 0.5-1.0 mJ per pulse was used, polarized parallel to the detector plane. For ionisation we either employed the 9th harmonic of a Nd-YAG laser at 118.2 nm for the molecular fragments or a second tuneable dye laser system for ionisation of Cl atoms in a [1 + 1'] resonance-enhanced MPI process. In the latter, the $^2\text{D}_{5/2} \leftarrow ^2\text{P}_{3/2}^{\text{O}}$ transition of Cl was excited by 118.9 nm radiation, produced by frequency tripling the second harmonic output of a second dye laser system in Xe. Note that the spin-orbit excited $^2\text{P}_{1/2}$ state of Cl cannot be probed by this scheme, as discussed previously, because there is no suitable transition in the tripling range accessible with the setup.⁴⁷ For these experiments, the dye laser was scanned over the entire Doppler profile of the atomic transition. The residual 356.7 nm light was employed for the ionisation step.⁴⁷ The velocity map images were accumulated over 10^4 laser shots and one-colour background was subtracted. Mass spectra were recorded by monitoring the current generated upon ion im-

pect on the MCPs. Further details on the ion optics, the imaging detector and the laser systems are given in the SI.

In both fs-PEI and ns-photofragment imaging, the 3D Newton sphere was reconstructed from the image via inverse Abel transformation with the pBASEX algorithm, employing Legendre polynomials up to the 4th order.⁵⁰ From this reconstruction, the photoelectron spectra (fs-experiments) and the translational energy release distributions $P(E_T)$ (ns-experiments) were derived.

Calculations were performed using DFT (density functional theory) employing the Qchem4 package, the CAM-B3LYP functional and the aug-cc-pVTZ basis set.⁵¹ Excited states were calculated using TD-DFT, also employing the CAM-B3LYP functional and the aug-cc-pVTZ basis set. TD-DFT is rather simple and inexpensive method that nevertheless yields reasonably accurate vertical excitation energies for many radicals.⁵² Spin contamination can be problematic, but were negligible in the computations presented below. For all calculated states, S^2 was around 0.8 at most, with a nominal value of 0.75.

4.4 Results

4.4.1 Calculations

The CCl_3 radical is C_{3v} -symmetric with a X^2A_1 electronic ground state. For the optimized ground state structure, we find a C-Cl bond length $R_{C-Cl} = 1.708\text{\AA}$, and angles $\alpha_{Cl-C-Cl} = 117.31^\circ$ and $d_{Cl-C-Cl-Cl} = -148.0^\circ$, in agreement with previous work.³³ The singly occupied molecular orbital (SOMO) can be seen in a first approximation as a p-orbital centred at the carbon atom, with contributions from the non-bonding orbitals at the chlorine. The relevant excited states, as well as vertical excitation energies and oscillator strengths for transitions from the ground state, as well as an approximate character of the transition are given in Table 4.1.

Table 4.1: Vertical excitation energies (at the ground state minimum geometry) and oscillator strengths f , computed by TD-DFT

State	$E_{\text{vert}}/\text{eV}$	Osc. Strength f	Attribution
2^2A_1	3.80	9.1×10^{-5}	SOMO \rightarrow LUMO, (C-Cl antibonding)
1^2A_2	4.96	0	$n_{Cl} \rightarrow$ SOMO
1^2E	5.41	4.1×10^{-5}	SOMO \rightarrow 3p-Rydberg/HOMO-2 \rightarrow SOMO
2^2E	5.69	4.2×10^{-2}	HOMO-2 \rightarrow SOMO
3^2A_1	5.74	1.3×10^{-2}	SOMO \rightarrow 3s-Rydberg

The transition into the lowest-lying excited state is centred in the near UV at 3.80 eV, corresponding to 326 nm. With an oscillator strength f around

10^{-4} it is expected to be rather weak. The second excited state is of A_2 symmetry, thus transitions from the ground state are dipole-forbidden. Above 5 eV a number of close-lying excited states are computed, two of them with considerable Rydberg character. Due to their energetic proximity the states are expected to be strongly coupled. Transitions into the $1\ ^2E$ state are again expected to be rather weak. The next states, the $2\ ^2E$ and the $3\ ^2A_1$ (3s) state are associated with $f = 0.1 - 0.01$ and thus provide the absorption strength for excitation in the far-UV. In previous work an absorption band was observed that sets in around 270 nm and maximises at 210 nm, corresponding to $E_{\text{vert}} = 5.90$ eV. It has been assigned to the $3\ ^2A_1$ (3s) state ($^2A'_1$ in D_{3h}).³² The computed transition dipole moment μ_T is oriented along the symmetry axis of the radical. Based on our computations, the $2\ ^2E$ will also contribute to this band. Here, μ_T is perpendicular to the symmetry axis. From a comparison with the experimental work we conclude that the computed E_{vert} are accurate to within ± 0.2 eV.

4.4.2 Mass spectra

Figure 4.1(a) shows the two-colour photoionisation mass spectrum (PIMS) of pyrolysed CCl_4 with 230 nm excitation and 118.2 nm ionisation (black line). Note that CCl_4 has an IE of 11.47 eV, thus no signal was observed without pyrolysis. A power of 40 W was applied to the SiC tube, corresponding to roughly 700-800 K. The main pyrolysis product is CCl_3 ($m/z = 117-123$), contributions from CCl_2 (m/z 82-86) and CCl (47, 49) are also identified. Minute amounts of C_2Cl_2 (m/z 94-98), C_2Cl_3 (m/z 129-135) and C_2Cl_4 (m/z 164-172) can also be observed. Close ups of the relevant contributions CCl , CCl_2 and CCl_3 are shown in Figure 4.1(b)-(d). The red and blue curves represent the signals with only ionisation or dissociation laser present. Upon turning the dissociation laser on, the CCl and CCl_2 signals increases roughly by a factor of two (black curve), indicating that they are formed in the dissociation, while the CCl_3 signal stays constant within the accuracy of the experiment. Also, one-colour ionisation of CCl by the 230 nm radiation is visible. Due to the delay between the two lasers, the peak appears at earlier time-of-flight, corresponding to m/z 38 and 40 for the two-colour signal. PIMS were also recorded at 235 nm, 240 nm, 245 nm and 250 nm. In agreement with the reported absorption cross section of CCl_3 the two-colour signal decreases with increasing wavelength.³² Mass spectra using chloroform as a precursor are given in Figure 4.S1 in the SI. As expected from previous work, they show CCl_2 to be the dominant pyrolysis product.^{17,53} Typical mass spectra obtained in the femtosecond experiments using CCl_3Br with pyrolysis present (black line) and without pyrolysis (red line) are given in Figure 4.2. They were recorded with pump- and probe-laser present at around time zero. While the mass spectrum without pyrolysis shows no appreciable signal at all, an intense signal corresponding to CCl_3 appears

with active pyrolysis. Small mass peaks due to Br (m/z 79/81) and CCl_2 as well as C_2Cl_4 (m/z 164-172) are visible. Mass spectra with pump- and probe-laser only revealed a one-colour background signal that was at least a factor of ten smaller than the pump-probe signal. Note that we stopped using CCl_3Br in the ns-experiments, because the presence of several mixed radicals CCl_xBr that were efficiently excited at shorter wavelengths complicated data interpretation.

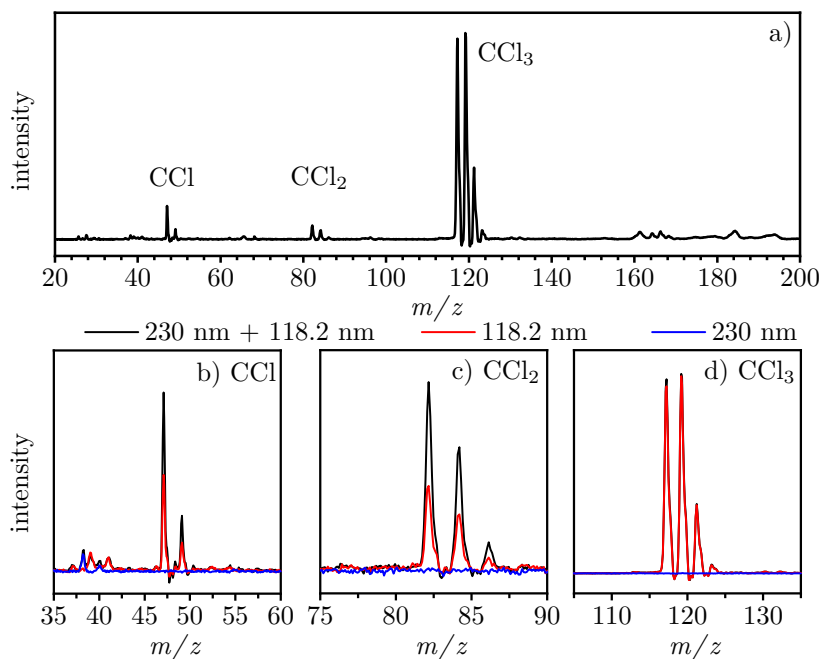


Figure 4.1: In (a) the two-colour mass spectrum using CCl_4 as a precursor recorded with 230 nm dissociation and a 118.2 nm ionisation wavelength is shown. Below, close-ups of the (b) CCl , (c) CCl_2 and (d) CCl_3 mass signals are displayed. In red the signal generated by only the ionisation laser and in blue by only the dissociation laser are shown. As visible, CCl and CCl_2 signals increase in the two-colour process. For CCl , a one-colour signal caused by the 230 nm radiation alone is present. Due to the delay between the two lasers it appears in the same region as the two-colour signals of m/z 38 and 40.

4.4.3 Time-resolved experiments

To investigate the primary photophysical processes in CCl_3 directly after excitation we conducted fs-time-resolved experiments, using ion and photoelectron detection. In Figure 4.3 the time-resolved ion signal is depicted. The CCl_3 sig-

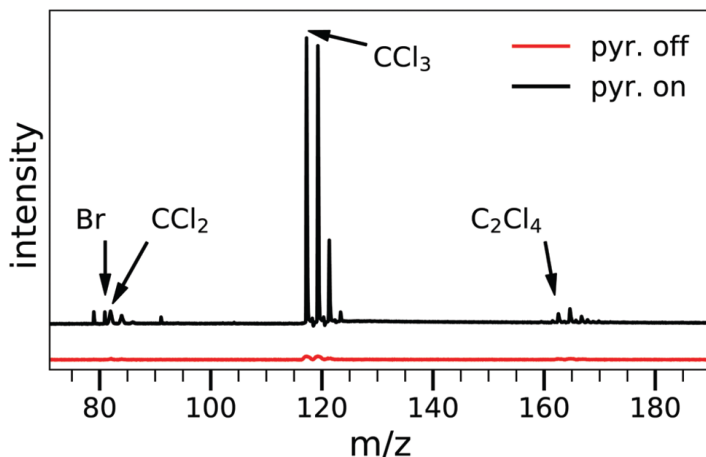


Figure 4.2: Mass spectra with and without pyrolysis, recorded with fs-lasers, $\lambda_{\text{pump}} = 266$ nm and $\lambda_{\text{probe}} = 798$ nm around time zero. CCl_3Br was employed as a precursor.

nal (open circles) decays quickly and a monoexponential fit (green line) yields a time constant of 50 ± 20 fs. The instrument response function (IRF) of 118 ± 10 fs employed in the fit is given as a dashed red line for comparison and shows that despite the short lifetime a reliable time constant can be extracted. At longer delay times the fit consistently underestimates the signal intensity, which indicates the presence of a second time constant on the order of 100-150 fs. However, an accurate value cannot be determined, because the contribution to the signal is too low.

As discussed above, TR-PES provides additional information not available from the mass spectra, albeit at the cost of losing mass information. Thus, possible side products from the pyrolysis have to be considered. We therefore included the time-dependent ion signal of the most relevant side product CCl_2 in Figure 4.3 (open diamonds). The signal was multiplied by a factor of six for a better comparison. As visible, the signal deviates only slightly from the IRF, thus the lifetime is significantly shorter than 50 fs. In addition, the signal has disappeared beyond 150 fs.

In Figure 4.4 the time-resolved photoelectron spectrum is displayed as 2D map. Although CCl_3 dominates the mass spectrum (Figure 4.2), small contributions from side products are present and have to be taken into account. At an electron kinetic energy (eKE) of 0.5 eV (left-hand panel) a time-dependent signal without observable decay is visible. Note that the trace for $t > 0.2$ ps has been scaled for ease of viewing. An ion signal with the same time-dependence is

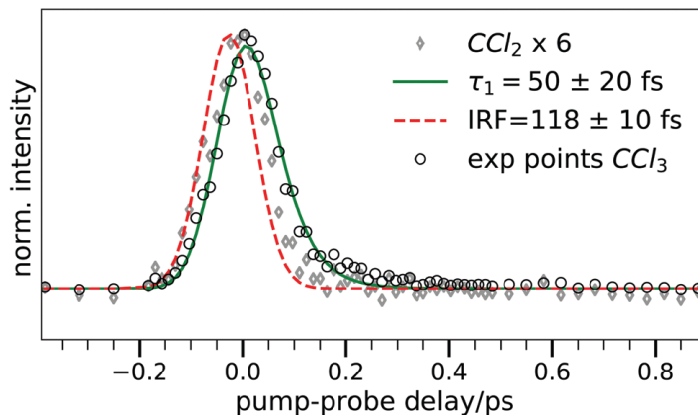


Figure 4.3: The time-resolved ion signal of CCl_3 (open circles) at 266 nm excitation is fitted by a monoexponential decay with a time constant of 50 fs. As visible, the fit underestimates the signal intensity beyond 200 fs, indicating the presence of a second contribution. For comparison, the CCl_2 signal (signal multiplied by six for ease of viewing) and the instrument response function (dashed red line) are given.

observed for Br (see Figure 4.S2, SI), therefore we assign the signal to bromine atoms formed in the pyrolysis.¹ The photoelectron signal from CCl_3 itself starts at around 1 eV, trailing to lower kinetic energies. Taking the IE of 8.06 eV into account,³³ the eKE confirms ionisation in a $[1+3']$ process with a total photon energy of around 9.32 eV. Two-photon excitation in the pump step can thus be excluded based on the energetics. Thus we are certain that the UV-absorption band reported by Ellermann is indeed excited, although 266 nm is close to the red edge of the band.³² The shoulder to lower eKE represents transitions into vibrationally excited states of the ion that cannot be resolved due to the laser bandwidth. The vibrational envelope appears due to the large geometry change upon ionisation. A very small signal at 2.3 eV represents an $[1+4']$ ionisation contribution. For CCl_2 an IE of 9.27 eV was determined,⁵³ thus only transitions with low eKE are expected. Indeed, a peak close to 0 eV and only present around t_0 can be recognized in the 2D map. We therefore assume, that the electron signal above 0.7 eV does only contain contributions from CCl_3 . The time-delay traces above the 2D map show the electron signal averaged over two eKE ranges (blue and red lines). The top one (0.7-1.2 eV, red line) is indeed almost identical to the CCl_3 ion signal and yields the same time constant. The lower trace, averaged over the kinetic energies from 0.38

¹Bromine has an IE of 11.81 eV. Ionisation via a $[1+5']$ or $[2+2']$ process with a total energy of 12.41 eV would be in agreement with $\text{eKE} \approx 0.5$ eV, assuming a non-perfect energy calibration. However, an alternative origin might be the dissociative photoionisation of Br_2 formed in the pyrolysis reactor in a $[1+4']$ process, $\text{AE}(\text{Br}^+, \text{Br}_2) = 10.48$ eV.

to 0.7 eV (blue line) contains contributions from Br and is offset at late times compared to the ion signal due to the resonant ionisation of bromine atoms.

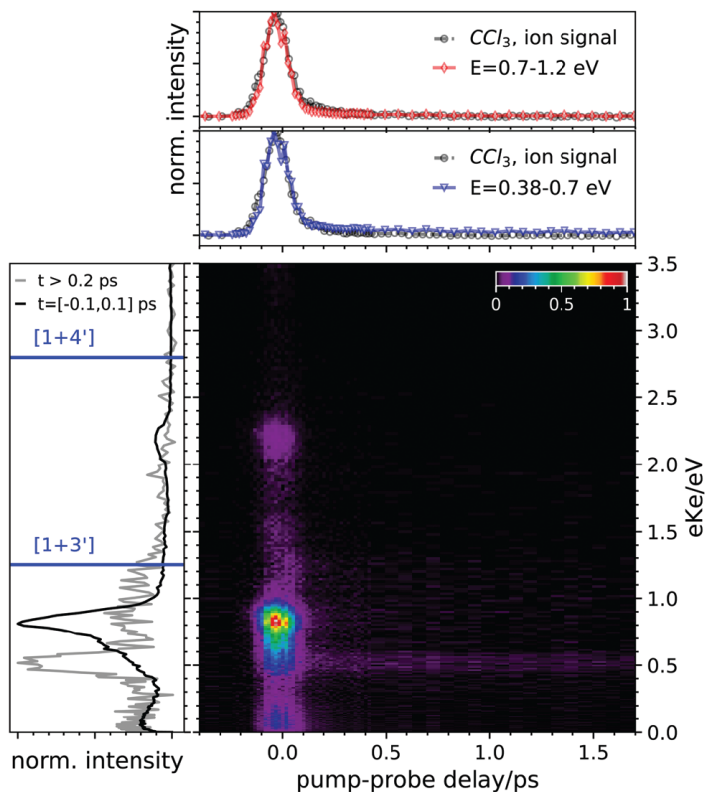


Figure 4.4: TR-PES spectrum with 266 nm pump/798 nm probe, displayed as a 2D-map. In the top trace the time-dependence of the photoelectron signal at two selected energy ranges is depicted and compared to the decay trace of CCl_3 ion signal obtained from the mass spectra (grey open circles). The graph on the left shows the photoelectron kinetic energy summed over all delay times. The trace for $t > 0.2$ ps has been scaled for ease of viewing. The average signal collected before t_0 was subtracted from the whole signal.

4.4.4 Nanosecond photofragment imaging

Photofragment imaging of CCl_3 photodissociation.

In the next step, the UV photodissociation of CCl_3 has been investigated between 230 nm ($520.1 \text{ kJ mol}^{-1}/5.39 \text{ eV}$) and 250 nm ($478.5 \text{ kJ mol}^{-1}/4.96 \text{ eV}$). In this region, two product channels are accessible, loss of a Cl atom (4.I) and

loss of Cl_2 (4.II). The reaction pathways are depicted in Figure 4.5. Note that CCl_2 can be formed in its singlet ground state or the first excited triplet state.



Both (4.Ia) and (4.Ib) can also be formed in conjunction with the spin-orbit excited ${}^2\text{P}_{1/2}$ state of Cl (+0.109 eV/10.52 kJ mol⁻¹). The first excited (open-shell) singlet state is at +17265 cm⁻¹ above the ground state (+206 kJ mol⁻¹) and thus barely accessible at the highest excitation energies.¹³ It is therefore neglected in the analysis below.

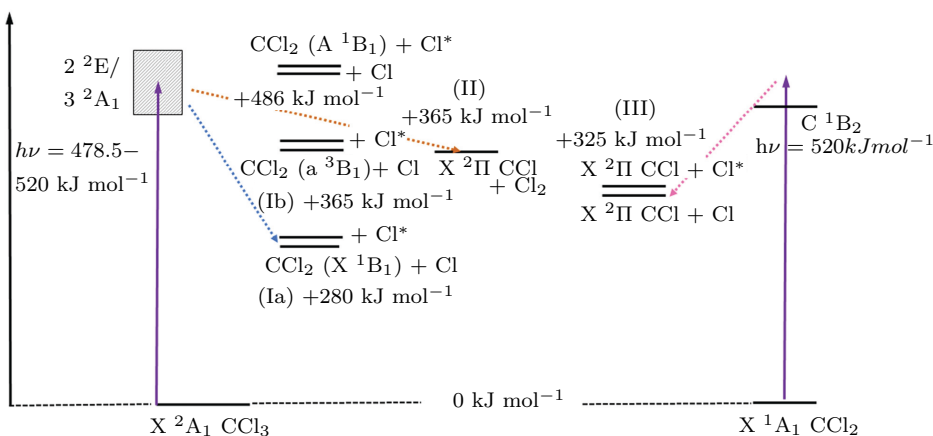


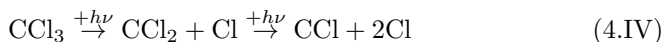
Figure 4.5: Summary of the relevant dissociation pathways in CCl_3 (left-hand side) and CCl_2 (right-hand side). The major product of CCl_3 photodissociation is dichlorocarbene in its X^1A_1 ground state (blue line). Loss of Cl_2 seems to be present as well (brown line). CCl_2 is also formed in the pyrolysis and dissociates to $\text{CCl}+\text{Cl}$ (magenta line).

Heats of reaction were computed from data given in the Active Thermochemical Tables (ATcT).^{54,55} For comparison, we computed $\Delta_R H^0(0 \text{ K}) = 278 \text{ kJ mol}^{-1}$ for (4.Ia). We assume that only a negligible reverse barrier is present, so $\Delta_R H^0$ is approximated to the bond dissociation energy, BDE. Formation of CCl in conjunction with two chlorine atoms is thermochemically not possible upon one-photon excitation. Nevertheless, photodissociation of CCl_2 has to be considered in the analysis, because it is produced as a further pyrolysis product

(see Figure 4.1 and Figure 4.5) and dissociates after single photon absorption (4.III).

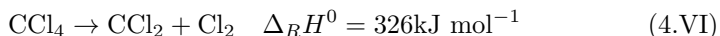


Alternatively, CCl_2 generated in the photodissociation of CCl_3 can dissociate after absorption of a second photon (4.IV), corresponding to two-photon dissociation of CCl_3 .



Note that CCl_2 (photo) generated in (Ia) or (Ib) will store part of the excess energy in the vibrational and rotational degrees of freedom, whereas CCl_2 (pyro) will be cooled in the jet expansion.

The CCl_4 precursor can also lose Cl or Cl_2 , but the tabulate absorption cross sections at 298 K lie between 0.02 Mb at 230 nm and 10^{-3} Mb at 250 nm, two to three orders of magnitude smaller than those of CCl_3 .⁵⁶ Indeed, we did not observe any photodissociation from pure CCl_4 without pyrolysis. Nevertheless, vibrational excitation acquired in the pyrolysis might increase the photodissociation cross section. It should also be kept in mind that CCl_4 is not observable in the mass spectrum and the pyrolytic conversion is thus unclear. Therefore, we will consider its thermochemistry as well.



While most experiments on CCl_4 were conducted in the VUV range, Kawasaki et al. investigated the photodissociation in a one-colour experiment at 235 nm (509kJ mol^{-1}) and found a Cl/Cl* ratio of 8/2, with a Boltzmann-type distribution for Cl.⁵⁷ However, the large translational energy release of the Cl* atoms that extends to more than 40kcal mol^{-1} (167kJ mol^{-1}) indicates the presence of a contribution from multiphoton excitation. For (4.VI) a quantum yield of only 5% was found at 214 nm,⁵⁸ compared with 490% for (4.V), with its relative importance increasing towards higher excitation energies (i.e. decreasing to longer wavelengths).

In general, an image of the atomic fragment of a photodissociation, in this case Cl, is simpler and easier to interpret. However, from the presence of Cl in (4.I), (4.III), (4.IV) and possibly (4.V) a superposition of several contributions is expected, and the additional detection of the molecular fragment is required. Therefore, in a first series of experiments, images of the CCl_2 photoproduct

ionized at 118.2 nm were recorded. Due to the subtraction of one-colour background signals, CCl_2 generated in the pyrolysis does not contribute to the image. Formation of CCl_2 from CCl_4 via (4.VI) is neglected, due to the small quantum yield observed at 214 nm and the even lower one expected at 230 nm. Translational energy distributions $P(E_T)$ probing CCl_2 upon 230 nm (upper trace, blue) and 250 nm excitation (lower trace, red) are given in Figure 4.6. The reconstructed image is visible on the right hand side. Experiments were also performed at 235 nm, 240 nm and 245 nm under the same conditions, the data are displayed in Figure 4.S4 (SI). Note that throughout the paper we plot ET of the respective fragment rather than the total translational energy release, because in the analysis, contributions from several molecules have to be included and compared. Excitation at 266 nm was also used for better comparison with the fs-data, but the photofragment signals beyond 250 nm were small and difficult to separate from the background signals.

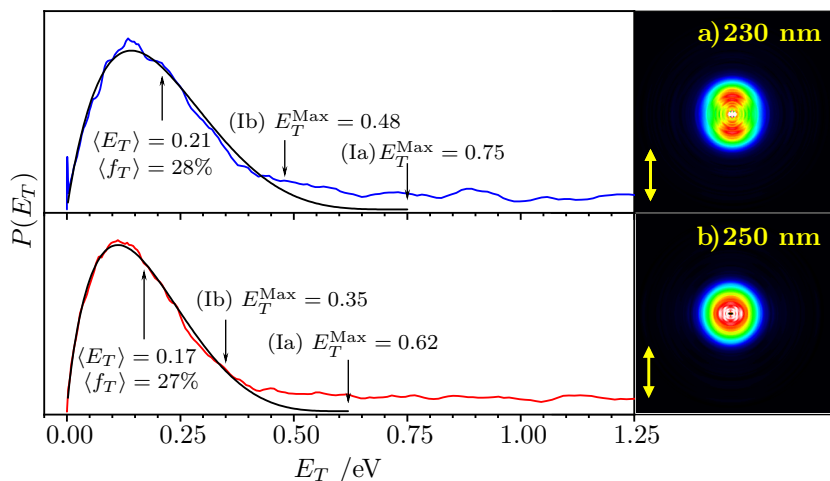


Figure 4.6: Translational energy distribution $P(E_T)$ of the CCl_2 fragment upon excitation with (a) 230 nm and (b) 250 nm light. The experimental results are drawn in blue and red respectively and a fit using expression (4.1) in black. The corresponding velocity map images are shown with a yellow arrow indicating the laser polarisation. Note that only the translational energy of the CCl_2 fragment is plotted on the abscissa. $\langle E_T \rangle_{\text{total}}$ amounts to 0.70 eV at 230 nm and 0.57 eV at 250 nm.

A unimodal energy distribution is observed with a shape that is independent of the dissociation wavelength. At both wavelengths, a background is visible that extends over all translational energies. The images on the right-hand side show a small anisotropy in the fragment distribution, which indicates a fast dissociation in less than a rotational period. The photofragment angular

distributions (PAD) are given in Figure 4.S6 (SI). From the PAD a value for the anisotropy parameter β of 0.5, is extracted at 230 nm, which decreases to around $\beta = 0.06$ at 250 nm.

As in previous work an empirical two-parameter function was used to fit the experimental data and extract the expectation value for the translational energy release, $\langle E_T \rangle$.^{59–61}

$$P(E_T) = C(E_T)^a (E_T^{\max} - E_T)^b \quad (4.1)$$

Here C is a normalisation constant, a and b are the two fitting constants and E_T^{\max} is the maximum available translational energy for the fragment upon photodissociation, computed from (4.2) and indicated by arrows in the figure.

$$E_T^{\max}(A) = \frac{m_B}{m_{A-B}}(h\nu - BDE) \quad (4.2)$$

This fit is used for extracting the expectation value from the recorded data. As an example, fitting the experimental data at a dissociation wavelength of 230 nm with the two-parameter fit results in an expectation value for the fraction of excess energy released as translation, $f_T = E_T/E_T^{\max} = 28\%$, assuming channel (4.Ia), i.e. formation of CCl_2 in its electronic ground state. As visible in particular for 250 nm (lower trace), $P(E_T)$ extends beyond the cut-off expected for formation of CCl_2 in the excited triplet state, so (4.Ib) is considered to be of minor importance. Note that the spin-orbit splitting in Cl is 881 cm^{-1} (0.109 eV) and cannot be resolved in the data. Also product vibrations are not resolved. A summary of the values obtained at the various dissociation wavelengths is shown in Table 4.2.

Table 4.2: Experimental values for the CCl_2 fragments from CCl_3 photodissociation

$\lambda_{\text{diss}}/\text{nm}$	$E_T^{\max}(\text{CCl}_2)/\text{eV}$	E_T/eV	$\langle f \rangle/\%$	β
230	0.75	0.21	28	0.50
235	0.72	0.19	26	0.20
240	0.68	0.19	28	0.13
245	0.65	0.19	29	0.05
250	0.62	0.17	27	0.06

The anisotropic photofragment angular distribution indicates a dissociation that proceeds faster than a rotational period, i.e. along a repulsive or predissociative coordinate. The expectation value of such a direct dissociation can be calculated with an impulsive model described by Tuck⁶² and by Galloway et al.⁶³ It is based on the assumption that the available energy goes initially into the translation of Cl and C, which are considered independent from the rest of the molecule. Only after the dissociation this energy is redistributed in

the molecular fragment. This simple model is appropriate for a direct dissociation, which is faster than energy redistribution in the molecule. The impulsive model yields an expectation value $\langle f_T \rangle = 36\%$ for the total translational energy release. Considering that the geometry change in the molecular fragment during dissociation is neglected, the agreement with the experimental value is reasonable. It has been shown that impulsive (i.e. direct) C-Cl bond rupture will lead to a significant part of the excess energy ending up as CCl_2 rotation.³⁴

As visible in Figure 4.6, there is a contribution at higher translational energies that extends beyond E_T^{max} and does not originate from channel (4.I). It is either the result of a background signal that could not be fully subtracted, from the dissociation of one of the higher masses visible in the mass spectrum, or from a small multiphoton contribution that is present, although a low laser power was used and the beam was not focused.

The second pathway (4.II) for photodissociation of CCl_3 leads to $\text{CCl} + \text{Cl}_2$, therefore velocity map images of CCl were also recorded. However, as noted above CCl can also be formed from CCl_2 via (4.III) or (4.IV). Figure 4.7 shows $P(E_T)$ for (a) 230 nm and (b) 250 nm (black curve). Data at further wavelengths are given in Figure 4.S5 (SI). Note again that E_T of the CCl fragment is plotted on the x-axis rather than the total translational energy release, because contributions from two different molecules (CCl_2 and CCl_3) have to be considered. A bi- or multimodal distribution is evident from the shape. The contributions to the fit will be discussed below. At 250 nm excitation, the distribution maximizes around 0.1 eV, followed by a shoulder at around 0.4 eV. Furthermore, a background signal is again present, which extends to high translational energies. Anisotropy is evident at 230 nm, but less pronounced at 250 nm. The energy cut-offs for the various product channels are indicated by arrows. As visible, $P(E_T)$ extends beyond the limit given by reactions (4.II) and (4.III). E_T^{max} for the CCl fragment after dissociation with 230 nm light for reaction (4.III) is 0.87 eV, for reaction (4.II) 0.98 eV and for the consecutive two-photon process (4.IV) 2.24 eV. We thus conclude that the latter process (4.IV) is responsible for this contribution at large E_T . The maximum possible ET values at the various excitation wavelengths are summarised in the SI, Table 4.S1.

Photofragment imaging of CCl_2 photodissociation.

To get information on the possible presence of (4.II) to the $P(E_T)$ of CCl , we conducted experiments using CHCl_3 as a precursor, which is known to produce predominately CCl_2 upon pyrolysis (see mass spectra in Figure 4.S1, SI). Figure 4.8 shows the velocity map image of the CCl fragment after dissociation of CCl_2 with 230 nm light. Two contributions are discernible, an isotropic first one at low energies (around 0.1 eV) and a second one centred at around 0.4 eV, which is strongly anisotropic. Interestingly, the high energy component visible in Figure 4.7 is absent, supporting its assignment to (IV). Experimental con-

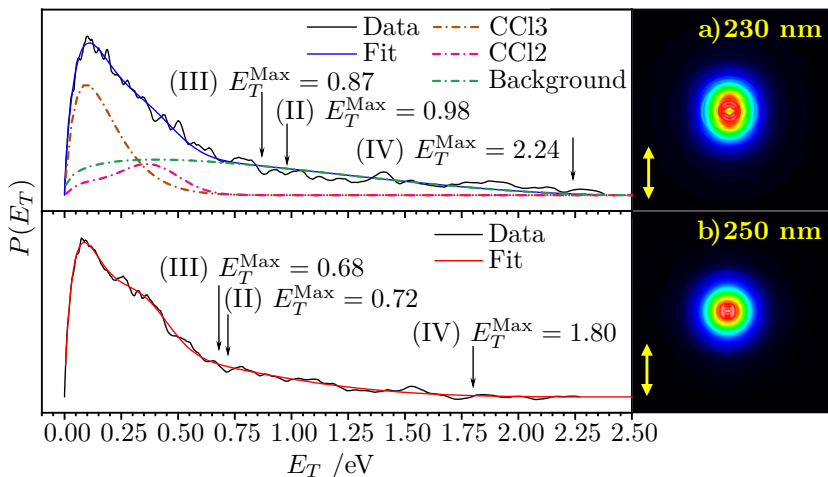


Figure 4.7: Translational energy distribution $P(E_T)$ of the CCl fragment using CCl_4 as a precursor. In (a) 230 nm and in (b) 250 nm light was used for dissociation. The experimental results are shown in black, while fits are shown in blue or red. In the upper trace the fit to the CCl_2 data obtained from Figure 4.8 (see below) is given as a dotted magenta line, assumed contributions from CCl_3 are given as a dashed brown line, while multiphoton contributions are given in green. The corresponding Velocity Map Images are shown with a yellow arrow indicating the laser polarisation. Again the translational energy of the CCl fragment is plotted on the abscissa, because $P(E_T)$ contains contributions from the photodissociation of CCl_3 and CCl_2 . The red line in the bottom trace assumes similar components (scaled) at 250 nm.

ditions (mainly pyrolysis power) were varied in order to increase and decrease the amount of CCl_3 generated as a side product and additional VMIs were recorded. However, the two contributions in the CCl image did not change appreciably when the experimental conditions were changed. This confirms that both contributions belong to the dissociation of CCl_2 . Its photodissociation dynamics has been investigated in detail by Dagdigian and co-workers, who monitored the CCl fragment by laser induced fluorescence,^{15–17} and by Huber and coworkers, who employed photofragment translational spectroscopy (PTS).¹⁸ The Dagdigian-group observed two different dissociation channels associated with different rotational state distributions of CCl. Thus, the two contributions obtained from the images are in qualitative agreement with this previous work. The isotropic contribution at low E_T in Figure 4.8 (dashed green line) is assumed to originate from a statistical process and a fit using function (4.1) yields $\langle E_T \rangle = 0.15$ eV, corresponding to $\langle f_T \rangle = 17\%$. The high-energy contribution (dotted magenta line) is fitted by a Gaussian centred around $\langle E_T \rangle = 0.37$ eV. Given that $E_T^{\text{max}} = 0.87$ eV, as indicated by the ar-

row in Figure 4.8, this corresponds to $\langle f_T \rangle = 43\%$ released into translation of the CCl fragment. Taking the translational energy of the Cl counterfragment into account, an expectation value for the total translational energy release $\langle E_T \rangle_{\text{tot}} = 0.89$ eV (86 kJ mol^{-1}) is obtained. This process is associated with a β -value close to 1. Note that a more detailed study on the photodissociation dynamics of CCl_2 is currently underway. PTS at 248 nm yielded a comparable value of $\langle E_T \rangle_{\text{tot}} \approx 100 \text{ kJ mol}^{-1}$, corresponding to roughly 1 eV, but only a negligible anisotropy was observed.¹⁸

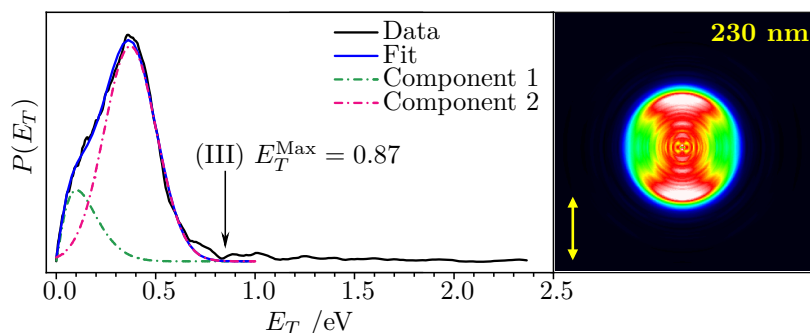


Figure 4.8: Translational energy distribution $P(E_T)$ of CCl using CHCl_3 as a precursor and dissociating at 230 nm. The experimental results are shown in black, while a superposition of a two-parameter fit (expression (4.1)) and a Gaussian distribution is shown in blue. The individual functions are drawn in dashed lines. The corresponding velocity map images are shown with an arrow indicating the laser polarisation in yellow.

Going back to the photodissociation of CCl_3 in Figure 4.7, it is evident that the shoulder in trace (b) at around 0.4 eV is due to the anisotropic component observed in reaction (4.III) for the photodissociation of CCl_2 (dotted magenta line). However, the low energy contribution is significantly more intense in Figure 4.7 than in Figure 4.8. Concluding from the contribution at large E_T , part of the signal at all E_T will be due to (4.IV), indicated as a dash-dotted green line, but there seems to be an additional component that appears exclusively at low E_T (dashed brown line). It suggests that reaction (4.II) occurs in CCl_3 as an additional contribution. The fit in the upper trace of Figure 4.7 (full blue line) contains the various contributions. Note that due to the large number of free parameters, this fit represents only an approximation and should be considered with care. This is particularly true for the fit at 250 nm (red line), which employs a scaled CCl_2 distribution. As (4.II) is associated with Cl_2 formation, we also attempted to detect molecular chlorine via the REMPI line at 118.94 nm,⁶⁴ but were unsuccessful. This in turn seems to indicate that reac-

tion (4.II) is of minor importance. However, it is hard to detect photofragments when the oscillator strength is distributed over a large number of transitions.

Chlorine images.

Further information on the dissociation dynamics should be available from the atomic fragment. Due to the large absorption cross section of CCl_3 at 230 nm, it is not possible to monitor Cl-atoms via [2 + 1] REMPI at 235 nm, because the focussing conditions cause multiphoton excitation of the radical. On the other hand, a [3 + 1] process at 356.7 nm did not yield analysable Cl images. As in previous work, we therefore resorted to ionisation of atomic Cl in a [1 + 1] process via the ${}^2\text{D}_{5/2} \rightarrow {}^2\text{P}_{3/2}^{\text{O}}$ transition, using VUV excitation at 118.9 nm.⁴⁷ A velocity map image of the atomic chlorine ${}^2\text{P}_{3/2}$ fragment was recorded at a dissociation wavelength of 230 nm, using pyrolysis of CCl_4 . It is given in Figure 4.S7 (SISI). As noted above, the spin-orbit excited ${}^2\text{P}_{1/2}$ state of Cl cannot be probed by this scheme. If the Cl atom and the CCl_2 fragment originate from the same process, the momenta calculated from the translational energy distributions of the two fragments should be matched with each other. The blue line in Figure 4.9 represents the expected Cl distribution momentum-matched with the CCl_2 distribution given in the upper trace of Figure 4.6, corresponding to reaction (4.I). As visible the maxima overlap quite well, indicating that the major part of the Cl atoms originates from process (4.Ia). However, the width of the distribution does not match and deviations at low and high momentum indicate that other processes contribute to the Cl-signal. Figure 4.S8 (SI) illustrates P_2 as a function of momentum for CCl_2 and Cl. As visible, both follow the same trend, but for chlorine, P_2 is less pronounced and even becomes negative at momenta larger 1×10^{-22} N s. This confirms the existence of a further contribution at higher momenta that is not associated with photodissociation of CCl_3 . The Cl distribution expected from reaction (4.III) is given as a red line in Figure 4.9. It should be rather narrow and centred at a slightly higher momentum, therefore it can only partially explain the deviations in the distribution. Thus fragments produced from CCl_3 after multiphoton excitation via (4.IV) as well as chlorine-fragments from (4.V) might contribute to the Cl signal over a range of translational energies or momenta, respectively.

4.5 Discussion

A model of the photodynamics of CCl_3 can be derived by combining the information from fs time-resolved PES with the information on the dissociation products, available from photofragment imaging with ns-lasers. While the former gives insight into the processes directly after excitation, the latter sheds light on the later steps of the photochemistry. It is important to keep in mind that CCl_3 is a rather complicated radical with a number of low-lying electronic

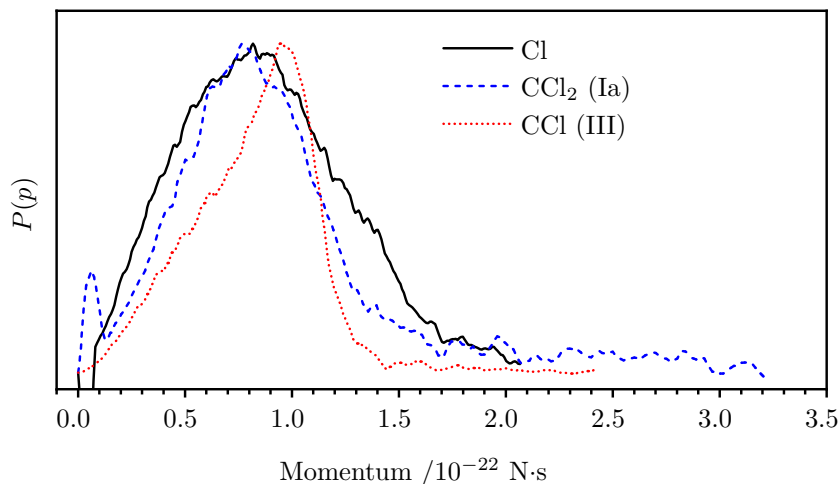


Figure 4.9: Translational energy distribution of atomic Cl (black) as a function of momentum, recorded at 230 nm. The blue dashed line shows the distribution expected from momentum-matching of the CCl_2 signal. The red dotted line indicates the momentum matching expected for a CCl co-fragment from the photodissociation of CCl_2 (III). As visible, the Cl and CCl fragments do not match well.

states that has only scarcely been investigated. The description will therefore be less detailed than the one possible for diatomics or simple hydrocarbons.

In all experiments, the UV absorption band starting around 270 nm and previously observed by Ellerman is excited. As evident from Table 4.1, the 1^2E , 2^2E and the 3^2A_1 (3s) states lie close to each other and based on their computed oscillator strengths the latter two will contribute to this band, which has previously been assigned as 3^2A_1 (3s). The electron kinetic energy in the TR-PES (*cf.* Figure 4.4) shows that single photon excitation dominates and that the red edge of the absorption band is excited. The excitation energy will be rapidly redistributed between these electronic states. The time constant of around 50 fs observed in the time-resolved spectra reflects the redistribution of energy and subsequent motion out of the Franck-Condon region. Furthermore, we expect rapid depopulation of the higher excited state and transfer of the molecule to the lower-lying states, most likely 2^2A_1 and 1^2A_2 . Based on the data available for alkyl halides like CH_3Cl ,^{6,65} and preliminary computations, these lower lying states are expected to be repulsive with respect to the C-Cl bond. As discussed above, a second time constant is evident in the time-dependent ion signal, but cannot be accurately determined. Its presence shows that the initial 50 fs process does not correspond to the time for dissociation. We

assume that it reflects this nonradiative population transfer to the lower-lying electronic states. One has to keep in mind that fs-experiments were conducted at a single excitation wavelength only. Time constants and initial dynamics might therefore change at higher excitation energies.

At first glance it might appear appropriate to compare CCl_3 with the methyl radical, CH_3 . However, the latter is planar and the lowest-lying electronically excited states correspond to Rydberg-states. In contrast, the nonbonding p-orbitals on the chlorine atoms, n_{Cl} enforce a pyramidal geometry of CCl_3 and additional low-energy transitions due to excitation of these orbitals. Thus nonradiative deactivation pathways are available that are not present in methyl.

While TR-PES unravels the early steps of the dynamics, photofragment imaging gives information on the product state distributions, i.e. the processes that occur after the rapid population transfer to the lower-lying states. The ns-data show that reaction (4.I) dominates, i.e. loss of Cl, associated with CCl_2 . As visible in Figure 4.5, four pathways are possible for loss of a chlorine atom, leading to CCl_2 either in the X $^1\text{A}_1$ ground state or the a $^3\text{B}_1$ excited triplet state. Both can be formed with a Cl atom in the $^2\text{P}_{3/2}$ ground state or the $^2\text{P}_{1/2}$ spin-orbit excited state, which are separated by $10.52 \text{ kJ mol}^{-1}$. The latter two cannot be distinguished in the translational energy distribution. Due to side reactions contributing to the Cl signal, most information on (4.I) is available when the CCl_2 molecular fragment is monitored.

Interpretation of the data and derivation of a dissociation model are not straightforward. The image shows a unimodal distribution, with the fraction of excess energy released into product translation $\langle f_T \rangle = 26\text{-}29\%$, assuming formation of CCl_2 in the X $^1\text{A}_1$ ground state (4.Ia). Formation of CCl_2 in the a $^3\text{B}_1$ state (4.Ib) would also be thermochemically possible, but $P(E_T)$ extends beyond the maximum translational energy expected for this reaction, so the X $^1\text{A}_1$ product state has to dominate. For example, at 250 nm, the observed $\langle E_T \rangle$ would correspond to $\langle f_T \rangle \approx 60\%$ assuming a triplet product, far above the range expected for statistical as well as impulsive dissociation. In addition, $P(E_T)$ is unimodal and β does not vary with translational energy. Due to the radical temperature in the jet of 150 K (vide supra) hot band transitions might contribute, but especially at 250 nm excitation they cannot explain the shape of $P(E_T)$ when compared with previous work.^{45,66} Therefore, we assume that (Ia) dominates and contributions from (4.Ib) are small, if present at all. Formation of CCl_2 (A $^1\text{B}_1$) is energetically possible at the highest excitation energies, but not consistent with the observed $P(E_T)$. As the molecular fragment is monitored and the VUV detection scheme cannot probe Cl^* , there is no information on the spin-orbit branching ratio. The shape of $P(E_T)$ appears Boltzmann-like and at first glance seems to indicate a ground state dissociation after redistribution of vibrational energy, following a statistical mechanism. However, 26–29% of the excess energy are released into translation, which is significantly more than usually observed in a statistical distribution. In the statistical photodis-

sociation of cyclic hydrocarbons^{66,67} and aryl chlorides at 193 nm values⁶⁸ for $\langle f_T \rangle$ between 10% and 12% have been observed, while in the H-atom loss from hydrocarbon radicals $\langle f_T \rangle$ of up to 15 to 20% have been reported.^{69,70} Thus in the present work $\langle f_T \rangle$ exceeds the range of values previously observed for statistical dissociation. In addition, an anisotropic PAD with a positive β is observed, which suggests that dissociation is faster than a rotational period and thus supports a model based on a prompt dissociation. According to preliminary computations, both the 2^2A_1 and 1^2A_2 states of CCl_3 result in a dissociation to the X 1A_1 state of CCl_2 . Dissociation in these states would be commensurate with the observations. From an impulsive model for dissociation along a repulsive coordinate we expect a larger $\langle f_T \rangle = 0.36$, but this simple approach neglects effects like geometry changes during the dissociation and should thus be seen as a limiting case. Interestingly, β decreases with an increase in wavelength from 0.5 at 230 nm to 0.06 at 250 nm (see Figure 4.S6, SI), suggesting either a slower dissociation at lower energies or an involvement of different electronic states. Different contributions of the 2^2E (D_4) and 3^2A_1 (D_5) states to the initial absorption might lead to different anisotropies. As for the 2^2E state μ_T is oriented in the C-Cl plane, we expect a positive β -value for the Cl photofragment angular distribution, whereas for the (most likely planar) 3^2A_1 state, a negative β is expected, because μ_T is oriented along the symmetry axis.⁷¹ Therefore, the contribution of the 2^2E state to the absorption band might increase to the blue and possibly lead to a change of dissociation mechanism with excitation energy. However, the almost constant shape of $P(E_T)$ at all wavelengths does not support this model. We therefore suggest an alternative explanation, a stepwise deactivation of the optically excited state. At lower excitation energies, CCl_3 could be trapped for a few vibrational periods in an intermediate state (e.g. the 1^2A_2), sufficiently long to partially lose its anisotropy, whereas at higher excitation energies such a barrier is rapidly surmounted. Note that the rise time of the two-colour signal (Figure 4.S3, SI) is on the scale of the laser pulse duration, in agreement with a dissociation on a sub-ns time scale. High-level computations are required to verify this model.

The only previous study on CCl_3 photodissociation was reported by Hints et al., who excited the radical at 308 nm and observed the CCl_2 fragment by translational energy spectroscopy.³⁴ Here, CCl_3 was generated by photolysis of CCl_4 at 193 nm, so radicals were most likely internally hot. Hints et al. observed a total translational energy release of less than 30% and $\beta = 1.0 \pm 0.2$, in qualitative agreement with the present results. No indication of pathway (4.II), loss of Cl_2 was found in this work.

Besides the CCl_2 molecular fragment, the Cl signal has also been analysed at 230 nm. Momentum matching of CCl_2 and Cl fragments and a comparable anisotropy parameter β indicate that both fragments predominately originate from the same source. However, there are visible differences that suggest contributions from competing processes to the Cl signal, possibly dissociation of

CCl_2 (4.III) or CCl_4 (4.V) as well as multiphoton-processes (4.IV), so it is difficult to disentangle their contribution from (4.I).

In addition to Cl-loss, pathway (4.II) to $\text{CCl} + \text{Cl}_2$ is also thermochemically accessible (see Figure 4.5). The CCl images show two distinguishable features, a dominant low energy one, which maximizes at around 0.1 eV and a second one centred around 0.4 eV. However, CCl_2 , which is a minor product in the pyrolysis can also dissociate to CCl (see right-hand side of Figure 4.5). Control experiments using CHCl_3 , a known precursor for CCl_2 , also yield a bimodal translational energy distribution for the CCl photofragment. The higher energy component, centred at 0.4 eV is dominant in the experiments utilizing CHCl_3 and can thus be assigned to pathway (4.III), photodissociation of CCl_2 produced in the pyrolysis to $\text{CCl} + \text{Cl}$. The anisotropic PAD for this main peak with β between 0.7 and 1 and the large $\langle f_T \rangle$ of about 43% indicate that CCl_2 dissociates to CCl along a repulsive coordinate. An impulsive model yields $\langle f_T \rangle = 0.41$, in almost perfect agreement with the experiment. The origin of a low energy contribution in the photodissociation of CCl_2 is still being investigated, but the smaller $\langle f_T \rangle$ and the absence of anisotropy point towards a statistical mechanism. With this information, the peaks in the CCl image from CCl_4 as a precursor can be assigned. The distribution derived from the CCl_2 experiment is given as a dotted magenta line in the upper trace of Figure 4.7 (230 nm dissociation). The shoulder at around 0.4 eV is attributed to the direct dissociation of CCl_2 formed in the pyrolysis and not related to CCl_3 photodissociation. However, the low energy contribution at around 0.1 eV is significantly larger than in the CCl_2 experiments, thus it seems to originate partially from CCl_3 dissociation. This additional contribution at low energy is depicted as a dashed brown line in the figure. The $P(E_T)$ of CCl also shows a signal that extends to high translational energies and requires absorption of two photons. This component must originate from the consecutive process (IV), which deposits extra internal energy in the CCl_2 and thus leads to a broad $P(E_T)$. It is indicated as a dash-dotted green line in the figure. It is difficult to imagine that the strong component maximizing at $E_T = 0.1$ eV is exclusively due to this sequential process. Thus we conclude that reaction (4.II) contributes to this component, represented as a dashed brown line in Figure 4.7. We point out that the counterfragment Cl_2 has not been detected. Quantification of the various reaction channels is not possible, because the ionisation cross sections σ_{ion} of CCl_2 and CCl are not known. Compared to alkyl chlorides, one important difference should be noted. In many alkyl halides, the spin orbit branching ratio of chlorine is determined by the interaction between the $^3\text{Q}_0$ and the ^1Q states. In CCl_3 , however, all low-lying excited states are doublets, with the quartet states higher in energy. Direct dissociation of a quartet state corresponds to a CCl_2 fragment either in the triplet (4.Ib) or the open-shell singlet state. The present work provides no evidence for either product and thus rules out dissociation from a quartet state. Nevertheless,

quartet states might be involved in the non-radiative relaxation. The question of whether such interactions lead to the formation of spin-orbit excited chlorine atoms remains open.

4.6 Conclusions

The photodissociation dynamics of CCl_3 upon UV excitation was investigated by fs time-resolved photoionisation and photofragment imaging of the reaction products to follow the photodynamics along the complete reaction coordinate. The radical was generated by pyrolysis of CCl_4 and CH_3Br . Excitation between 230 nm and 266 nm is due to transitions into the D_4 (2E) and D_5 (2A_1) states, as indicated by TD-DFT. The fs-experiments show a rapid motion out of the Franck-Condon window within around 50 fs. A second slightly longer time constant is recognisable, but cannot be determined accurately. It is most likely due to a fast nonradiative deactivation to lowerlying dissociative or pre-dissociative electronic states. Here, the fate of the radicals was monitored by photofragment imaging. Dissociation of CCl_3 leads to $\text{CCl}_2 + \text{Cl}$. A velocity map image of the CCl_2 photofragment shows an anisotropic distribution and a translational energy release of 26-29%, indicating a dissociation in less than a rotational period. The Cl-fragment image is to a large extent momentum matched and the β -parameter is similar, but it contains additional contributions, in part from the photodissociation of CCl_2 , which is produced in the pyrolysis in small amounts. Furthermore, as the photoproduct from CCl_3 it can absorb a second photon and dissociate.

Images of CCl were recorded to get insight into the second reaction pathway, leading to $\text{CCl} + \text{Cl}_2$. Control experiments using the pyrolysis of CH_3Cl , a known CCl_2 precursor, revealed the contribution of CCl_2 dissociation to the CCl fragment signal. An anisotropic component centred at around 0.4 eV is due to direct dissociation of CCl_2 . An isotropic one at low translational energies increases significantly when CCl_3 is present, indicating the presence of reaction (II), dissociation of CCl_3 to $\text{CCl} + \text{Cl}_2$. The long tail in the translational energy distribution shows the presence of a multiphoton process, i.e. stepwise dissociation of CCl_3 , thus the CCl contribution that originates from (4.II) cannot be quantified.

4.7 Conflicts of interest

There are no conflicts of interest to declare.

4.8 Acknowledgements

This work has been financially supported by the Deutsche Forschungsgemeinschaft, GRK 2112 and FI 575/13-1. The femtosecond experiments were conducted at the CEA Saclay and supported by Laserlab Europe (SLIC001972). We would like to thank Jens Giegerich for contributions to the fs-experiments. Travel support by the DAAD and by PHC Program PROCOPE 2015 (Grant No. 32980XH) is gratefully acknowledged. The authors kindly thank Michel Perdrix and Delphine Guillaumet for setting up and maintaining the SLIC/LUCA laser. A. R. thanks Ryan E. McDonell for helpful and insightful discussions.

4.9 Supplementary Information

4.9.1 Further Experimental Details

In this section, additional information on the photofragment imaging experiments conducted at the University of Würzburg is given. The ion optics consists of three velocity-focusing plates (repeller, extractor, ground; separated by 15 mm) which accelerate the ions towards the detector. An electric field of 615 V/cm between repeller and extractor and 2719 V/cm between extractor and ground was applied for mass spectrometry, while electric fields of 1014 V/cm and 2319 V/cm were applied for the velocity map imaging experiments. The detector consists of a dual stage microchannel plate (MCP) followed by a phosphorescent screen (P43). The front MCP was kept at ground potential in order to ensure a field-free drift condition. The voltage on the second MCP was regulated by a push/pull switch with a gate of 100 ns in order to only detect the fragments of interest during velocity map imaging experiments. The resulting signal that is visible on the phosphorescent screen was then recorded with a progressive-scan camera with a 2/3" CCD chip. An achromatic object lens was attached to the camera for focusing of the image.

The average power of the third harmonic of the Nd-YAG laser (355nm) used in the ionisation of the molecular fragments was around 16 mJ/pulse. This light was focused with a $f = 200$ mm lens into a tripling cell filled with xenon, generating 118.2 nm light. This light was then focused with a MgF2 ($f = 100$ mm) lens into the ionisation region.

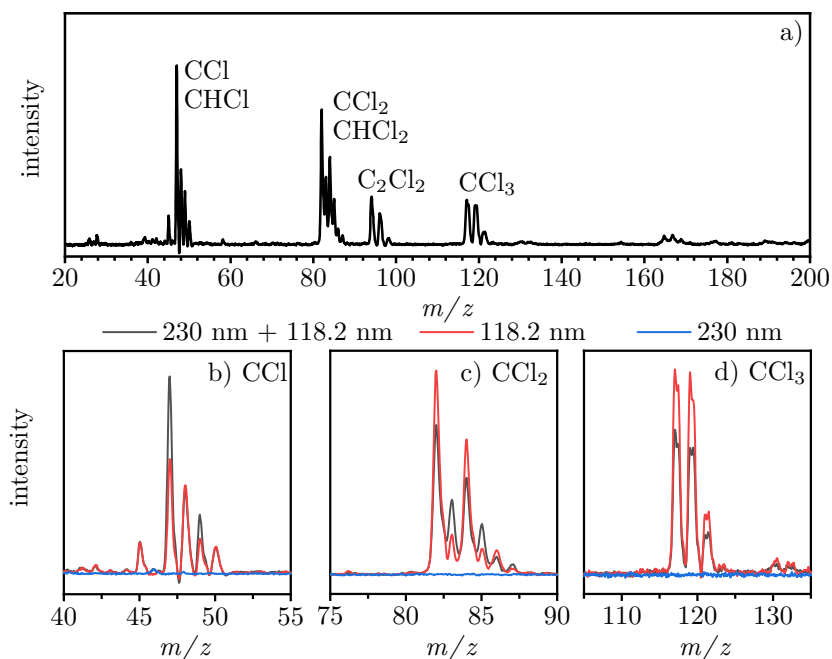


Figure 4.S1: In a) the two-colour mass spectrum using chloroform, CHCl_3 as a precursor for CCl_2 is shown. It was recorded with $\lambda_{\text{diss}} = 230$ nm and $\lambda_{\text{ion}} = 118.2$ nm at a pyrolysis power of 40 W. Furthermore, close-ups of the CCl (m/z 47) b), CCl_2 (m/z 82) c) and CCl_3 (m/z 117) d) mass signals. The one-color signals are added. In red the signal generated by only the ionisation laser and in blue by only the dissociation laser are shown. As visible, the CCl_3 and CCl_2 signals decrease in the presence of the dissociating laser, while the CCl signal increases.

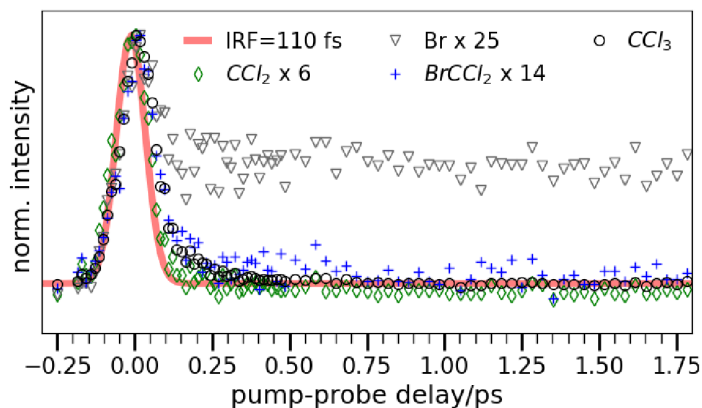


Figure 4.S2: Time-resolved ion signals recorded in the fs-experiments. All signals are normalised to the maximum of the CCl_3 peak, scaling factors are given in the legend. As visible, only the Br^+ signal has an appreciable intensity at long delay times.

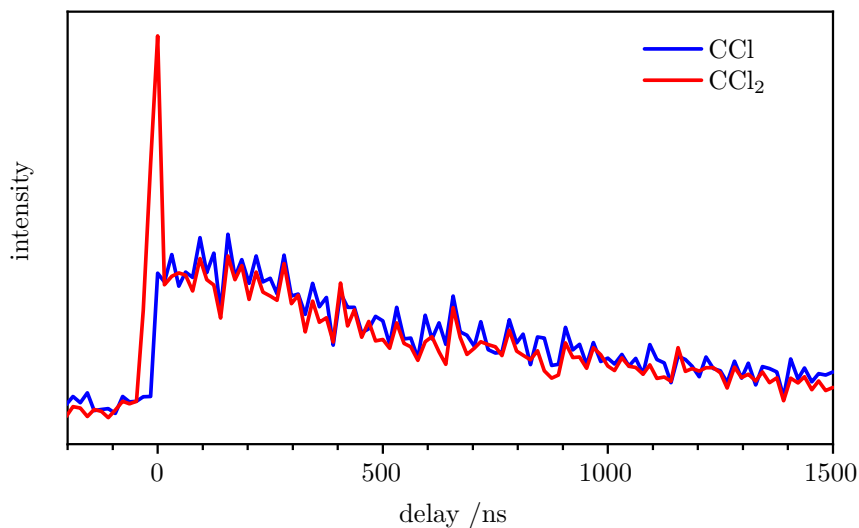


Figure 4.S3: Time delay between dissociation and ionisation laser for the CCl (blue) and CCl_2 (red) fragment in the ns-experiments for $\lambda_{\text{diss}} = 230$ nm. CCl_4 was employed as a precursor. The rise time is within the resolution of the nanosecond laser systems thus the process is faster than 10 ns. The initial CCl_2 peak is caused by the “inverse” process: The ionisation laser first ionizes a parent fragment which is then dissociated by the dissociation laser.

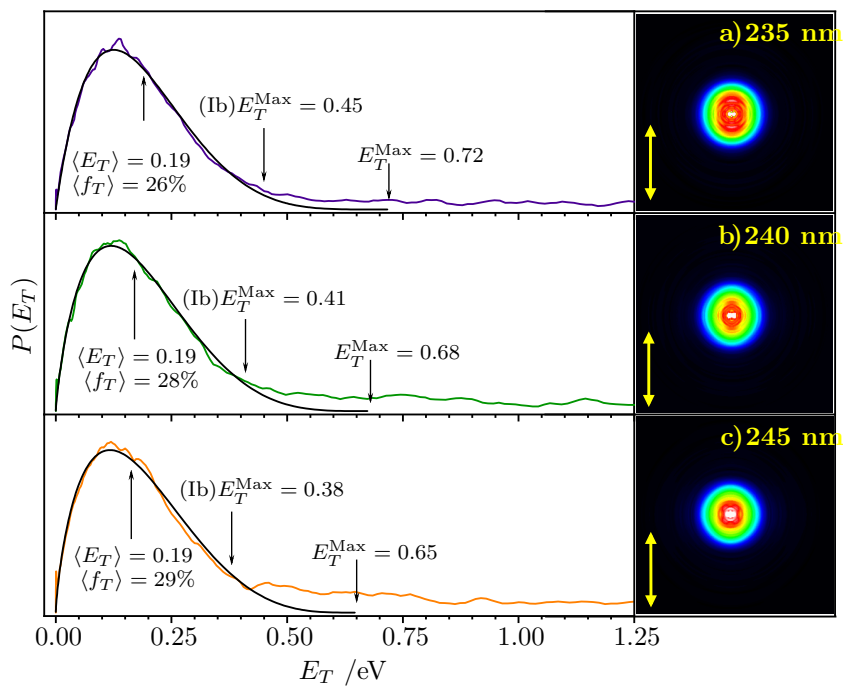


Figure 4.S4: Translational energy distribution $P(E_T)$ of the CCl_2 fragment upon excitation of CCl_3 with a) 235 nm, b) 240 nm and c) 245 nm light. CCl_4 was employed as a precursor. The experimental data are drawn in black and a fit using expression (4.1) in colour. The corresponding velocity map images are shown with a yellow arrow indicating the laser polarization.

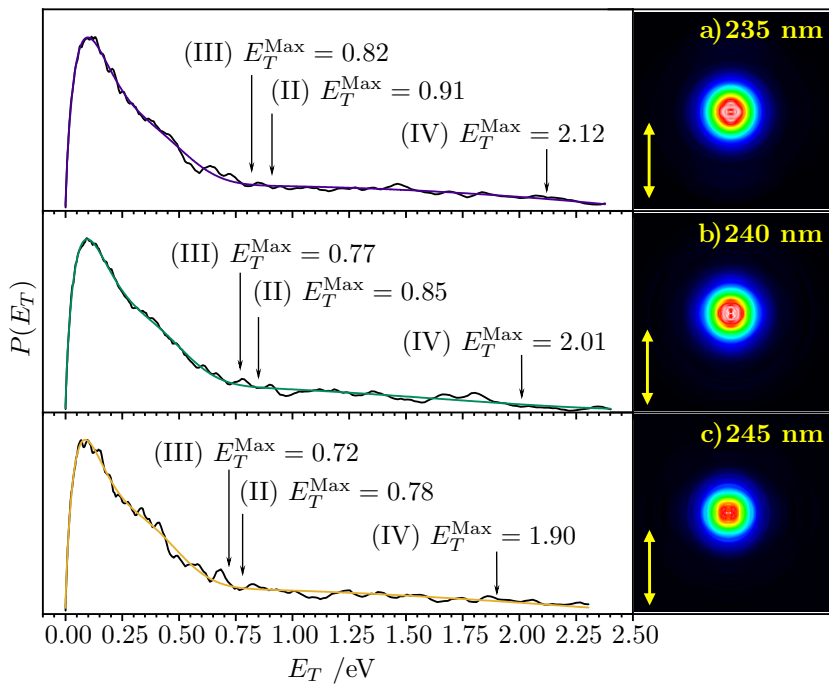


Figure 4.S5: Translational energy distribution $P(E_T)$ of the CCl fragment using CCl_4 as a precursor for CCl_3 . In a) 235 nm, b) 240 nm and in c) 245 nm light was used for dissociation. The experimental results are shown in black, while a superposition of two two-parameter fits using expression (4.1) and a Gaussian distribution is shown as a colored line. The corresponding velocity map images are shown with an arrow indicating the laser polarization in yellow.

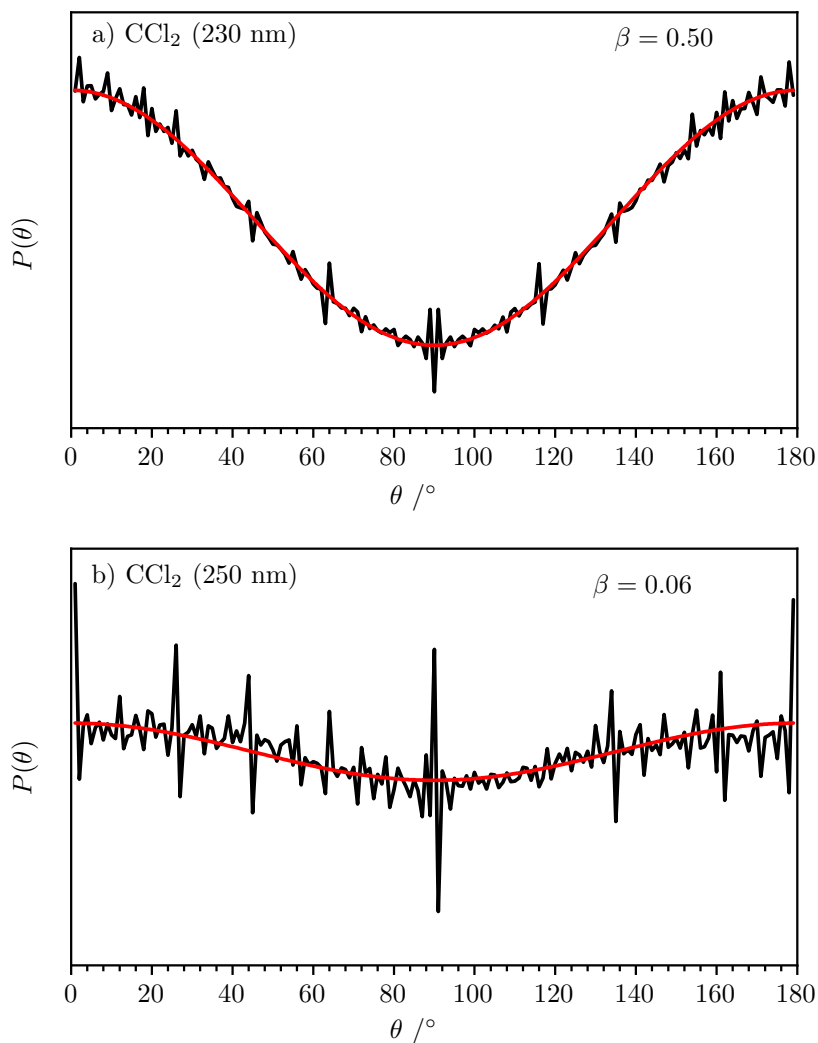


Figure 4.S6: Angular distribution of the CCl₂ images of at the dissociation wavelengths of a) 230 nm and b) 250 nm (black curves) and the corresponding fits using the equation $I(\theta) = N \cdot [1 + \beta P_2(\cos(\theta))]$ where $P_2(\cos(\theta))$ is the 2nd order Legendre polynomial. The CCl₂ fragment at 230 nm shows a clear anisotropy with a beta value of 0.5. At longer wavelengths β decreases and is only 0.06 at 250 nm.

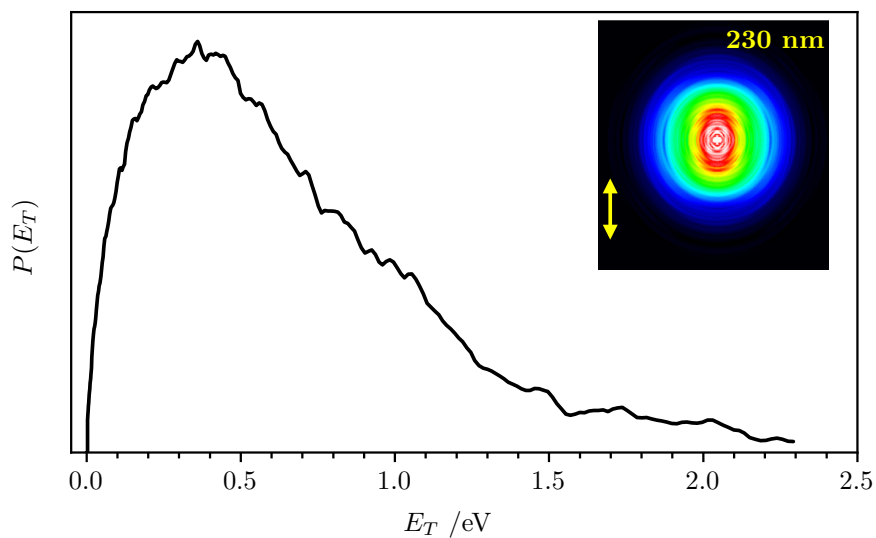


Figure 4.S7: Translational energy distribution $P(E_T)$ of the Cl ($^2P_{3/2}$) photofragment after photodissociation with 230 nm light, using CCl_4 as a precursor. The corresponding velocity map image is shown with an arrow indicating the laser polarization in yellow.

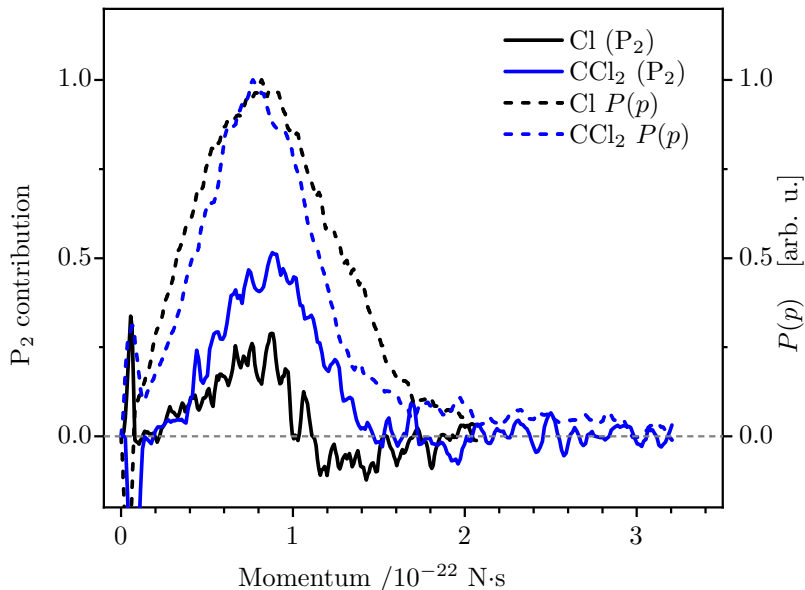


Figure 4.S8: Comparison of the momenta of the Cl and CCl₂ fragments from the photodissociation of CCl₃ (dotted black and blue lines respectively) and the P₂ term (contribution of the Legendre polynomial 2nd order, solid line). The dotted line divided by the solid line is equivalent to the β -parameter. The rise for both contributions is similar, however, the CCl₂ image has a stronger anisotropy and the anisotropy for the Cl image falls off quicker and even reaches a negative value. This is probably caused by various side reactions that also release Cl, resulting in the beta anisotropy not matching completely.

Table 4.S1: Summary of the maximum possible kinetic energy E_T^{\max} for the CCl fragment for different reaction pathways, see main paper for definition of the reactions.

$\lambda_{\text{diss}}/\text{nm}$	E_T^{\max}/eV (II)	E_T^{\max}/eV (III)	E_T^{\max}/eV (IV)
230	0.98	0.87	2.24
235	0.91	0.82	2.12
240	0.85	0.77	2.01
245	0.78	0.72	1.90
250	0.72	0.68	1.80

4.10 Bibliography

- (1) Molina, M. J.; Rowland, F. S. *Nature* **1974**, *249*, 810–812.
- (2) Myers, T. L.; Kitchen, D. C.; Hu, B.; Butler, L. J. *J. Chem. Phys.* **1996**, *104*, 5446.
- (3) Morton, M. L.; Butler, L. J.; Stephenson, T. A.; Qi, F. *J. Chem. Phys.* **2002**, *116*, 2763–2775.
- (4) Matsumi, Y.; Das, P. K.; Kawasaki, M. *J. Chem. Phys.* **1992**, *97*, 5261.
- (5) Matsumi, Y.; Das, P. K.; Kawasaki, M. *J. Chem. Phys.* **1990**, *92*, 1696–1701.
- (6) Lin, J. J.; Chen, Y.; Lee, Y. Y.; Lee, Y. T.; Yang, X. *Chem. Phys. Lett.* **2002**, *361*, 374–382.
- (7) Foley, C. D.; Joalland, B.; Alavi, S. T.; Suits, A. G. *Phys. Chem. Chem. Phys.* **2018**, *20*, 27474–27481.
- (8) Deshmukh, S.; Hess, W. P. *J. Chem. Phys.* **1994**, *100*, 6429–6433.
- (9) Ahmed, M.; Peterka, D. S.; Regan, P.; Liu, X.; Suits, A. G. *Chem. Phys. Lett.* **2001**, *339*, 203–208.
- (10) Dixon, R. N.; Kroto, H. W. *Trans. Faraday Soc.* **1963**, *59*, 1484–1489.
- (11) Herzberg, G., *Molecular Spectra and Molecule Structure. I. Diatomic Molecules*. Krieger Pub Co: 1989.
- (12) Bondybey, V. E. *J. Mol. Spectrosc.* **1977**, *64*, 180–183.
- (13) Richmond, C.; Tao, C.; Mukarakate, C.; Fan, H.; Nauta, K.; Schmidt, T. W.; Kable, S. H.; Reid, S. A. *J. Phys. Chem.* **2008**, *112*, 11355–11362.
- (14) Liu, M. L.; Lee, C. L.; Bezant, A.; Tarczay, G.; Clark, R. J.; Miller, T. A.; Chang, B. C. *Phys. Chem. Chem. Phys.* **2003**, *5*, 1352–1358.
- (15) Shin, S. K.; Dagdigian, P. J. *J. Chem. Phys.* **2008**, *128*, 154322.
- (16) Shin, S. K.; Dagdigian, P. J. *J. Chem. Phys.* **2006**, *125*, 133317.
- (17) Shin, S. K.; Dagdigian, P. J. *Phys. Chem. Chem. Phys.* **2006**, *8*, 3446–3452.
- (18) Morley, G. P.; Felder, P.; Huber, J. R. *Chem. Phys. Lett.* **1994**, *219*, 195–199.
- (19) Bacskey, G. B. *Mol. Phys.* **2015**, *113*, 1608–1617.
- (20) Richmond, C.; Tao, C.; Mukarakate, C.; Dawes, R.; Brown, E. C.; Kable, S. H.; Reid, S. A. *J. Chem. Phys.* **2011**, *135*, 104316.
- (21) Tao, C.; Mukarakate, C.; Reid, S. A. *J. Mol. Spectrosc.* **2007**, *241*, 136–142.
- (22) Schlachta, R.; Lask, G.; Stangassinger, A.; Bondybey, V. E. *J. Phys. Chem.* **1991**, *95*, 7132–7134.

- (23) Dribinski, V.; Potter, A. B.; Demyanenko, A. V.; Reisler, H. *J. Chem. Phys.* **2001**, *115*, 7474–7484.
- (24) Levchenko, S. V.; Demyanenko, A. V.; Dribinski, V. L.; Potter, A. B.; Reisler, H.; Krylov, A. I. *J. Chem. Phys.* **2003**, *118*, 9233–9240.
- (25) Møgelberg, T. E.; Sehested, J.; Nielsen, O. J.; Wallington, T. J. *J. Phys. Chem.* **1995**, *99*, 16932–16938.
- (26) Gushchin, A. A.; Grinevich, V. I.; Izvekova, T. V.; Kvitkova, E. Y.; Tyukanova, K. A.; Rybkin, V. V. *Chemosphere* **2021**, *270*, 129392.
- (27) Nottingham, W. C.; Rudolph, R. N.; Andrews, K. P.; Moore, J. H.; Tossell, J. A. *Int. J. Chem. Kinet.* **1994**, *26*, 749–756.
- (28) Fenter, F. F.; Lightfoot, P. D.; Niiranen, J. T.; Gutman, D. *J. Phys. Chem.* **1993**, *97*, 5313–5320.
- (29) Danis, F.; Caralp, F.; Rayez, M. T.; Lesclaux, R. *J. Phys. Chem.* **1991**, *95*, 7300–7307.
- (30) Hudgens, J. W.; Johnson, R. D.; Tsai, B. P.; Kafafi, S. A. *J. Am. Chem. Soc.* **1990**, *112*, 5763–5772.
- (31) Danis, F.; Caralp, F.; Veyret, B.; Loirat, H.; Lesclaux, R. *Int. J. Chem. Kinet.* **1989**, *21*, 715–727.
- (32) Ellermann, T. *Chem. Phys. Lett.* **1992**, *189*, 175–181.
- (33) Robles, E. S.; Chen, P. *J. Phys. Chem.* **1994**, *98*, 6919–6923.
- (34) Hintsä, E. J.; Zhao, X.; Jackson, W. M.; Miller, W. B.; Wodtke, A. M.; Lee, Y. T. *J. Phys. Chem.* **1991**, *95*, 2799–2802.
- (35) Horn, M.; Botschwina, P. *Chem. Phys. Lett.* **1994**, *228*, 259–267.
- (36) Röder, A.; Petersen, J.; Issler, K.; Fischer, I.; Mitrić, R.; Poisson, L. *J. Phys. Chem.* **2019**, *123*, 10643–10662.
- (37) Stolow, A.; Bragg, A. E.; Neumark, D. M. *Chem. Rev.* **2004**, *104*, 1719–1757.
- (38) Stolow, A. *Annu. Rev. Phys. Chem.* **2003**, *54*, 89–119.
- (39) Eppink, A. T.; Parker, D. H. *Rev. Sci. Instrum.* **1997**, *68*, 3477–3484.
- (40) Whitaker, B. J., *IMAGING IN MOLECULAR DYNAMICS Technology and Applications (A User's Guide)*; Cambridge University Press: 2003.
- (41) Vallance, C. *Chem. Commun.* **2019**, *55*, 6336–6352.
- (42) Suits, A. G. *Rev. Sci. Instrum.* **2018**, *89*, 111101.
- (43) Ashfold, M. N.; Ingle, R. A.; Karsili, T. N.; Zhang, J. *J. Phys. Chem. Chem. Phys.* **2019**, *21*, 13880–13901.
- (44) Steinbauer, M.; Giegerich, J.; Fischer, K. H.; Fischer, I. *J. Chem. Phys.* **2012**, *137*, 014303.

-
- (45) Giegerich, J.; Petersen, J.; Mitrić, R.; Fischer, I. *Phys. Chem. Chem. Phys.* **2014**, *16*, 6294–6302.
- (46) Schuurman, M. S.; Giegerich, J.; Pachner, K.; Lang, D.; Kiendl, B.; MacDonell, R. J.; Krueger, A.; Fischer, I. *Chem. Eur. J.* **2015**, *21*, 14486–14495.
- (47) Matthaai, C. T.; Mukhopadhyay, D. P.; Fischer, I. *J. Phys. Chem.* **2021**, *125*, 2816–2825.
- (48) Röder, A.; Issler, K.; Poisson, L.; Humeniuk, A.; Wohlgemuth, M.; Comte, M.; Lepetit, F.; Fischer, I.; Mitric, R.; Petersen, J. *J. Chem. Phys.* **2017**, *147*, 013902.
- (49) Röder, A.; Humeniuk, A.; Giegerich, J.; Fischer, I.; Poisson, L.; Mitrić, R. *Phys. Chem. Chem. Phys.* **2017**, *19*, 12365–12374.
- (50) Garcia, G. A.; Nahon, L.; Powis, I. *Rev. Sci. Instrum.* **2004**, *75*, 4989–4996.
- (51) Shao, Y. et al. *Mol. Phys.* **2015**, *113*, 184–215.
- (52) Barnes, L.; Abdul-Al, S.; Allouche, A. R. *J. Phys. Chem.* **2014**, *118*, 11033–11046.
- (53) Kohn, D. W.; Robles, E. S.; Logan, C. F.; Chen, P. *J. Phys. Chem.* **1993**, *97*, 4936–4940.
- (54) Ruscic, B.; H., B. D. Active Thermochemical Tables (ATcT) values based on ver. 1.122p of the Thermochemical Network, 2020.
- (55) Ruscic, B.; Pinzon, R. E.; Morton, M. L.; Laszevski, G. V.; Bittner, S. J.; Nijssure, S. G.; Amin, K. A.; Minkoff, M.; Wagner, A. F. *J. Phys. Chem.* **2004**, *108*, 9979–9997.
- (56) Keller-Rudek, H.; Moortgat, G. K.; Sander, R.; Sörensen, R. *Earth System Science Data* **2013**, *5*, 365–373.
- (57) Kawasaki, M.; Suto, K.; Sato, Y.; Matsumi, Y.; Bersohn, R. *J. Phys. Chem.* **1996**, *100*, 19853–19858.
- (58) Rebbert, R. E.; Ausloos, P. J. *J. Photochem.* **1976**, *6*, 265–276.
- (59) Pachner, K.; Steglich, M.; Hemberger, P.; Fischer, I. *J. Chem. Phys.* **2017**, *147*, 084303.
- (60) Deyerl, H. J.; Fischer, I.; Chen, P. *J. Chem. Phys.* **1999**, *111*, 3441–3448.
- (61) North, S. W.; Marr, A. J.; Furlan, A.; Hall, G. E. *J. Phys. Chem.* **1997**, *101*, 9224–9232.
- (62) Tuck, A. F. *J. Chem. Soc., Faraday Trans. 2* **1977**, *73*, 689–708.
- (63) Galloway, D. B.; Glenewinkel-Meyer, T.; Bartz, J. A.; Huey, L. G.; Crim, F. F. *J. Chem. Phys.* **1994**, *100*, 1946–1952.
- (64) Lee, L. C.; Suto, M.; Tang, K. Y. *J. Chem. Phys.* **1985**, *84*, 5277–5283.

- (65) Lambert, H. M.; Dagdigian, P. J. *Chem. Phys. Lett.* **1997**, *275*, 499–505.
- (66) Giegerich, J.; Fischer, I. *Phys. Chem. Chem. Phys.* **2013**, *15*, 13162–13168.
- (67) Tsukiyama, K.; Bersohn, R. *J. Chem. Phys.* **1986**, *86*, 745–749.
- (68) Ichimura, T.; Mori, Y.; Shinohara, H.; Nishi, N. *J. Chem. Phys.* **1997**, *107*, 835–842.
- (69) Giegerich, J.; Fischer, I. *J. Chem. Phys.* **2015**, *142*, 044304.
- (70) Sun, G.; Lucas, M.; Song, Y.; Zhang, J.; Brazier, C.; Houston, P. L.; Bowman, J. M. *J. Phys. Chem.* **2019**, *123*, 9957–9965.
- (71) Rakitzis, T. P.; Zare, R. N. *J. Chem. Phys.* **1999**, *110*, 3341–3350.

5 Velocity Map Imaging Study of the Photodissociation of Dichlorocarbene in the VUV

5.1 Abstract

The photodissociation dynamics of dichlorocarbene, CCl_2 , generated via flash pyrolysis of chloroform was investigated. UV radiation between 230 nm and 250 nm was used to produce CCl and Cl photofragments which were then examined with the velocity map imaging technique, giving insights into the translational energy distribution of these fragments. A bimodal translational energy distribution is observed. One pathway is a direct dissociation from an excited state showing an average kinetic energy of 48% of the maximally possible, while the second pathway is a predissociation. Because of the overlap between these two contributions an exact value for the expectation value of this second contribution cannot be given.

5.2 Introduction

Halogen-containing species play a major role as a greenhouse gas¹ and in the catalytic destruction of stratospheric ozone.² These findings led to thorough examinations of various alkyl and alkenyl halides in the gas phase. Especially chlorinated compounds that release atomic chlorine upon UV-absorption have been studied in order to gain UV photoabsorption spectra and photodissociation cross sections.³⁻¹⁰ On the other hand, the radicals that can be generated via photodissociation from these molecules, i.e. haloalkyl radicals, have not been studied in much detail yet.

Dichlorocarbene (CCl_2) is one of the photofragments generated in the stratosphere from the photodissociation of molecules like tetrachloromethane, CCl_4 .¹¹ As such, it can be an additional source of stratospheric chlorine and is of interest for atmospheric chemistry. Photoelectron spectra of CCl_2 have been recorded by Kohn et al.¹² The photodissociation of CCl_2 has been studied by the group of Dagdigian using laser-induced fluorescence spectroscopy.¹³⁻¹⁵ They observed a bimodal rotational state distribution for the reaction $\text{CCl}_2 + h\nu \rightarrow \text{CCl} + \text{Cl}$. The translational energy distribution of the photofragments was investigated by Morley et al., who only observed a unimodal energy distribution.¹⁶ In the past, we studied the photodissociation dynamics of CCl_3 , produced via flash pyrolysis, with the velocity map imaging technique. In these studies we observed that the photodissociation of CCl_2 which also got generated via pyrolysis contributed to the recorded CCl image.¹¹

Here, we investigate the photodissociation of CCl_2 in greater detail using the velocity map imaging in order to gain a deeper insight into the photodissoci-

ation dynamics of this for atmospheric chemistry important carbene.^{17,18} Like in former works, we generate the CCl_2 via flash pyrolysis from chloroform, CHCl_3 .¹³⁻¹⁶ We then dissociated the CCl_2 with a UV light in the range of 230 nm to 250 nm and subsequently ionized the generated fragments via single photon ionization (SPI) with 118.2 nm. Atomic chlorine is ionized via $[1 + 1']$ resonance enhanced multiphoton ionization at 118.9 nm.

5.3 Experimental

We generated CCl_2 via flash pyrolysis of CHCl_3 (chloroform) which we obtained from Sigma-Aldrich. The chloroform was seeded in 1.6 bar of Ar. This mixture then passed through a solenoid pulsed valve into an electrically heated SiC tube, thermally cleaving the chloroform. After the SiC tube, the generated radicals were adiabatically expanded into vacuum, where they were cooled to a vibrational temperature of about 150 K, as concluded from previous work.¹⁹

This molecular beam then passed through a skimmer into a second vacuum chamber, used for the velocity map imaging (VMI) technique.^{17,18} It consists of a time of flight mass spectrometer (TOF-MS), which can be operated in either space-focusing or VMI configuration. The radicals were then dissociated and ionized via two counterpropagating laser beams (10 ns pulse duration). This allows for the study of the generated photofragments. The laser systems employed are two dye lasers, pumped by Nd:YAG lasers, and an additional Nd:YAG laser. For the photodissociation 1.2 mJ of the second harmonic of one of the dye lasers was utilized (230-250 nm/5.39-4.96 eV). In order to ionize the molecular fragments we generated the 9th order of the additional Nd:YAG laser (118.2 nm, 10.49 eV). For this, the third harmonic of the Nd:YAG laser was focused into a xenon-filled gas cell, directly attached to the vacuum chamber, which triples the frequency of the incident light. Atomic chlorine fragments were ionized with the second dye laser in a $[1+1']$ resonance-enhanced MPI process at 118.9 nm ($^2\text{D}_{5/2} \leftarrow ^2\text{P}_{3/2}^o$). Here, the frequency doubled output of the dye laser was focused into the gas cell. The wavelength of the laser is scanned over the entire Doppler profile of the atomic transition. From the $^2\text{D}_{5/2}$ state, the residual 356.7 nm light ionizes the atoms. However, this scheme only allows for the observation of ground state chlorine ($^2\text{P}_{3/2}^o$), since the spin-orbit excited state ($^2\text{P}_{1/2}$) cannot be exited within the tripling range of our setup.²⁰

The ionized photofragments are then accelerated towards a dual stage microchannel plate (MCP) assembly, followed by a phosphorescent screen (P43). The ion optics utilized for this, consist of three equally spaced velocity-focusing plates (15 cm; repeller, extractor, ground). For mass spectrometry an electric field of 615 V/cm was applied between repeller and extractor and 2719 V/cm between extractor and ground. These electric fields were changed to 1014 V/cm and 2319 V/cm for the velocity map imaging experiments respectively. The

front MCP was grounded, in order to ensure a field-free drift condition inside of the flight tube. A voltage of around 1.8 kV, controlled by a push/pull switch, was applied to the second MCP. The length of the utilized gate was 100 ns, allowing to only detect the fragments of interest during the VMI experiments. The current generated by the impact of the ions on the MCPs was monitored by an oscilloscope, which gives us the mass spectra. The impact events on the MCPs are also visible on the phosphorescent screen. This signal is recorded with a progressive-scan camera with a 2/3" CCD chip, to which an achromatic lens was attached.

In order to extract the translation energy distributions ($P(E_T)$) from the images, the 3D Newton spheres were then reconstructed via inverse Abel transformation utilizing the pBASEX algorithm. Legendre polynomials up to the 4th order were used.²¹

5.4 Results

5.4.1 Mass spectra

In Figure 5.1 photoionization mass spectra are shown. In the top section (Figure 5.1 a)) the mass spectrum of the photofragments dissociated by 230 nm light of the pyrolyzed CHCl_3 is shown (30 W applied to the SiC tube). The predominant pyrolysis product is CCl_2 ($m/z = 82-86$). Smaller amounts of CCl ($m/z = 47-49$) and CHCl ($m/z = 48-50$) are also clearly visible, while minute amounts of C_2Cl_2 ($m/z = 94-98$) and CCl_3 ($m/z = 117-123$) can be observed as well. Detailed close ups of the CCl and CCl_2 fragments are shown in Figure 5.1 b) and Figure 5.1 c). The black curve represents the two-color mass spectrum with both dissociation and ionization laser. The blue curve depicts the one-color mass spectrum with only the ionization laser being used. The difference between the two curves shows the amount of the fragment generated by the dissociation laser. First thing to note in the close up is that also tiny amounts of CHCl_2 ($m/z = 83-87$) are generated in the pyrolysis, and the amount increases slightly due to the photodissociation of residual CHCl_3 in the molecular beam. However, the amount of CHCl stays the same, meaning no measurable amount CHCl_2 gets dissociated. Also, no change in the amount of CCl_2 could be observed. The only considerable two-color signal, that is visible, is the increase of the CCl signal. Chloroform itself however cannot be observed in the mass spectrum since its ionization energy is 11.37 eV and thus above the photon energy of the used ionization laser.

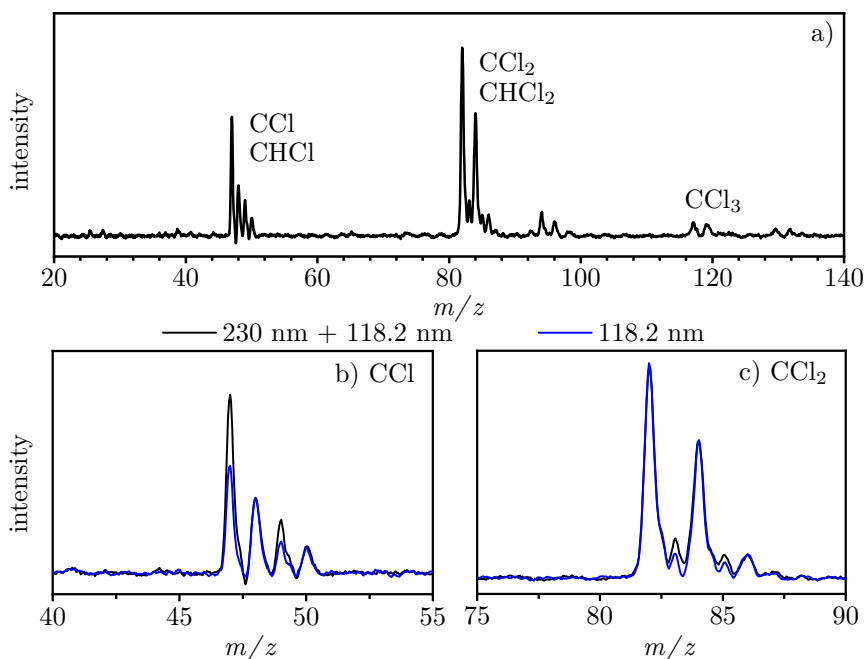
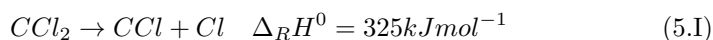


Figure 5.1: a) shows the mass spectrum obtained from using CHCl_3 as a precursor and then dissociating the generated fragments with 230 nm light. For ionization a wavelength of 118.2 nm was used. Mainly CCl_2 can be seen. Also CCl , CHCl and CHCl_2 are present. In b) and c) a close up of the CCl and CCl_2 region are shown with (black) and without (blue) dissociation laser. Only the CCl and CHCl_2 signals increase. The increase in CCl signal is roughly 3.5 greater than that of CHCl_2

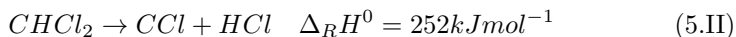
5.4.2 Velocity map imaging

CCl_2 images.

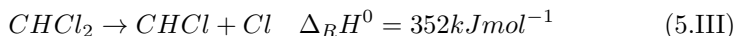
After confirming that mainly CCl_2 is produced in the pyrolysis, the photodissociation of it was studied with the velocity map imaging technique using a dissociation laser between 230 nm ($520.1 \text{ kJ mol}^{-1}/5.39 \text{ eV}$) and 250 nm ($478.5 \text{ kJ mol}^{-1}/4.96 \text{ eV}$). Upon absorption of a photon, the CCl_2 can dissociate producing CCl and Cl . Under the assumption that there is no reverse barrier for the reaction, the bond dissociation energy (BDE) is the same as the heat of reaction (5.1).



Another potential pathway for the formation of CCl is from the dissociation of CHCl₂:



Since the mass spectrum shows no increase of the CHCl signal, the photodissociation of CHCl₂ to CHCl and Cl can be disregarded:



Furthermore, the photodissociation of the residual chloroform can form CHCl₂, which could also be observed in the two-color mass spectrum (5.1):



The enthalpies of formation used for these calculations are taken from the Active Thermochemical Tables (ATcT).^{22,23} All these heats of formation lie below the the photon energy used, making all these pathways theoretically possible.

Both CCl₂ and CHCl₃ lose a chlorine atom in the presented processes. Because of these multiple pathways that can release chlorine, we recorded images of both the atomic chlorine fragment as well as the CCl and the CHCl₂ fragment.

Figure 5.2 shows the translational energy distribution $P(E_T)$ of the CCl fragment ionized at 118.2 nm after the dissociation with a) 230 nm, and b) 250 nm light. The corresponding reconstructed images are included on the right side. Images were also recorded at 235 nm, 240 nm and 245 nm. These results are shown in the supplementary information (Figure 5.S1). The CCl formed in pyrolysis generates a background signal which was subtracted by recording an image only using the ionization laser.

The $P(E_T)$ shows a bimodal distribution independent of the dissociation wavelength. One component is isotropic and has a maximum at around 0.2 eV. The second component is strongly anisotropic with a maximum around 0.4 eV. The curve is fitted with a superposition of a Gaussian distribution and an empirical two-parameter function, also used in previous works in order to fit experimental data and extract the expectation value for the translational energy release, $\langle E_T \rangle$:²⁴⁻²⁶

$$P(E_T) = C(E_T)^a (E_T^{\text{max}} - E_T)^b \quad (5.14)$$

C is a normalization constant, a and b are the fitting parameters and E_T^{max} is the maximum translational energy that a fragment can have upon photodissociation. The maximum translational energy depends on the mass of the

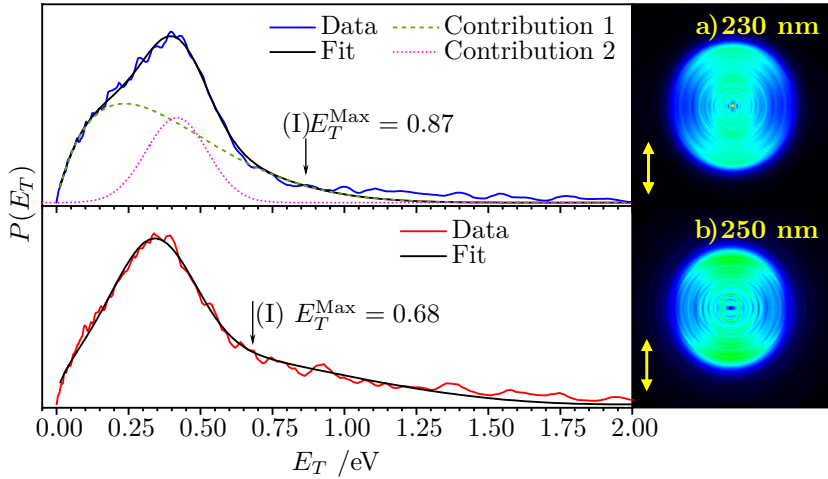


Figure 5.2: Translational energy distribution $P(E_T)$ of the CCl fragment upon excitation with a) 230 nm and b) 250 nm light. The experimental data (blue and red respectively) is fitted with the sum of a two-parameter fit (expression 5.1) and a Gaussian distribution (black). The corresponding velocity map images are displayed on the side with a yellow arrow indicating the laser polarization.

counterfragment m_B , the mass of the molecule before dissociation m_{A-B} and the difference between the photon energy and the BDE:

$$E_T^{\max} = \frac{m_B}{m_{A-B}}(h\nu - \text{BDE}) \quad (5.2)$$

Reconstructing the strongly anisotropic image gives a Legendre polynomial of the second order P_2 in the shape of a Gaussian curve, centered at around 0.4 eV. This polynomial is a measure for the anisotropy of the image. The quotient between value of the P_2 contribution and the total $P(E_T)$ gives us an approximation of the anisotropy parameter β :

$$\beta = \frac{P_2(E_T)}{P(E_T)} \quad (5.3)$$

First, this P_2 contribution is fitted with a Gaussian distribution (see SI Figure 5.S2). The result of which was used as a basis for fitting the anisotropic contribution to the translational energy distribution of the CCl fragment. This Gaussian distribution added to the empirical function (5.1) results in the fit seen in Figure 5.2. The average energy for the isotropic portion is 0.49 eV for 230 nm and 0.61 eV for 250 nm and for the anisotropic contribution 0.42 eV

and 0.34 eV respectively. This equals a fraction of excess energy released as translational energy ($\langle f_T \rangle = \langle E_T \rangle / E_T^{\max}$) of 46% and 89% for the isotropic, and 48% and 51% for the anisotropic portion. These values can be compared with a simple impulsive model, used for the calculation of the expectation value of a direct dissociation. This model is described by Tuck²⁷ and by Galloway et al.²⁸ and is based on the assumption that excess energy goes solely into the translation of the two atoms where the bond is broken within the molecule. For the case of CCl_2 dissociating into CCl and Cl (5.I), this model results in a value of $\langle f_T \rangle = 44\%$. An overview of these results is shown in Table 5.1.

Table 5.1: Summary of experimental values for the kinematics of the CCl photofragment and the lower boundary of the β -value

λ_{diss} /nm	$E_T^{\max}(\text{CCl})$ /eV (5.I)	$\langle E_T \rangle$ /eV isotropic	$\langle f_T \rangle$ /% isotropic	$\langle E_T \rangle$ /eV anisotropic	$\langle f_T \rangle$ /% anisotropic	β
230	0.87	0.40	46	0.42	48	1.3
235	0.82	0.49	59	0.35	43	1.0
240	0.77	0.43	56	0.36	47	0.8
245	0.72	0.40	56	0.36	49	0.9
250	0.68	0.61	89	0.34	51	1.4

For a translational energy distribution with multiple contributions, the anisotropy parameter β cannot simply be extracted from the image, since the different contributions each have their own β -value. This dependency of β on the kinetic energy of the CCl fragment is exemplarily shown for 230 nm in Figure 5.3 a). It starts at around 0, increasing to a value of roughly 0.6 in the region of the Gaussian fit and goes back down afterwards, even falling below 0 for the tail end of the curve. This drop below zero can be explained by low signal in this area, where small fluctuations in the background signal, which gets subtracted from the image, can result in large differences in the P_2 contribution.

However, by assuming that the entirety of the anisotropy can be attributed to the Gaussian fit, a lower limited of β can be obtained. This lower limit for the second contribution can be calculated by dividing the fit of the P_2 contribution (Figure 5.S2) by the Gaussian fit used for the second contribution (Figure 5.2). This results in β being greater than 1.3 and 1.4 for 230 nm and 250 nm respectively. The empirically fitted contribution is most probably isotropic.

Chlorine images.

Furthermore, the chlorine atoms generated in the photodissociation process were imaged using 118.9 nm light in a $[1 + 1']$ REMPI process. This approach was selected since the radicals produced in the pyrolysis absorb the focused 235 nm light used for the typically $[2 + 1]$ REMPI ionization of chlorine so well,

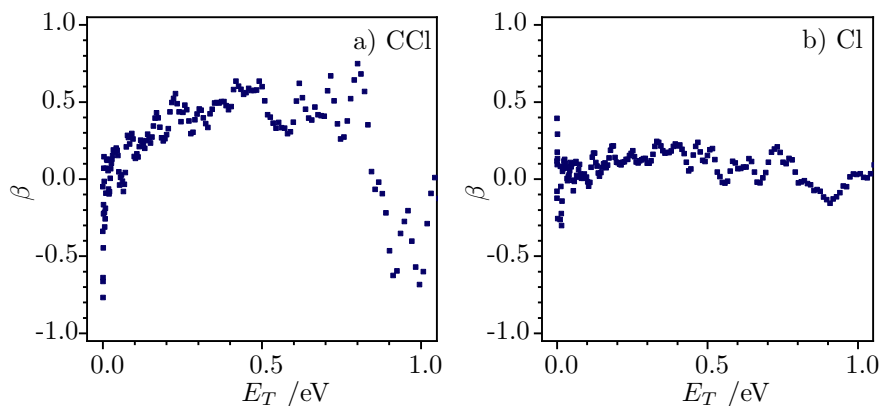


Figure 5.3: Dependency of β on the kinetic energy of a) CCl and b) Cl. Both show a mainly positive value. CCl peaks at around 0.6 while the maximum for Cl is around 0.25.

that it leads to multiphoton excitation. As a result, chlorine with significantly higher translational energy is generated which makes it impossible to obtain interpretable results. Also, the [3 + 1] REMPI scheme at 356.7 nm did not ionize enough chlorine to yield analyzable images. Thus, no data about the spin-orbit excited chlorine $^2P_{1/2}$ was obtainable.

The image of chlorine resulting from the dissociation via 230 nm light is shown in Figure 5.S3. During the photodissociation of a molecule, the momentum of the system needs to be conserved. This means that both fragments have to have the same momentum post dissociation. A comparison of the momentum of the chlorine fragment and the CCl fragment is displayed in Figure 5.4. If both fragments truly stem from the same parent molecule, in this case from CCl_2 (5.I), then the distribution of momentum for both have to be equal. The black curve shows the momentum of atomic chlorine and the blue dashed line that of the CCl fragment. It can be seen that the shape of both distributions look very similar, however CCl has a slightly lower energy overall. Also the β -value for the entire image is significantly lower, peaking at about 0.25 as opposed to 0.6 for CCl (see Figure 5.3). This signifies that probably a further pathway contributes to the observed Cl.

As previously noted, an increase of CHCl_2 upon photodissociation was measured. The increase is about one third of the the increase observed in CCl, meaning it has a significant two-color signal. An image of this CHCl_2 was also recorded (Figure 5.S4 (SI)). As previously mentioned, CHCl_2 can be formed from the photolysis of residual CHCl_3 releasing atomic chlorine (5.IV). Our results were compared to the photodissociation study of CHCl_3 at 235 nm by

Reid et al.²⁹ and the energy distribution fits perfectly. We however observed an isotropic image compared to theirs which has an anisotropy of $\beta = 0.2$. The momentum of CHCl_2 is displayed as a red dotted line in Figure 5.4. This distribution shows a momentum that is slightly shifted to a higher momentum than that of both chlorine and CCl . A comparison to the observations by Reid et al. is shown in Figure 5.S5(SI).

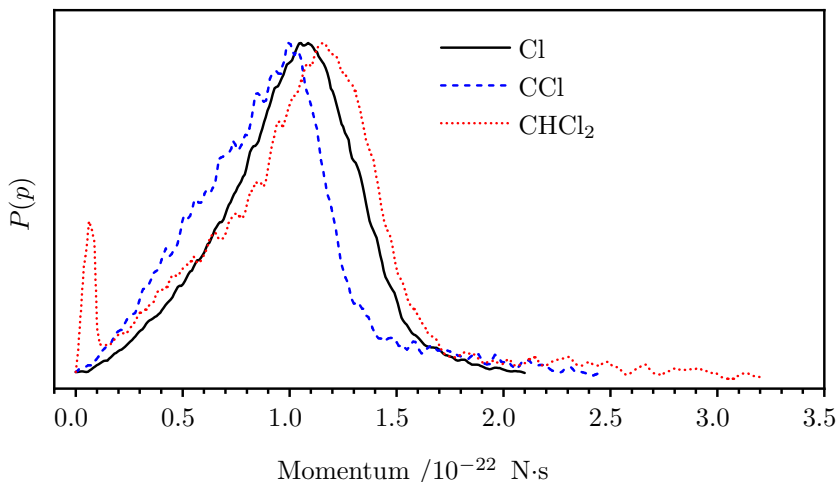


Figure 5.4: Comparison of the momentum of the Cl (black), CCl (blue) and CHCl_2 (red) fragment. All three show a similar shape with only slight differences in momentum. The Cl has a momentum that is between that of Cl and CHCl_2 , meaning Cl is generated by both pathways (5.I) and (5.II). This is supported by the fact that the anisotropy of Cl is between those of CCl and CHCl_2 .

5.5 Discussion

The photofragment image of CCl shows two clearly separate contributions, which do not show a strong dependency on the dissociation wavelength. Therefore, no change in the dissociation pathway dependent on the dissociation wavelength in the range of 230 nm to 250 nm can be inferred. The anisotropy and Gaussian shape of one of the contributions means that this dissociation pathway takes place on a very fast time scale, faster than the rotational period of the molecule it dissociates from. This happens in the case of a direct dissociation from the excited state, usually having an average total kinetic energy release of around 50%. The expectation value of around 48% for the various wavelength fits almost perfectly together with the value calculated using the

impulsive model of 44%. This lets us conclude that this contribution originates from the direct photodissociation of CCl_2 .

The other contribution extends to translational energies in excess of what is possible after the dissociation of CCl_2 with one photon. In all likelihood this second contribution itself consists of multiple contributions, since using only one two-parameter fit results in the high energy tail of the curve to not be fitted well. This suggests that in addition to the isotropic contribution at the beginning of the curve, resulting in the bump at 0.2 eV, a broader background signal is present. This broad background signal is most probably superposition of multiple processes. Since the molecules produced in pyrolysis only get cooled to a temperature of around 150 to 200 K, a part of them will be in an vibrational excited state. This leads to the photofragments receiving parts of that vibrational energy, increasing the translational energy of the fragments. Other possibilities include the fragments to be generated after multiphoton absorption during the dissociation step or result from photodissociation of one of the various other radicals generated during pyrolysis. Furthermore, the consecutive photodissociation of CHCl_2 , releasing HCl, after photolysis from residual CHCl_3 can contribute. The first part that peaks at around 0.2 eV can be attributed to the dissociation of CCl_2 , since this contribution stays the same independent of factors like backing pressure and pyrolysis power. These factors change the relative intensities of the generated fragments in the pyrolysis step and if a different fragment were to be responsible for this initial strong peak, it would get more pronounced at higher pyrolysis powers which we did not observe.

Dagdikian et al. also studied the dissociation of CCl_2 at 248 nm by monitoring the CCl fragment with laser induced fluorescence and noted that they observed two different rotational distributions, belonging to two different dissociation pathways.^{14,15} This matches with the two contributions we observe in our recorded images. Two states are accessible by excitation with 248 nm light: The $\tilde{\text{C}}^1\text{B}_2$ electronic state with the angle $\theta(\text{Cl-C-Cl}) = 94.7^\circ$ and the $\tilde{\text{D}}^1\text{A}_1$ which prefers a linear geometry. The bond angle inside the ground state has been calculated to $\theta(\text{Cl-C-Cl}) = 109.2^\circ$.³⁰ Because of the larger torque upon excitation to the $\tilde{\text{D}}^1\text{A}_1$ state, the higher rotational energy distribution observed by Dagdikian et al. was assigned to a dissociation from this state.¹⁵ On the other hand, the pathway leading to a rotational distribution peaking at $J \approx 0.5$ was assigned to the dissociation from the $\tilde{\text{C}}^1\text{B}_2$ state. The expected translational energy under the assumption of CCl only being formed in the vibrational ground state were calculated to 0.41 eV and 0.67 eV respectively. Because of the lack of structure in the photofragment excitation spectra, it was concluded that both pathways are from a direct dissociation. If both pathways were to follow a direct dissociation, two Gaussian shaped contributions peaking at the above mentioned values would be expected with an anisotropy depending on the transition dipole moment. However, we observe only one Gaussian

distribution with an anisotropy, peaking at 0.34 eV at 250 nm. This is very close to the expected value for the dissociation from the \tilde{D}^1A_1 electronic state and matches well with the reported translational energy distribution recorded by Morley et al., which has a peak at 0.44 eV.¹⁶ However, no anisotropy was observed by them. But it was also stated that the signals were too small for a precise determination of the anisotropy parameter which could explain why they observed no anisotropy.

The second contribution peaking at around 0.2 eV shows a shape more characteristic for a statistical process. It was noted, that there might be small barriers before dissociation in the excited states.¹⁵ Based on this previous work, we conclude that it is highly probable that one is present in the \tilde{C}^1B_2 state resulting in the excited molecule being trapped shortly by this barrier, giving it time to rotate and thus losing the anisotropy and resulting in an redistribution of internal energy, leading to the translational energy distribution being shaped similar to a statistical process. The expected β -value for a direct dissociation from this state is 0.62.³⁰ Such a high anisotropy would be noticeable but is not observed for our isotropic contribution, furthermore underpinning our conclusion that this pathway is not a result from a direct dissociation. Note that the value is also too low for the observed anisotropic portion since a value for β around 1 is to be expected here. However, it cannot be entirely excluded that this contribution stems from a statistical dissociation after relaxation back into the ground state.

Because of the uncertainty of the various contributions in our CCl image, definitive conclusions about the isotropic portion cannot be derived. But, taking the data of the dissociation at 230 nm as an example, one can assume that the average energy of the isotropic contribution is between 0.15 and 0.3 eV. This would equal a fraction of energy released as translational energy $\langle f_T \rangle$ between $\langle f_T \rangle$ 17% and 34% which is a reasonable range for a dissociation from a state including a barrier. On the other hand, the expected translational energy of the anisotropic portion is only based on the P_2 function and as thus can be seen as reliable.

The momentum of atomic chlorine also shows good agreement with that of CCl, furthermore indicating that pathway (5.I) is being observed. The slightly higher energy and lower anisotropy in comparison to the CCl momentum can be explained by the presence of chlorine from the dissociation of residual chloroform. Our measurement of the $CHCl_2$ fragment is identical to the one carried out by Reid et al.,²⁹ except for the fact that they observed an anisotropy of $\beta = 0.2$. The addition of the anisotropic CCl and the isotropic $CHCl_2$ result in the lower anisotropy observed in our Cl translational energy distribution compared to the one of CCl. Because the spin-orbit excited chlorine could not be ionized with our method, information about its participation in the photodissociation remains open.

5.6 Conclusion

The photodissociation dynamics of CCl_2 upon excitation with wavelengths between 230 nm and 250 nm was investigated using the velocity map imaging technique. This CCl_2 was generated via flash pyrolysis. Small amounts of CCl and CCl_3 were also observed in the mass spectra. Velocity map images of the CCl fragment and the atomic chlorine were recorded. For the CCl fragment a bimodal translational energy distribution was found. One contribution belongs to a direct dissociation of CCl_2 (5.I). For this channel, the average kinetic energy release is around 48% which is in good agreement with the previous work by Morley et al. and the impulsive model. The anisotropy β is around 1. While the average energy for this pathway is based solely on the P_2 contribution and thus reasonably accurate, the β value has a strong uncertainty to it because of the overlap of the two contributions. The second contribution most likely happens through dissociation after a small barrier and is isotropic. Because of the overlap with the direct dissociation pathway and the background signal, it can only be concluded that between 17% and 34% of the energy goes into translation. The chlorine image shows a similar distribution to the CCl fragment, however, the momentums do not match perfectly. The presence of two-color CHCl_2 shows that residual chloroform gets dissociated as well, contributing to the Cl image.

5.7 Supplementary Information

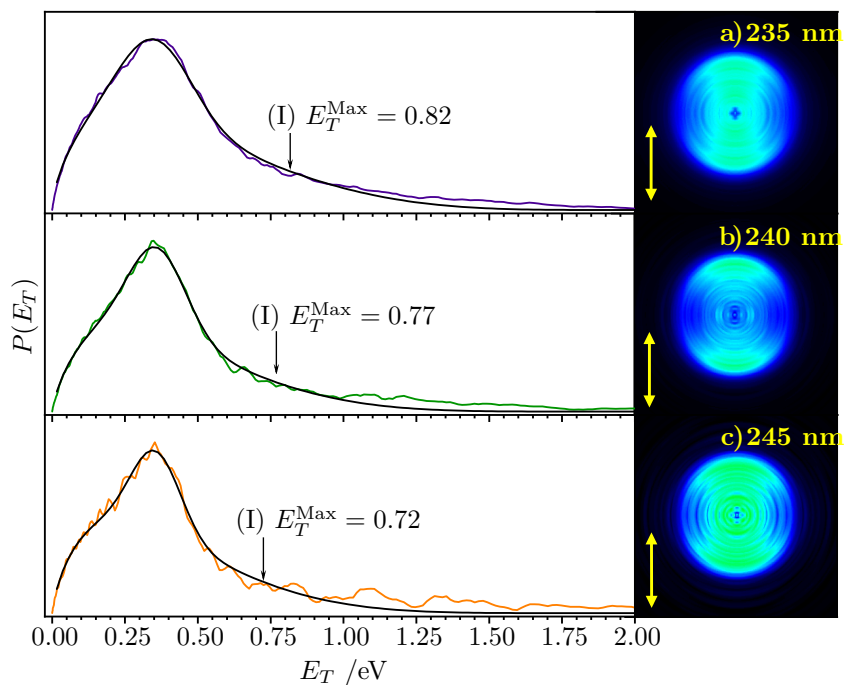


Figure 5.S1: Translational energy distribution $P(E_T)$ of the CCl fragment upon excitation with a) 235 nm, b) 240 nm and c) 245 nm light. The experimental data (purple, green and orange respectively) is fitted with sum of a two-parameter fit (expression 5.1) and a Gaussian distribution (black). The corresponding velocity map images are displayed to the side with a yellow arrow indicating the laser polarization.

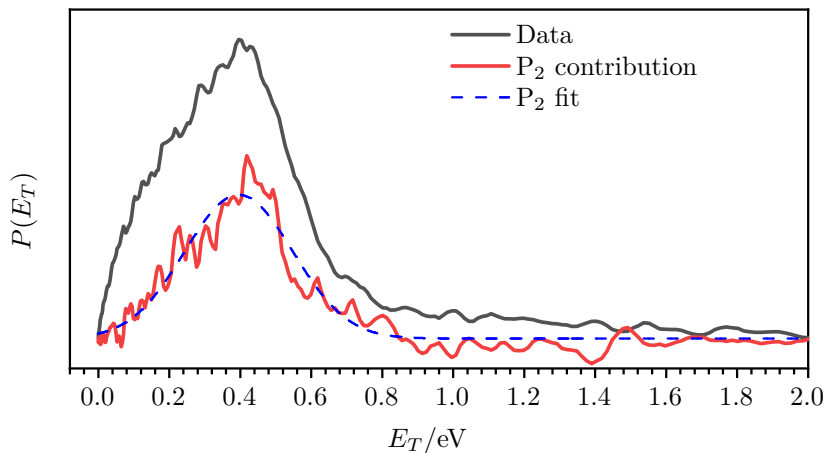


Figure 5.S2: Translational energy distribution $P(E_T)$ of the CCl fragment upon excitation with 230 nm light (black) and the contribution of the second order Legendre polynomial (P_2) (red). The Gaussian fit of the P_2 contribution is shown in blue.

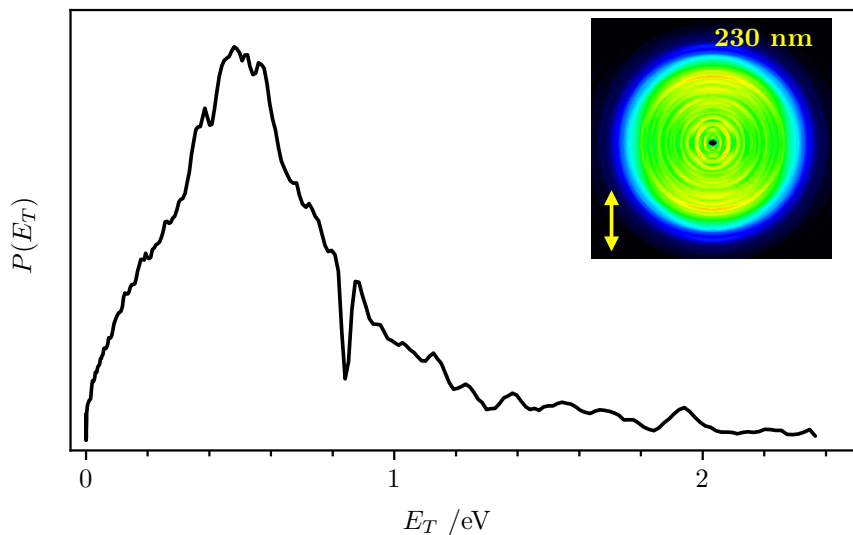


Figure 5.S3: Translational energy distribution $P(E_T)$ of the Cl fragment upon excitation with 230 nm light. The corresponding velocity map images are displayed to the side with a yellow arrow indicating the laser polarization.

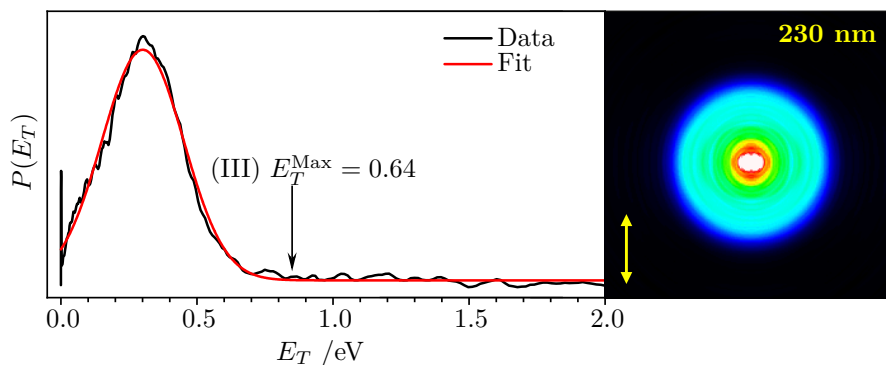


Figure 5.S4: Translational energy distribution $P(E_T)$ of the CHCl_2 fragment upon excitation with 230 nm light. The corresponding velocity map images are displayed to the side with a yellow arrow indicating the laser polarization.

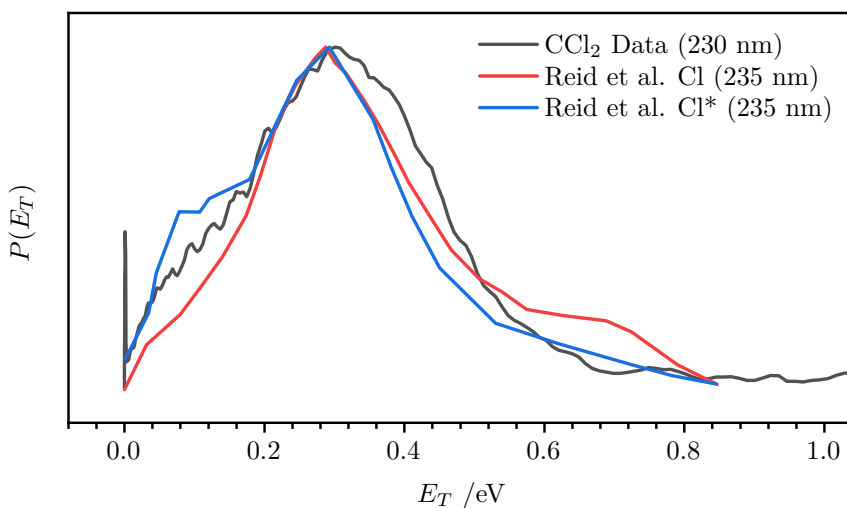


Figure 5.S5: The translational energy distribution $P(E_T)$ of the CHCl_2 fragment upon excitation with 230 nm light is displayed in black. The red and blue curves, show digitized data from Reid et al.²⁹ The red curve is from their image of the Cl and the blue curve from their Cl^* fragment. The data was gathered at an dissociation wavelength of 235 nm. The difference in energy of the falling edges compared to the CCl_2 data gathered in the experiments described above is approximately the same as the energy difference between 235 nm and 230 nm.

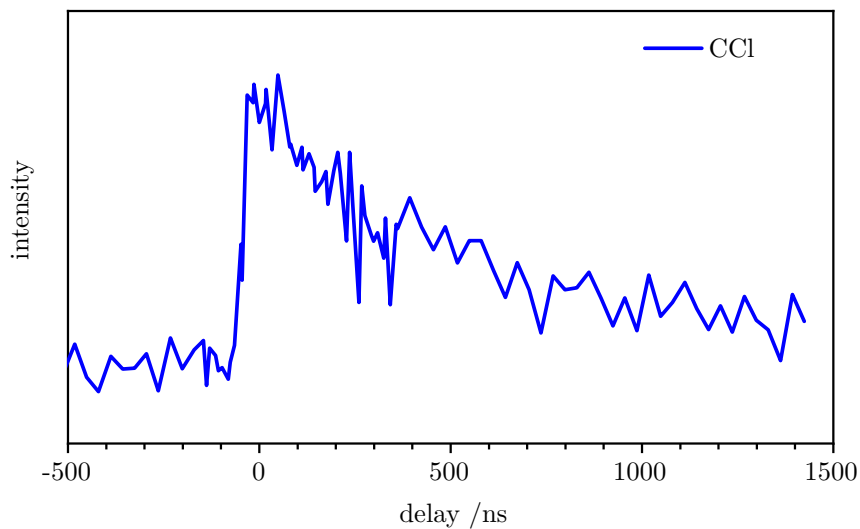


Figure 5.S6: Delay scan between the dissociation and the ionization laser. The rise time is within the resolution of the experiment, meaning that both dissociation pathways take place faster than the pulse duration of the laser of 10 ns.

5.8 Bibliography

- (1) Ramanathan, V.; Feng, Y. *Atmos. Environ.* **2009**, *43*, 37–50.
- (2) Molina, M. J.; Rowland, F. S. *Nature* **1974**, *249*, 810–812.
- (3) Myers, T. L.; Kitchen, D. C.; Hu, B.; Butler, L. J. *J. Chem. Phys.* **1998**, *104*, 5446.
- (4) Morton, M. L.; Butler, L. J.; Stephenson, T. A.; Qi, F. *J. Chem. Phys.* **2002**, *116*, 2763.
- (5) Matsumi, Y.; Das, P. K.; Kawasaki, M. *J. Chem. Phys.* **1992**, *97*, 5261.
- (6) Matsumi, Y.; Das, P. K.; Kawasaki, M. *J. Chem. Phys.* **1998**, *92*, 1696.
- (7) Lin, J. J.; Chen, Y.; Lee, Y. Y.; Lee, Y. T.; Yang, X. *Chem. Phys. Lett.* **2002**, *361*, 374–382.
- (8) Foley, C. D.; Joalland, B.; Alavi, S. T.; Suits, A. G. *Phys. Chem. Chem. Phys.* **2018**, *20*, 27474–27481.
- (9) Deshmukh, S.; Hess, W. P. *J. Chem. Phys.* **1998**, *100*, 6429.
- (10) Ahmed, M.; Peterka, D. S.; Regan, P.; Liu, X.; Suits, A. G. *Chem. Phys. Lett.* **2001**, *339*, 203–208.
- (11) Matthaiei, C. T.; Mukhopadhyay, D. P.; Röder, A.; Poisson, L.; Fischer, I. *Phys. Chem. Chem. Phys.* **2022**, *24*, 928–940.
- (12) Kohn, D. W.; Robles, E. S.; Logan, C. F.; Chen, P. *J. Phys. Chem.* **1993**, *97*, 4936–4940.
- (13) Shin, S. K.; Dagdigian, P. J. *J. Chem. Phys.* **2006**, *125*, 133317.
- (14) Shin, S. K.; Dagdigian, P. J. *Phys. Chem. Chem. Phys.* **2006**, *8*, 3446–3452.
- (15) Shin, S. K.; Dagdigian, P. J. *J. Chem. Phys.* **2008**, *128*, 154322.
- (16) Morley, G. P.; Felder, P.; Huber, J. R. *Chem. Phys. Lett.* **1994**, *219*, 195–199.
- (17) Eppink, A. T.; Parker, D. H. *Rev. Sci. Instrum.* **1998**, *68*, 3477.
- (18) Whitaker, B. J., *IMAGING IN MOLECULAR DYNAMICS Technology and Applications (A User's Guide)*; Cambridge University Press: 2003.
- (19) Giegerich, J.; Petersen, J.; Mitrić, R.; Fischer, I. *Phys. Chem. Chem. Phys.* **2014**, *16*, 6294–6302.
- (20) Matthaiei, C. T.; Mukhopadhyay, D. P.; Fischer, I. *J. Phys. Chem.* **2021**, *125*, 2816–2825.
- (21) Garcia, G. A.; Nahon, L.; Powis, I. *Rev. Sci. Instrum.* **2004**, *75*, 4989.
- (22) Ruscic, B.; H., B. D. Active Thermochemical Tables (ATcT) values based on ver. 1.122p of the Thermochemical Network, 2020.

- (23) Ruscic, B.; Pinzon, R. E.; Morton, M. L.; Laszevski, G. V.; Bittner, S. J.; Nijssure, S. G.; Amin, K. A.; Minkoff, M.; Wagner, A. F. *J. Phys. Chem.* **2004**, *108*, 9979–9997.
- (24) Pachner, K.; Steglich, M.; Hemberger, P.; Fischer, I. *J. Chem. Phys.* **2017**, *147*, 084303.
- (25) Deyerl, H. J.; Fischer, I.; Chen, P. *J. Chem. Phys.* **1999**, *111*, 3441.
- (26) North, S. W.; Marr, A. J.; Furlan, A.; Hall, G. E. *J. Phys. Chem.* **1997**, *101*, 9224–9232.
- (27) Tuck, A. F. *J. Chem. Soc., Faraday Trans. 2* **1977**, *73*, 689–708.
- (28) Galloway, D. B.; Glenewinkel-Meyer, T.; Bartz, J. A.; Huey, L. G.; Crim, F. F. *J. Chem. Phys.* **1998**, *100*, 1946.
- (29) Reid, M.; Green, V.; Koehler, S. P. *Phys. Chem. Chem. Phys.* **2014**, *16*, 6068–6074.
- (30) Cai, Z. L.; Zhang, X. G.; Wang, X. Y. *Chem. Phys. Lett.* **1993**, *210*, 481–487.

6 Summary

Chlorine-containing hydrocarbons pose a significant risk to the environment. If they reach the stratosphere they can get dissociated by UV radiation, releasing chlorine atoms. The chlorine atoms then contribute to the catalytic destruction of the ozone layer. That is why the photodissociation dynamics leading to chlorine release is an important subject of study for understanding atmospheric chemistry. Therefore, these types of molecules have been widely studied. However, the radicals generated from the photodissociation can still contain further chlorine atoms. Thus, to better understand atmospheric chemistry, it is important to investigate whether these radicals can release additional chlorine, and if so, how this process occurs. However, the challenges of generating radicals have led to this research field being neglected. Only a few radicals and only in a limited matter have been studied.

The goal of the work presented in this thesis was to advance the study of chlorinated radicals which are relevant in atmospheric processes. The method of flash pyrolysis was employed in order to generate the chlorinated radicals. The dissociation dynamics were then studied with the velocity map imaging technique. This technique gives insight into the kinetic energy distribution of fragments generated in a photolysis process. Also, the angular distribution is extractable from the images. With this data, information on the states involved in the process can be gained.

The atmospherically relevant chlorine-containing radicals usually exhibit a broad absorption band around 235 nm which is a good region to probe the dissociation dynamics. However, this is the same wavelength that is typically used for ionizing chlorine atoms with a $[2 + 1]$ REMPI scheme. Since a focused laser is required for this ionization method, the intensity of 235 nm light in the ionization region is very high. This high intensity leads to some radicals to absorb multiple photons. The radicals can then dissociate, releasing chlorine atoms with considerably higher kinetic energy than would be the case for the absorption of only one photon. This high energy contribution results in the velocity map images to be difficult to interpret.

This led to the investigation of an alternative ionization pathway. Chlorine can also be ionized with 356 nm light in a $[3 + 1]$ REMPI process. This requires very tight focusing of the laser beam and even then the amount of chlorine ionized is very small. However, the corresponding transition at 118.9 nm lies in the tripling range of xenon. Experience using a tripling cell filled with xenon in order to generate the third harmonic of a Nd:YAG laser in the same tripling window at 118.2 nm has already been gathered. Using the 356 nm output of a dye laser and tripling its frequency inside the gas cell in order to excite chlorine, showed to be a very efficient method for ionizing the atomic chlorine. In order to gain complete information of a dissociation process, information about the

spin-orbit excited chlorine is necessary. Unfortunately no Cl^* absorption line was present within the used tuning range of xenon. Still, this method proved to supply high quality images of the ground state chlorine without having unwanted background signals.

In order to establish this method, a study on the stable molecule benzoyl chloride was performed. Benzoyl chloride has already been studied by analyzing the time-of-flight profile and it was shown that chlorine gets released via two different channels. In the here presented findings, benzoyl chloride was dissociated at four different wavelengths (237 nm, 253 nm, 265 nm and 279.6 nm). With these photons, the molecule was excited into the S_1 , S_2 and the S_3 state. It was found that the dissociation pathway is unimodal and independent on the dissociation wavelength, having an average kinetic release of 20%. Furthermore, the image was isotropic. Because of these insights, the dissociation pathway was attributed to a statistical dissociation pathway from the vibrationally excited ground state. The difference to the previous study can be explained by the higher accuracy of our method. Analyzing a TOF MS spectrum is a 1-dimensional analysis method compared to velocity map imaging where the 2D projection of the Newton sphere is recorded. In addition a cylindrical symmetry is present making the reconstruction of the Newton sphere highly accurate. On the other hand, fitting of the TOF MS spectrum is a very inaccurate procedure, where many different fits can produce similar fitting results.

After showing that ionizing chlorine with a $[1 + 1']$ REMPI scheme is a reliable method for recording Cl VMIs, the study of the photodissociation of chlorine-containing radicals was started. At first, the trichloromethyl radical CCl_3 was examined. It has been shown that CCl_4 , a haloalkane, is a major contributor to the destruction of stratospheric ozone. In the past, CCl_4 was widely used in a variety of ways and a lot of it got released into the environment. In the upper parts of the stratosphere, residual VUV light in the area around 200 nm is still present. The CCl_4 can absorb this residual radiation, resulting in the dissociation to CCl_3 and Cl. In the here presented study, CCl_3 was generated by the pyrolysis of CCl_4 and was then excited in the range of 230 to 250 nm. It was observed that the CCl_3 dissociates via multiple channels. The first channel is a predissociation that takes place on a similar time scale as the rotational period of CCl_3 and results in the generation of CCl_2 and Cl. At shorter wavelengths an anisotropy can be observed but increasing the wavelength above 240 nm it begins to disappear. However, the energy distribution stays the same. This leads to the conclusion that the pathway stays the same, independent on the wavelength. But there exists a barrier in the excited state which can be easily overcome if the excitation energy is high enough. Above 240 nm more energy needs to be redistributed in order for the barrier to be overcome which increases the required timescale for the dissociation to take place, making it take longer than the rotational period of CCl_3 which in turn causes the anisotropy to disappear. The second pathway is a statistical process leading to the formation

of CCl and Cl₂. Multiple contributions overlap in the CCl image. In addition to the CCl being created in the dissociation process of CCl₃, CCl fragments generated from the dissociation from CCl₂, and a broad background signal can be observed. This overlap in signals did not allow for exact information on the CCl₃ dissociation pathway to CCl to be gained. However, this pathway seems to be isotropic and shows an energy distribution shape that is similar to a statistical process.

In order to better understand the contributions leading to the formation of CCl in the CCl₃ study, a detailed examination of the dissociation dynamics of CCl₂ was conducted. It was generated by flash pyrolysis of CHCl₃. Here it is shown, that CCl₂ is an additional source of atmospheric chlorine, since it dissociates upon UV absorption to CCl and Cl via two separate pathways. The same excitation wavelengths as in the CCl₃ study were used. Both observed pathways overlap and additionally a broad background signal is present. However, it can be said that one pathway is a direct dissociation releasing around 48% of the excess energy as translation energy. The anisotropy parameter β for this process is around 1. The second pathway cannot be assigned because of the overlap with the direct dissociation channel. But it seems that this pathway leads to an isotropic energy distribution with a shape resembling a statistical dissociation or a predissociation.

With these studies a new chlorine ionization scheme could be established and information on the photodissociation dynamics of chlorine-containing radicals that are relevant in atmospheric processes could be gained. Currently studies on other halogen containing radicals are being conducted. So far, the photodissociation dynamics of two chlorine-containing methyl radicals have been examined. In this work the photodissociation dynamics of CCl₃ has been studied while those of CH₂Cl have been examined by others. Currently the last remaining chlorine-containing methyl radical CHCl₂ is being studied. So far CHCl₂Br has been used as a precursor because the C-Br bond is weaker than the C-Cl bond, resulting in the probability of the C-Br bond to be cleaved via pyrolysis to be higher. However, a significant amount of bromine-containing radicals get generated leading to an overlap of many signals when investigating the photodissociation of the CHCl₂ radical. In the future CHCl₂I will be synthesized and it will be investigated if it is a better precursor. The C-I bond is even weaker than the C-Br bond and hopefully this bond will be cleaved more selectively in pyrolysis.

Additionally, it can also be tried to investigate if ionization of the spin-orbit excited state of chlorine in [1 + 1'] REMPI using krypton as tripling gas is possible. A few observed lines exist around 110 nm which is right on the edge of one of the tripling windows of krypton.

Lastly, using the knowledge gained from ionizing Cl via the [1 + 1'] REMPI scheme, first experiments on ionizing atomic bromine have been conducted.

Bromine can be ionized by tripling the dye laser in the same Xe tripling window as has been done for chlorine. It can absorb at 117.83 nm and at 118.88 nm. Furthermore, spin-orbit excited bromine can be excited at 118.87 nm and 118.89 nm. Which is why the same limitations that apply to chlorine imaging do not apply here. This method is currently being tested by examining the photodissociation dynamics of the CHBr_2 radical.

List of Figures

1.1	Schematic description of the various dissociation pathways . . .	3
1.2	Schematic of the Newton spheres generated in a photodissociation process	5
1.3	Newton sphere for different angles between transition dipole moment $\vec{\mu}$ and the bond that is broken \vec{k}	6
2.1	Schematic of the generation of the molecular beam	12
2.2	Schematic of in thesis used apparatus	15
2.3	Schematic of different ionization schemes	18
2.4	Representation of the different REMPI schemes used to ionize chlorine in this thesis	20
2.5	Schematic of the xenon filled gas cell used for tripling	22
2.6	Schematic of the main components of a VMI setup	23
2.7	Steps required to analyze a velocity map image	27
2.8	Typical kinetic energy distribution fitted with a two-parameter fit	31
2.9	Example for the dependence of radical generation with pyrolysis	35
2.10	Comparison of the $P(E_T)$ of CCl generated from the photodissociation of CCl_2	36
3.1	Cl REMPI scan at 118.9 nm and and mass spectrum on the REMPI line	46
3.2	Gas phase absorption spectrum of the Ph-CO-Cl	48
3.3	Mass spectra obtained after the photodissociation of benzoyl chloride	49
3.4	Translational energy distribution of CCl after the photodissociation of benzoyl chloride at 237 nm and 279.6 nm	50
3.5	Comparison of one-parameter fits used for the translational energy distribution of CCl after the photodissociation of benzoyl chloride	51
3.6	One-color translational energy distribution of Cl at 235.35 nm .	54
3.7	Proposed scheme for photodissociation of Ph-CO-Cl	57
3.S1	VMI and corresponding $P(E_T)$ of ^{35}Cl from photodissociation of Cl_2 at 356.6 nm	60
3.S2	Single photon 118.2 nm photoionization mass spectra of Ph-CO-Cl	61
3.S3	Comparison of the experimentally measured symmetrized velocity map images of fragmented Cl with the reconstructed images	62
3.S4	Translational energy distribution $P(E_T)$ of photodissociated ^{35}Cl upon excitation to S_3 state at 253 nm	63
3.S5	Translational energy distribution $P(E_T)$ of photodissociated ^{35}Cl upon excitation to 265 nm	64
3.S6	Fit of the experimental translational energy distributions $P(E_T)$ of photodissociated ^{35}Cl (black) at 253 nm (top) and 265 nm (bottom)	65

3.S7	Time dependence of the Cl signal at four dissociating wavelengths	66
3.S8	[2 + 1] REMPI spectra of fragmented Cl and Cl* after photodissociation of Ph-CO-Cl recorded in one-color experiment	67
4.1	Two-color mass spectra using CCl ₄ as a precursor	78
4.2	Mass spectra with and without pyrolysis, recorded with fs-lasers, $\lambda_{\text{pump}} = 266$ nm and $\lambda_{\text{probe}} = 798$ nm around time zero. CCl ₃ Br was employed as a precursor.	79
4.3	The time-resolved ion signal of CCl ₃ at 266 nm excitation is fitted by a monoexponential decay with a time constant of 50 fs	80
4.4	TR-PES spectrum with 266 nm pump/798 nm probe, displayed as a 2D-map	81
4.5	Summary of the relevant dissociation pathways in CCl ₃ and CCl ₂	82
4.6	Translational energy distribution $P(E_T)$ of the CCl ₂ fragment upon excitation with 230 nm and 250 nm light using CCl ₄ as a precursor	84
4.7	Translational energy distribution $P(E_T)$ of the CCl fragment upon excitation with 230 nm and 250 nm light using CCl ₄ as a precursor	87
4.8	Translational energy distribution $P(E_T)$ of the CCl fragment upon excitation with 230 nm and 250 nm light using CHCl ₃ as a precursor	88
4.9	Translational energy distribution of atomic Cl as a function of momentum, recorded at 230 nm	90
4.S1	Two-color mass spectra using CHCl ₃ as a precursor	96
4.S2	Time-resolved ion signals recorded in the fs-experiments	97
4.S3	Time delay between dissociation and ionisation laser for the CCl and CCl ₂ fragment in the ns-experiments for $\lambda_{\text{diss}} = 230$ nm	97
4.S4	Translational energy distribution $P(E_T)$ of the CCl ₂ fragment upon excitation of CCl ₃ with 235 nm, 240 nm and 245 nm light. CCl ₄ was employed as a precursor	98
4.S5	Translational energy distribution $P(E_T)$ of the CCl fragment using CCl ₄ as a precursor for CCl ₃ . In 235 nm, 240 nm and in 245 nm light was used for dissociation	99
4.S6	Angular distribution of the CCl ₂ images of at the dissociation wavelengths of 230 nm and 250 nm	100
4.S7	Translational energy distribution $P(E_T)$ of the Cl (² P _{3/2}) photofragment after photodissociation with 230 nm light, using CCl ₄ as a precursor	101
4.S8	Comparison of the momenta of the Cl and CCl ₂ fragments from the photodissociation of CCl ₃ and the P2 term	102
5.1	Mass spectra showing the fragments generated in a two-color dissociation process using CHCl ₃ as a precursor	110

5.2	Translational energy distribution of the CCl fragment upon excitation with 230 nm and 250 nm light using chloroform as a precursor	112
5.3	Dependency of β on the kinetic energy of CCl and Cl	114
5.4	Comparison of the momentum of the Cl, CCl and CHCl ₂ fragment using chloroform as a precursor	115
5.S1	Translational energy distribution $P(E_T)$ of the CCl fragment upon excitation with 235 nm, 240 nm and 245 nm light using chloroform as a precursor	119
5.S2	Translational energy distribution $P(E_T)$ of the CCl fragment upon excitation with 230 nm light and the contribution of the second order Legendre polynomial	120
5.S3	Translational energy distribution $P(E_T)$ of the Cl fragment upon excitation with 230 nm light using chloroform as a precursor . .	120
5.S4	Translational energy distribution $P(E_T)$ of the CHCl ₂ fragment upon excitation with 230 nm light using chloroform as a precursor	121
5.S5	Comparison of the translational energy distribution $P(E_T)$ of the CHCl ₂ fragment upon excitation with 230 nm light using chloroform as a precursor with the data gathered by Reid et al.	121
5.S6	Delay scan between the dissociation and the ionization laser for the photofragment experiments using chloroform as a precursor	122

List of Tables

3.1	Maximum Translational Energy Available for Fragmented $^{35}\text{Cl}(E_T^{\text{max}})$ at Different Photodissociation Wavelengths along with some Energy Parameters ^a	52
3.S1	Comparison of the fraction of excess energy released as translation computed in different models along with experimental values. 67	67
3.S2	Translational energy release computed by the impulsive model as described in References. ^{62,63}	68
4.1	Vertical excitation energies (at the ground state minimum geometry) and oscillator strengths f , computed by TD-DFT . . .	76
4.2	Experimental values for the CCl_2 fragments from CCl_3 photodissociation	85
4.S1	Summary of the maximum possible kinetic energy E_T^{max} for the CCl fragment for different reaction pathways, see main paper for definition of the reactions.	102
5.1	Summary of experimental values for the kinematics of the CCl photofragment and the lower boundary of the β -value	113

Acknowledgments

Schließlich möchte ich noch den zahlreichen Personen danken, die mich durch die Zeit der Promotion begleitet haben.

Im Besonderen danke ich Prof. Dr. Ingo Fischer, nicht nur, dass er mir die Gelegenheit gegeben hat, in seiner Arbeitsgruppe zu promovieren, sondern auch für die hervorragende Betreuung während der Planung, Durchführung und Auswertung der Experimente. Obwohl ich einen physikalischen Hintergrund habe, hast du mir die Chance gegeben, mein Wissen im Bereich der physikalischen Chemie auszubauen. Für Fragen und Anregungen hattest du immer ein offenes Ohr, was das Arbeiten in deiner Gruppe sehr angenehm gemacht hat.

Außerdem geht mein Dank an Dr. Deb Pratim Mukhopadhyay, der mich die ersten 2 Jahre meiner Promotion bei der Durchführung der Experimente begleitet hat. Both of us started at around the same time in the group and both of us only had limited knowledge of the experiments being conducted. Together, we challenged the experiments and got to know how it works in great detail. Without your assistance I would probably not have been able to do the experiments so efficiently in the same amount of time.

Mein Dank geht auch an alle ehemaligen Doktoranden, mit denen ich einige Jahre zusammengearbeitet habe. Marco Flock, Domenik Schleier, Florian Hirsch und Engelbert Reusch: Als ich in der Arbeitsgruppe angefangen habe, habt ihr mich mit offenen Armen empfangen, wodurch ich mich sofort als ein Teil der Gruppe gefühlt habe. Die gemeinsamen Kickerpartien und die gelegentlichen Schafkopfabende waren toll und werden mir immer in Erinnerung bleiben.

Insbesondere möchte ich mich noch bei dir, Engelbert, für das super Wildfleisch bedanken, dass du mir gelegentlich mitgebracht hast und das wir gemeinsam an schönen Abenden zubereitet und genossen haben.

Weiterhin möchte ich meinem Bürokollegen Tobias Preitschopf für die tolle Gesellschaft danken. Mit dir konnte man sich immer über verschiedenste Themen austauschen, ob privat oder wissenschaftlich. Die Atmosphäre in unserem Büro war immer klasse, weshalb es immer wieder eine Freude war zur Uni zu kommen. Sobald ich die Arbeitsgruppe verlasse wirst du der Senordoktorand sein und ich werde dir den Titel feierlich überreichen, so wie er mir schon von Domenik übergeben wurde.

An dieser Stelle möchte ich dann auch den neueren Mitgliedern danken: Floriane Sturm, Marius Gerlach, Emil Karaev und Klaus Hofmann. Ich hoffe, wir haben euch all die guten Seiten der Arbeitsgruppe gezeigt und dass euch die Zusammenarbeit genauso viel Spaß macht wie mir.

Natürlich bedanke ich mich auch bei Kasimir Merlin Philipp, der während seiner Bachelorarbeit mit mir an dem Projekt gearbeitet hat. Deine schnelle

Auffassungsgabe und dein großes Interesse an der Materie haben die Betreuung unglaublich einfach gemacht. Ich bin mir sicher, dass du erfolgreich deinen Weg an der Universität Göttingen finden wirst.

Ein Dank geht auch an meine zwei Masteranden Lilith Wohlfart und Jonas Fackelmayer. Ich hatte die Freude, euch während eurer Masterarbeit zu betreuen und werde mit dem Abschluss meiner Promotion das Experiment an euch weitergeben. Ich bin mir sicher, dass ihr dieses Projekt erfolgreich fortsetzen und viele neue spannende Ergebnisse erhalten werdet.

Die Mitglieder der Mechanik- und Elektronikwerkstatt, Wolfgang Liebler, Ralf Kohrmann, Katharina Schreckling, Peter Lang, Markus Keller, Reiner Eck und Uwe Reuß waren maßgeblich am Erfolg dieser Arbeit beteiligt, weshalb ich mich bei Ihnen bedanken muss. Sobald es irgendwelche Probleme mit dem experimentellen Aufbau gab, standet Ihr sofort zur Seite. Danke dafür!

Schließlich muss ich mich noch bei meinen Eltern, die mich bei meinem Weg bis hierher unterstützt haben, bedanken. Ohne euch wäre ich nicht da wo ich jetzt bin.

Eidesstattliche Erklärung

Hiermit erkläre ich an Eides statt, dass ich die Dissertation

"Studying the Photodissociation of Chlorine-Containing Molecules with Velocity Map Imaging"

selbständig angefertigt und keine anderen als die von mir angegebenen Quellen und Hilfsmittel benutzt habe.

Ich erkläre außerdem, dass ich diese Dissertation weder in gleicher noch in anderer Form bereits in einem anderen Prüfungsverfahren vorgelegt habe.

Außer die mit dem Zulassungsgesuch urkundlich vorgelegten Graden habe ich keine weiteren akademischen Grade erworben oder zu erwerben versucht.

Würzburg, den

M.Sc. Christian Tobias Matthaei

Erklärung zur Autorenschaft

Photodissociation of Benzoyl Chloride: A Velocity Map Imaging Study Using VUV Detection of Chlorine Atoms
Christian T. Matthaei, Deb Pratim Mukhopadhyay, and Ingo Fischer
Published: J. Phys. Chem. A, 2021, 125, 14, 2816-2825

Detaillierte Darstellung der Anteile an der Veröffentlichung (in %)
Angabe Autoren/innen (ggf. Haupt- / Ko- / korrespondierender/ Autor/in) mit Vorname Nachname (Initialen)

Christian T. Matthaei (C. T. M.), Deb Pratim Mukhopadhyay (D. P. M.), Ingo Fischer (I. F.)

Autor	C. T. M.	D. P. M.	I. F.	Σ in Prozent
Experimente	30%	20%		50%
Auswertung	13%	7%		20%
Verfassen der Veröffentlichung	5%	10%	5%	20%
Korrektur der Veröffentlichung	2%	2%	2%	6%
Koordination der Veröffentlichung	0.5%	0.5%	3%	4%
Summe	50.5%	39.5%	10%	100%

Erklärung zur Autorenschaft

Photodissociation of the trichloromethyl radical: photofragment imaging and femtosecond photoelectron spectroscopy
 Christian T. Matthaei, Deb Pratim Mukhopadhyay, Anja Röder, Lionel Poisson, and Ingo Fischer
 Published: Phys. Chem. Chem. Phys., 2022, 24, 928-940

Detaillierte Darstellung der Anteile an der Veröffentlichung (in %)
 Angabe Autoren/innen (ggf. Haupt- / Ko- / korrespondierender/r Autor/in) mit Vorname Nachname (Initialen)

Christian T. Matthaei (C. T. M.), Deb Pratim Mukhopadhyay (D. P. M.), Anja Röder (A. R.), Lionel Poisson (L. P.), Ingo Fischer (I. F.)						
Autor	C. T. M.	D. P. M.	A. R.	L. P.	I. F.	∑ in Prozent
Calculations			2%			2%
Time-resolved experiments			30%			30%
Photofragment Imaging experiments	28%	15%				43%
Writing of publication	6%	1%	2%	2%	4%	15%
Correction of publication	1%	1%	1%	1%	1%	5%
Coordination of publication				2%	3%	5%
Summe	35%	17%	35%	5%	8%	100%

